

Shear induced Crystallization of a Colloidal Glass

Nikos N. Koumakis

Master Thesis



**Department of Materials Science and Technology
University of Crete**

November 2007

Committee:

George Petekidis

Dimitris Vlassopoulos

Jan K. G. Dhont

Abstract:

The phase behavior of a suspension of monodisperse colloidal hard spheres is determined solely by its volume fraction. At low concentrations it is in a liquid state and at higher concentrations it forms an ordered crystal as a way to maximize entropy. At a transition volume fraction of 0.58 the system becomes mechanically trapped in a metastable glassy state. When put under oscillatory strain, hard spheres suspensions generally tend to order. When a high volume fraction hard sphere glass is under oscillatory shear it is given enough energy to order into the entropically favorable crystal structure. This study focuses on the rheological properties of the glassy state and the differences to its shear induced crystal.

We have rheologically studied the crystallization process of the glass with increasing strain and probed the linear frequency dependence of both glass and shear induced crystal. The concentration dependence of the linear viscoelastic properties of the glass and crystal was compared. It shows a lower G' and G'' for the shear induced crystal. Additionally the comparison of the yield strains and Lissajous plots provided information on the shearing mechanisms of the crystal and the glass. The rheological aging was also probed, surprisingly revealing an increase of viscoelasticity not only for the glass, but also for the shear induced crystal.

Light Scattering Echo experiments and Brownian Dynamics Simulations were also carried out in order to complement the rheology experiments by showing the microscopic rearrangements of the hard spheres under shear. Light scattering-Echo from a crystal at rest showed larger de-correlation compared to the glass, verified by the increased in cage Mean Squared Displacements (MSD) found by the BD simulations. The MSD of both the glass and the crystal under shear were extracted from the simulations giving more insight to the crystallization process. Additionally the simulations allowed the visualization of the crystal slipping layers under oscillatory strain.

| | |
|--|-------|
| 1. Introduction | Pg.1 |
| 2. Background | |
| 2.1 Hard-sphere colloids | Pg.3 |
| 2.2 Rheology | Pg.6 |
| 2.3 Shear induced Ordering | Pg.11 |
| 2.4 Hard sphere Rheology | Pg.13 |
| 2.5 Hard sphere Crystallization under Shear | Pg.14 |
| 2.6 Hard spheres and Aging | Pg.15 |
| 3. Experimental setup and Systems and preparation | |
| 3.1 Sterically Stabilized PMMA Spheres | Pg.16 |
| 3.2 Sample Preparation | Pg.16 |
| 3.3 Rheometer Setup | Pg.17 |
| 4. Rheology | |
| 4.1 Creation of crystal | Pg.20 |
| 4.2 Linear rheology - Frequency dependence | Pg.32 |
| 4.3 Linear rheology - Concentration dependence | Pg.39 |
| 4.4 Yield Stress and Strain | Pg.45 |
| 4.5 Lissajous Stress-Strain | Pg.49 |
| 4.6 Aging | Pg.51 |
| 5. Dynamic Light Scattering Echo | |
| 5.1 Introduction | Pg.55 |
| 5.2 Experimental Setup | Pg.58 |
| 5.3 Results - Discussion | Pg.59 |
| 6. Brownian Dynamics Simulations | |
| 6.1 Introduction | Pg.65 |
| 6.2 Algorithm Details | Pg.67 |
| 6.3 Simulation runs – Results | Pg.69 |
| 7. Conclusions | Pg.89 |
| 8. References | Pg.91 |

1. Introduction

A colloidal dispersion is a type of homogeneous mixture. A colloid consists of two phases: a dispersed phase in a continuous phase. In a colloid, the dispersed phase is made of tiny particles or droplets that are distributed evenly throughout the continuous phase. The size of the dispersed phase particles are between typically 10 nm and 1000 nm in at least one dimension. Many familiar substances, including butter, milk, cream, aerosols (fog, smog, smoke), asphalt, inks, paints, glues and foam are colloids. Milk is a liquid colloid (fat) suspended in a liquid medium (water). Fog is a colloid system of water particles suspended in air. In this work we examine the case of solid colloidal particles suspended in a liquid medium.

Colloids interact with each other with van der Waals, electrostatic, excluded volume and steric forces. The interaction between two dipoles which are either permanent or induced can cause a force between two particles. Even if the particles do not have a permanent dipole, fluctuations of the electron density gives rise to a temporary dipole in a particle. This temporary dipole induces a dipole in particles nearby. This causes an attraction between the dipoles and is known as van der Waals force. It is always present, it is short range and attractive. When colloidal particles carry an electrical charge they can attract or repel each other. The charges of both the continuous and the dispersed phase, as well as the mobility of the phases are factors affecting this interaction. The excluded volume repulsion refers to the impossibility of any overlap between hard particles. Lastly, steric forces between polymer-covered surfaces can modulate interparticle forces, producing an additional repulsive steric stabilization force.

Stabilization serves to prevent colloids from aggregating due to attractive forces. Steric stabilization and electrostatic stabilization are the two main mechanisms for colloid stabilization. With steric stabilization the particles are coated with a layer of polymer that induces repulsion due to polymer chain excluded volume. Electrostatic stabilization is based on the mutual repulsion of same electrical charges. Small particle sizes lead to enormous surface areas, and this effect is greatly amplified in colloids. The particles used in this work have been sterically stabilized.

Colloids are found in a wide range of consumer and industrial products such as paints and shampoos. A greater understanding of the underlying principles that govern the behavior and properties of these products is of great interest to manufacturers. Many products are sold in metastable states and consequently their study is of particular interest.

Added to the general interest surrounding colloids, shear induced colloidal crystals have an added technological interest, because the application of shear could be used to assemble colloidal crystals for use in photonic or other applications.

In physics, colloids are an interesting model system for atoms. Many of the forces that govern the structure and behavior of matter, such as excluded volume interactions or electrostatic forces govern the structure and behavior of colloidal suspensions. For example, the same techniques that can be used to model ideal gases can be used to model the behavior of a hard sphere colloidal suspension. The colloidal length scale is comparable to the wavelength of light making both light scattering and optical microscopy valuable research tools. The added possibility of tuning the size and interactions of colloidal particles combined with the accessibility of the particles to optical techniques make them a lucrative atomic modeling system.

This thesis presents a study of the oscillatory shear response of hard sphere colloidal glasses and their shear induced crystal counterparts. It has been known that colloidal particles of this sort crystallize under shear, but no rheological measurements had been made that determined the mechanical properties of the crystal and compared them to the metastable glass. We also make comparison of glass and crystal by looking at the particle rearrangements during oscillatory shear by light scattering echo and computer simulations.

2. Background

2.1 Hard Sphere Colloids

The system studied in this work is ideally the simplest conceivable particle dispersion. Colloidal hard spheres are ideally microscopic particles moving within a medium with Brownian motion that interact with an infinite repulsive potential when they touch. Figure 2.1.1 shows the potential $V(r)$ as $V(0 < r < 2R) = \infty$ and $V(r > 2R) = 0$, where R is the particle radius. Hard spheres have no energy scale ($V(r)$ is independent of temperature) so we only need to consider entropy to determine phase behavior (Poon and Pusey 1995, Laird et al. 1987, Hoover et al. 1968). We can thus characterize this system by the number density of the particles alone. This is expressed in colloid volume fraction Φ ,

$$\Phi = \frac{4}{3} \pi R^3 \frac{N}{V}$$

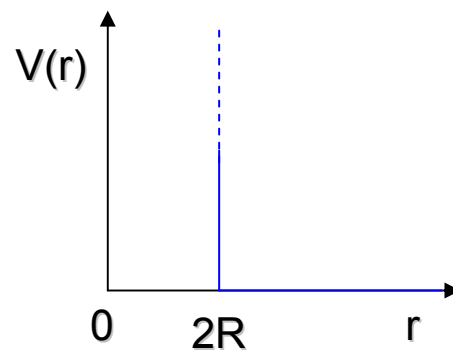


Figure 2.1.1: The pair potential of hard sphere particles of uniform radius R and centre to centre separation r .

As mentioned in the introduction, Van der Waals attractive forces may cause colloidal particles to aggregate irreversibly. This attraction is sufficiently long ranged (r^{-1} for $r < R$) to be able to affect particles in the size range of colloids. The resulting attractive potential has strength proportional to the refractive index mismatch between solvent and particle (Hamaker constant), that can be many times that of the thermal energy of the particles. This makes it important to stabilize the colloids to prevent aggregation. (Poon and Pusey 1995)

The method used to stabilize the particles in this work is steric stabilization. Small polymer chains are densely grafted on the surface of the colloidal particles. When two particles approach the polymer layers interpenetrate resulting in the reduction of entropy of individual chains. This causes a strong repulsion between the two polymer layers preventing the particles from getting close enough for the Van der Waals forces to become significant. If the grafting density and length of the chains are properly tailored, the resulting potential for sterically stabilized particles is a good approximation of a hard sphere potential.

2. Background

Another issue of the experimental implementation of hard spheres is polydispersity. Highly polydisperse hard sphere systems are unable to crystallize, but are still able to reach an arrested glassy state at $\phi=0.58$. As polydispersity rises, crystallization dynamics become slower as different particles sizes are not easily accommodated in the crystal lattice. At about 10% polydispersity, the distribution of sizes is too large and the crystal is not created at all (Poon and Pusey 1995, Schöpe et al. 2007).

As mentioned before, there is no temperature/energy scale for hard spheres, so there is only one parameter which completely determines the phase behavior. This is the particle volume fraction Φ . Hard spheres exhibit a liquid phase at volume fractions beneath 0.494, where the particles are free to diffuse and explore the whole volume available. A liquid-crystal coexistence phase is observed at volume fractions ranging from 0.494 to 0.545 and a fully crystalline structure from 0.545 to 0.58. Due to the large particle sizes of these colloidal crystals, they are extremely weak compared to atomic crystals and can be destroyed by gently shaking the sample cell. As hard spheres cannot overlap, the maximum packing in an ordered state is $\Phi_{MAX} \approx 0.74$. If the particles form an amorphous random close packed structure then the maximum packing fraction is $\Phi_{RCP} \approx 0.64$ (Schaertl and Sillescu 1994). The liquid-crystal coexistence phase has a linear dependence of crystal volume to volume fraction that makes it possible from the relevant heights of the phases to accurately determine volume fraction (Ackerson 1990).

Entropy is the driving force behind the crystallization of hard sphere colloids. It may seem counterintuitive that the increase of entropy leads to an ordered state, however the crystal structure gives freedom of movement to each particle around their lattice site by increasing individual free volume. Even though the particles are in an ordered state, the increase of entropy due to individual motion and free volume is greater than the reduction of the configurational entropy (Poon and Pusey 1995).

By increasing the volume fraction further the hard sphere particles reach a metastable state. Over 0.58 the particles are unable to move into the entropically favorable crystal positions due to space restrictions and become trapped in a dynamically arrested glass phase (Pusey and van Megen 1986). Figure 2.1.2 shows the hard sphere phase diagram.

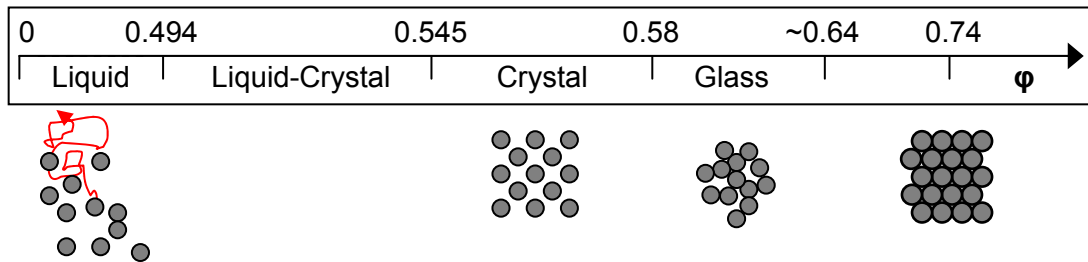


Figure 2.1.2 Phase behaviour of a suspension of monodisperse hard spheres

The crystal structures in which hard spheres assemble to when left at rest are a mixture of face-centred cubic (FCC) and hexagonally close packed (HCP) regions that are randomly oriented (Pusey et al. 1989). As seen in figure 2.1.3 the FCC crystal (in the shearing plane, as will be shown later) is defined by hexagonal layers of spherical particles one on top of the other. The HCP crystal is similar, but instead of the three repeating layers of the FCC (ABCAB...), the HCP has two (ABABA...). If left for long periods of time, it was found that this mixture of random HCP and FCC structures will gradually age into a pure FCC crystal. (Kegel and Dhont 1999 & Martelozzo et al. 2002). Small mechanical perturbations also seemed to favour the FCC structure.

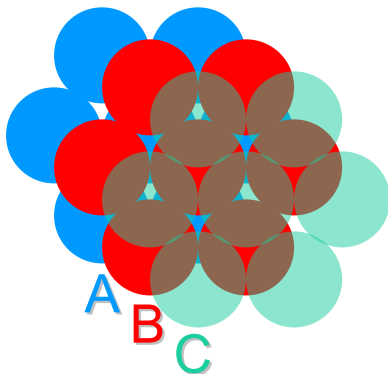


Figure 2.1.3: FCC crystal representation

2.2 Rheology

Rheology is a science that deals with the flow and elasticity properties of materials. The name comes from the Greek word “ρῶή”, which means “flow”. It has been extensively used for characterizing polymers and aiding in the industrial processing of polymeric products. The macroscopic properties probed by rheology can be used to glimpse into the microscopic structure and yield important time and size scales. This information is extracted from the material through deformation and subsequent measurement of the force response.

Linear Viscoelasticity

Consider the deformation geometry of simple shear, sketched in Fig. 2.2.1. The material being sheared is between two flat rigid surfaces. The adhesion between the material and the surfaces is assumed to be strong enough that there is no slippage at either surface. The shear stress σ_{xy} (called here σ for short) in this simple shear is defined as the ratio of the applied force and the cross-sectional area of the surfaces A , which is also the area of any plane perpendicular to the y -direction within the material being sheared.

$$\sigma = \frac{F}{A} \quad (\text{Eq. 2.2.2})$$

The shear strain is defined as the displacement of the top plate Δx relative to the thickness of the sample h (see Fig. 2.2.1).

$$\gamma = \frac{\Delta x}{h} \quad (\text{Eq. 2.2.3})$$

By defining the stress and strain in this fashion, each part of the entire sample being sheared has identical shear stress σ and shear strain γ , in simple shear, as long as the material shears uniformly.

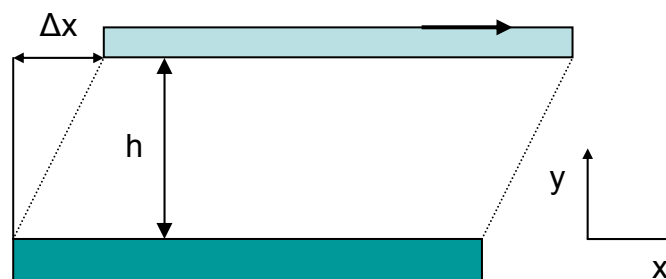


Figure 2.2.1: Deformation in simple shear requires application of equal and opposite forces to the two plates. The figure is a 2-dimensional representation.

If the material between the surfaces is a perfectly elastic solid, the shear stress σ and shear strain γ are proportional, with the constant of proportionality defining the shear modulus G .

2. Background

$$G = \sigma / \gamma \text{ (Eq. 2.2.4)}$$

Since the stress has units of force/area and the strain is dimensionless, the modulus has units of force/ area. Equation 2.2.4 is Hooke's Law of Elasticity and it is valid for all solids at sufficiently small strains.

On the other hand, if the material between the surfaces is a simple liquid, the stress is identically zero at any constant strain γ . In liquids, the stress is determined by deformation rate. The rate of change of shear strain with time is called the shear rate.

$$\dot{\gamma} = \frac{d\gamma}{dt} \text{ (Eq. 2.2.5)}$$

If the top plate moves with a constant velocity v , as seen in figure 2.2.6, the shear rate is $\dot{\gamma} = v / h$. For simple liquids, the shear stress σ is linearly proportional to shear rate $\dot{\gamma}$, with the constant of proportionality defining the shear viscosity η .

$$\eta = \sigma / \dot{\gamma} \text{ (Eq. 2.2.7)}$$

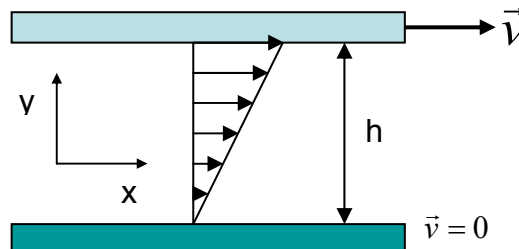


Figure 2.2.6: Steady rate deformation in simple shear geometry. The top plate moves in the x direction with a constant speed, while the bottom plate remains stationary.

This relation is Newton's Law of Viscosity and liquids that obey it are referred to as Newtonian liquids. Since the stress has units of force / area and the shear rate has units of reciprocal time, the viscosity has units of force time/area.

Materials such as polymers and colloidal suspensions are viscoelastic, meaning that they have intermediate properties between Newtonian liquids and Hookean solids.

Oscillatory Shear

A simple viscoelastic measurement that has become very easy to implement with the advent of modern electronics is oscillatory shear. A sinusoidal strain with angular frequency ω is applied to a sample in the simple shear geometry.

$$\gamma(t) = \gamma_0 \sin(\omega t) \quad (\text{Eq. 2.2.8})$$

The principle advantage of this technique is that the viscoelastic response of any material can be probed directly on different time scales ($1/\omega$) of interest by simply varying the angular frequency ω . If the material studied is a perfectly elastic solid, then the stress in the sample will be related to the strain through Hooke's Law (Eq. 2.2.4).

$$\sigma(t) = G\gamma(t) = G\gamma_0 \sin(\omega t) \quad (\text{Eq. 2.2.9})$$

The stress is perfectly in-phase with the strain for a Hookean solid, as shown in Fig. 2.2.10. On the other hand, if the material being studied is a Newtonian liquid, the stress in the liquid will be related to the shear rate through Newton's Law (Eq. 2.2.7).

$$\sigma(t) = \eta \frac{d\gamma(t)}{dt} = \eta\gamma_0\omega \cos(\omega t) \quad (\text{Eq. 2.2.11})$$

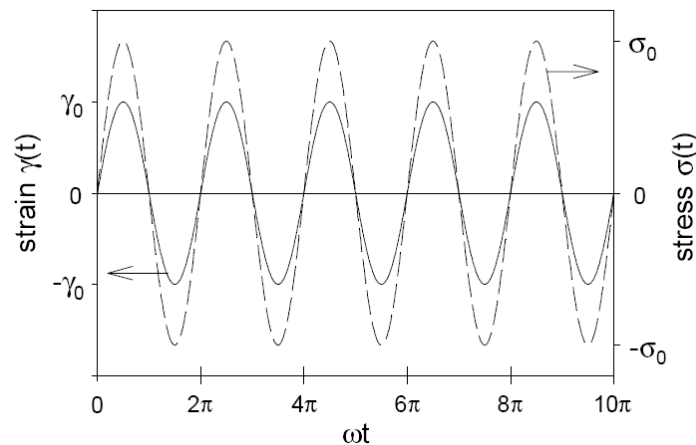


Figure 2.2.10: Oscillatory strain (solid curve and left axis) and oscillatory stress (dashed curve and right axis) are in-phase for a Hookean solid.

The stress in a Newtonian liquid still oscillates with the same angular frequency ω , but is out-of-phase with the strain by $\pi/2$, as shown in Fig. 2.2.12. More generally, the linear response of a viscoelastic material always has the stress oscillate at the same frequency as the applied strain, but the stress leads the strain by a phase angle δ .

$$\sigma(t) = \sigma_0 \sin(\omega t + \delta) \quad (\text{Eq. 2.2.13})$$

In general, δ can be frequency dependent, with any value in the range $0 < \delta < \pi/2$. The two simple cases already treated correspond to the limits allowed for the phase angle. Solids that obey Hooke's Law have $\delta = 0$ at all frequencies, while liquids that obey Newton's Law have $\delta = \pi/2$ at all frequencies. Since the stress is always a sinusoidal function with the same

2. Background

frequency as the strain, we can separate the stress into two orthogonal functions that oscillate with the same frequency, one in-phase with the strain and the other out-of-phase with the strain by $\pi/2$.

$$\sigma(t) = \gamma_0 [G'(\omega) \sin(\omega t) + G''(\omega) \cos(\omega t)] \quad (\text{Eq. 2.2.14})$$

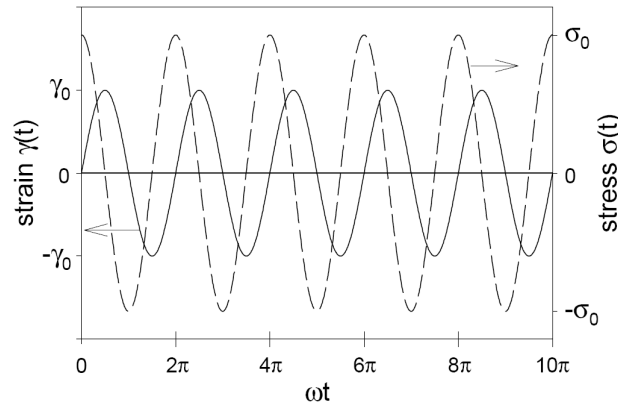


Figure 2.2.12: Oscillatory strain (solid curve and left axis) and oscillatory stress (dashed curve and right axis) are out-of-phase for a Newtonian liquid. The stress leads the strain by phase angle $\delta = \pi/2$.

The above equation defines $G'(\omega)$ as the storage modulus and $G''(\omega)$ as the loss modulus. Equation 2.2.14 can be related to the previous equation for the stress in oscillatory shear using the trigonometric identity for the sine of a sum.

$$\sin(\omega t + \delta) = \cos \delta \sin(\omega t) + \sin \delta \cos(\omega t) \quad (\text{Eq. 2.2.15})$$

This suggests that the storage and loss moduli can be related to the phase angle and the modulus amplitude σ_0/γ_0 at each frequency ω .

$$G' = \frac{\sigma_0}{\gamma_0} \cos \delta \quad (\text{Eq. 2.2.16})$$

$$G'' = \frac{\sigma_0}{\gamma_0} \sin \delta \quad (\text{Eq. 2.2.17})$$

The ratio of storage and loss moduli is the tangent of the phase angle, called the loss tangent.

$$\tan \delta = \frac{G''}{G'} \quad (\text{Eq. 2.2.18})$$

The storage and loss moduli are the real and imaginary parts of the complex modulus $G^*(\omega)$.

$$G^*(\omega) = G'(\omega) + iG''(\omega) \text{ (Eq. 2.2.19)}$$

Peclet Number

In order to quantify the effect of shear on a material, the Peclet number is introduced. It is mostly used for colloidal suspensions and is a measure of the relative importance of convective motion of shear flow to diffusive Brownian motion. It is a dimensionless number that is given by the shear rate $\dot{\gamma}$ multiplied by the time needed for a particle to diffuse a distance equal to its radius. $Pe = \dot{\gamma} \cdot \tau_B$, where $\tau_B = a^2 / D$ is the Brownian diffusion time. For the dilute regime $\tau_B = 6\pi\eta_S R^3 / K_B T$ and $Pe = 6\pi\eta_S R^3 \dot{\gamma} / K_B T$ (Bare Peclet). At $Pe \ll 1$, the Brownian diffusion is more important than the shear rate and the system's state closely resembles the system at rest (linear regime). If $Pe > 1$, the shear rate becomes important compared to Brownian motion and the system moves out of equilibrium giving rise to non linear effects.

Experimental Geometries

When working with commercial rheometers to produce experimental data, the geometries differ from the simple shear geometry shown previously. Although the simple shear geometry is easy to understand, it is very hard to implement experimentally. To solve various implementation issues, experimental rheologists turned to rotating geometries such as the parallel plate and cone plate geometries shown in figure 2.2.20 and also the couette geometry.

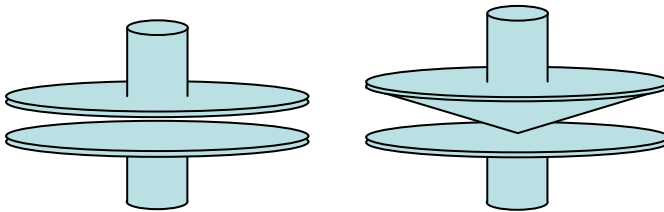


Figure 2.2.20: Illustration of the parallel plate (left) and cone plate (right) geometries used in experimental rheology.

The main difference between the two geometries is that the cone and plate has a homogenous strain field, whereas the parallel plates do not. This is especially important when doing non-linear measurements, as the validity of the response relies heavily on the assumption that the whole sample responds to applied strain in the same way. For linear measurements this assumption is true even in the case of parallel plates that apply non-homogenous strain. The cone and plate geometry was mostly used in this work as we focus on non-linear rheology.

2.3 Shear induced Ordering

Beyond the simplest system of hard spheres that is examined in this work, shear induced ordering has been witnessed in similar systems such as charged colloids (Chen et al. 1994), microgels (Paulin et al. 1996,1997, Stieger et al. 2004) and particles in aqueous medium (Panine et al. 2002). Paulin et al. (1996, 1997) studied the various forms of shear induced FCC structures in glassy PMMA microgels and found very different non-linear rheological properties as a function of strain (creep), but linear dynamic measurements showed small differences between changing structures. The study of concentrated PNIPAM microgels by Stieger et al. (JPCM, Langmuir 2004) showed the versatility of the system on the shear induced structures, while varying the temperature and changing interactions. Panine et al. (2002) were able to view the variations in the structure in hard sphere like particles and simultaneously monitor the elastic and loss moduli as the crystal was being formed. Experimental setups made to probe these systems included light (Paulin et al. 1996,1997), X-ray (Panine et al. 2002) and neutron scattering (Chen et al. 1994, Stieger et al. 2004) coupled with rheology.

Furthermore, simulations of crystallization on colloidal particles have been made for liquid charged particles (Blaak et al. 2004) and many jammed (Duff and Lacks 2007) systems. Duff and Lacks (2007) executed a range of different simulation techniques to examine the mechanism of shear induced ordering on jammed systems and deduced that ordering occurs as shear pushes the system to lower energy minima. A review of Vermant and Solomon (2005) summarizes and gives an overview of the more important work.

Denneman et al. (1999) developed a frequency dependent theory on the elastic properties of a square cubic charged colloidal crystal. More applicable to this work, Laird (1992) developed a theory on the elastic constants of BCC and FCC crystals using the Modified Weighted Density Approach.

There have also been indirect rheological measurements of a randomly oriented hard sphere crystal by Phan et al. (1999) showing an increase of elastic properties with volume fraction. Additionally, Schöpe et al. (1998) measured the elastic properties of the phase transition of BCC crystals to FCC crystals formed with charged latex spheres at rest. Vorst et al. (1995) made some dynamic linear measurements on charged crystals and developed a model that quantitatively fit their data.

More specific to this work on hard sphere particles, there have been direct observations of shear induced crystallization of hard spheres with microscopy (Haw et al. 1998) and light scattering experiments (Ackerson 1988, 1990), which show the structures and geometric flow characteristics and will be discussed in detail further down the text. Figure 2.2.1 shows a phase diagram of oscillatory shear induced ordering in hard spheres from Ackerson (1990).

2. Background

Amos et al. (2000) managed to fabricate hard sphere crystals with oscillatory shear in thin films giving rise to optical applications of shear induced crystallization. Derks et al. (2004) studied colloidal crystallization with a confocal microscope using a counter rotating cone plate shear cell and was able to image the shear behaviour of hard sphere crystals by looking at a stationary plane. Cohen et al. (2004) witnessed peculiar configurations under shear when colloidal spheres were confined to gaps of less than 11 particle diameters. Smith et al. (2007) developed a model to quantify under what application of shear a depletion hard sphere gel may crystallize. Even though this subject has been examined for many years, there still hasn't been a comprehensive rheological study of the shear induced crystal structure from a hard sphere glass.

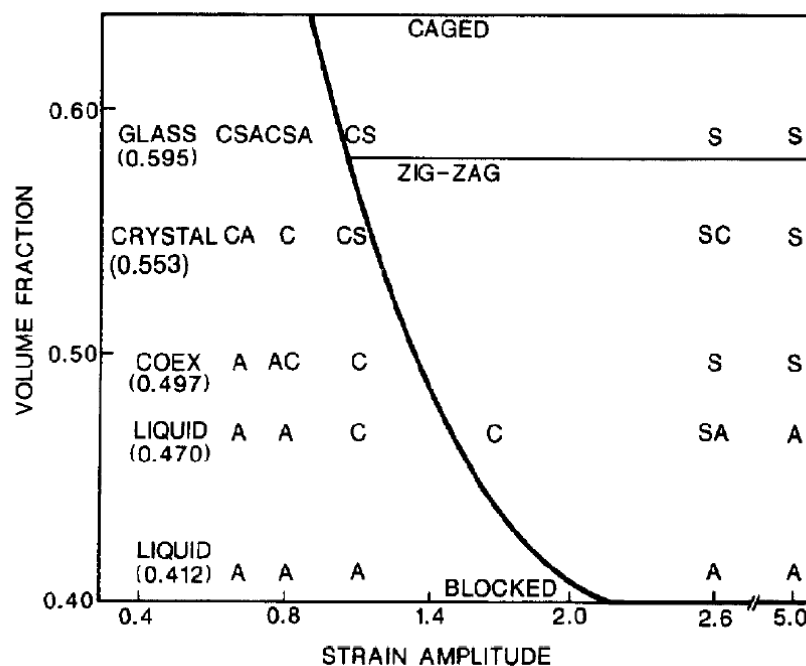


Figure 2.2.1: Phase diagram taken from Ackerson (1990) showing shear structure with volume fraction versus oscillatory strain (3.5 Hz) in a hard sphere system. C – FCC crystal order, S – layer ordering and A – amorphous order. The first letter shows the predominant ordering.

2.4 Hard sphere Rheology

Rheological measurements on hard spheres have been done in the past, mostly with polydisperse samples, as to not complicate results with shear ordering (Pusey 1987, Bartlett 1997). Older dynamic measurements on PMMA spheres with approximate hard interactions were done by Frith et al. (1990) showing a qualitatively similar frequency dependence to this work. Mewis and Vermant (2000) made a sum of viscosity, yield stress and shear thickening measurements and produced scaling relations allowing prediction of properties in different sized spheres. Petekidis et al. (2002, 2003) did some creep and some dynamic measurements coupled with DLS echo of a polydisperse hard sphere glass and concluded that it can tolerate a high amount of strain (10%-15%) before yielding irreversibly. Rao et al. (2006) conducted experiments on nanoparticle spheres with approximated hard interactions and high polydispersity showing the similarity of the rheological properties to hard spheres. Mason and Weitz (1995) measured the viscoelastic frequency dependence of silica hard spheres near the glass transition and successfully applied the Mode Coupling Theory to the resulting rheology. Koblelev and Schweizer (2005) presented a complete microscopic theory of glassy colloidal suspension under stress giving values including elastic moduli, viscosity and yield strains.

2.5 Hard sphere Crystallization under Shear

Work done by Haw et al. (1998) with a sliding parallel plate geometry (simple shear), shows that concentrated hard sphere systems tend to order under high enough oscillatory strains. If the volume fraction is over 0.545, a homogeneous crystal is created that remains stable. If the volume fraction is between 0.494 and 0.545 then the induced crystal appears in regions of the sheared sample, but still remains at the end of shear. In the case of volume fraction lower than 0.494 (liquid regime), ordering is seen during shear that dissolves after cessation of shear. If the hard spheres are in the glassy state ($\phi > 0.58$), the shear induced crystal does not revert to glass, but remains in the energetically preferable crystal state.

When the system under shear is in the glass regime, the crystal is formed with two orientations depending on the amount of strain. Either with the close packed direction parallel to shear ($\gamma > 50\%$) or with the close packed direction perpendicular to shear ($\gamma < 50\%$). Figure 2.3.1 shows a representation of the closed packed direction of the crystal at high and low strains. At low strains Haw would see that the crystal would have some sort of “polycrystallinity” as the sample would not be fully oriented in the perpendicular direction, but would have “grains” which had a preferred direction which was perpendicular to the shear direction. At high strains the sample would reorient parallel to shear and the “polycrystallinity” would disappear.

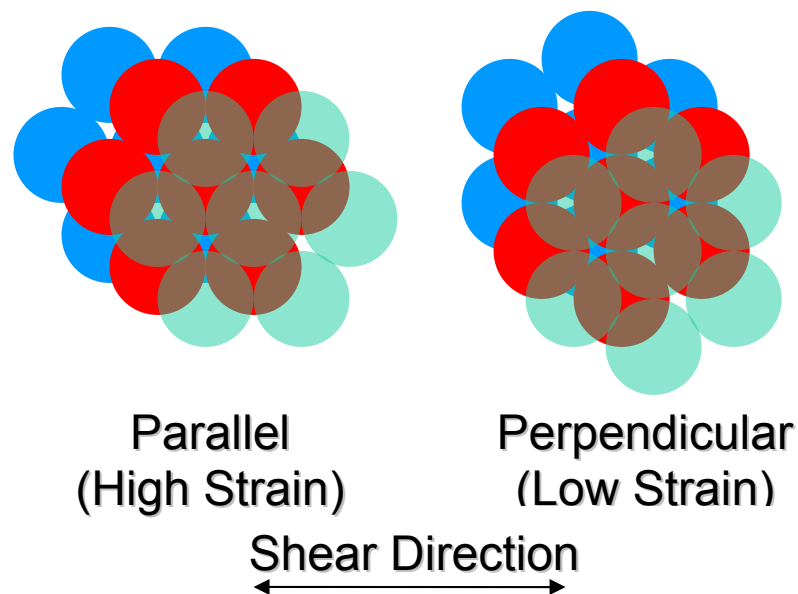


Figure 2.3.1: Representation of close packed direction of crystal parallel and perpendicular to shear

2.6 Hard spheres and Aging

As the volume fraction is increased, the motion of the particles slows down. The glass transition at 0.58, occurs when the system turns into a physically arrested state where each particle is trapped by its neighbours. In this metastable state, the system is far from the energetically preferred crystal structure and slowly explores the energetic landscape finding new minima with time (Bouchaud 1999, Cipelletti and Ramos 2005). This translates to the aging of the hard sphere system at volume fractions higher than the glass transition.

Aging manifests itself in many properties of a glassy system including particle mean square displacement, relaxation times and viscoelasticity. Specifically for the aging processes of hard sphere systems there have been measurements of mean square displacements with microscopy (Courtland and Weeks 2003) and time evolution experiments with light scattering (Masri et al. 2005), but there seem to be no previous experiments on viscoelasticity. For other similar glassy colloidal systems it has been found that at rest, the linear viscoelastic properties tend to increase logarithmically or exponentially. Examples of these are systems of charged spheres (Derec et al. 2003), which are very similar to hard spheres and seem to age logarithmically and also Laponite systems, which were found to age exponentially (Bonn et al. 2002, Abou et al. 2001).

Under oscillatory shear glassy colloids exhibit three distinct regimes of strain. a) Very low strains in the linear regime that do not perturb the internal mechanics and do not change the way the sample ages at rest, b) Mid range strains above the linear regime that cause increase in aging compared to aging at rest (overaging) and c) High strains which cause decrease in aging (underaging) or even complete rejuvenation to the initial rheological state of the system. This behaviour has been seen experimentally in glassy systems of charged spheres (Viasnoff et al. 2002, 2003) and has been the theme of molecular simulations (Lacks and Osborne 2004). Although overaging has not been seen in all cases (Kaloun et al. 2005), there is a clear picture of rejuvenation at high strains. The true nature of shear rejuvenation and whether it literally rejuvenates a glassy material is currently under debate (Isner and Lacks 2006).

There seems to be no previous literature on the rheological aging of shear induced crystal or any other shear induced colloidal crystal, but as previously mentioned, there have been experiments on the evolution of random hard sphere crystallites to pure FCC (Kegel and Dhont 1999 & Martelozzo et al. 2002). In addition, it has been seen in other systems (Mazoyer et al. 2006), that temperature fluctuations affect aging processes, possibly due to internal stresses introduced by temperature fluctuations that overage or underage the system depending on the shear rate as mentioned above.

3. Experimental Setup and Systems

3.1 Sterically Stabilized PMMA Spheres

The hard sphere particles used in this work consist of polymethylmethacrylate (PMMA) cores sterically stabilized by thin (≈ 10 nm) chemically grafted layers of poly-12-hydroxystearic acid (PHSA) chains. The particles were dissolved in cis-decahydronaphtalin (cis-decalin) making a good approximation of hard sphere particle interactions shown by Bryant et al. (2002). For long time aging experiments, particles were dissolved in octadecene, eliminating the effect of solvent evaporation. The radii of the particles used, which was measured by light scattering, are $R_C=689$ nm and $R_C=267$ nm in cis-decalin and $R_C=288$ nm in octadecene. Both particle suspensions had low enough polydispersities to be able to crystallize under shear ($\sim 5\%$). Due to sedimentation issues, the larger spheres will not be presented for aging measurements and because of severe shear thickening at high strains, non linear measurements will generally be omitted.

3.2 Sample Preparation

In order to determine the volume fraction for a monodisperse hard sphere sample, the usual procedure is to reach the coexistence regime through dilution or evaporation and derive a value from the crystal to liquid ratio of the sample. Because of high refractive index mismatch in octadecene and rapid sedimentation when using the larger spheres, the coexistence region in those cases could not be found.

In the case of the smaller spheres in cis-decalin, the coexistence region was found and we were able to calibrate the sample accordingly. Due to unknown reasons though, when the samples were submitted to centrifugation, the experimental random close packing fraction was close to the value of 0.70 which is very far from the value of 0.64 expected for monodisperse spheres. Details on how the volume fraction is calculated from the coexistence can be found in the paper of Ackerson (1990).

Thus in order to have the same conditions for all the samples used, they were first centrifuged until all the excess solvent was expelled from the colloid and the sample was separated to a randomly close packed colloid and solvent. The volume fraction value of 0.660, which was derived from computer simulations (Schärfl and Sillescu 1994), was used to determine random close packing by centrifugation. The standard deviation of the volume fraction derived this way is $\sigma_\phi=\pm 0.006$. The rest of the sample concentrations were determined by successive dilutions of the same sample batch. This means that even though the absolute volume fraction of a sample may generally have a large deviation because of random close packing,

the error in the determination of the volume fractions in the same batch is small (of the order of the weight determination error, typically much less than 0.1% for each dilution).

The following equation was used to calculate volume fractions when dilution or evaporation occurred:

$$\Phi = \Phi_0 \left[1 + \frac{m_s}{m_c} \left(1 + \frac{\Phi_0 (\chi - 1)}{1 + a\chi} \right) \right], \text{ where } \chi = \frac{\rho_c}{\rho_s} \text{ (Eq.3.2.1)}$$

with Φ as the new volume fraction, Φ_0 the old volume fraction, m_s the mass of the added solvent, m_c the mass of the colloidal suspension, ρ_c the density of the dry colloid and ρ_s the density of the solvent. a is a parameter used to compensate for the fact that the spheres do not have the same density when in solvent, but have an increased radius due to the stabilizing layer. For the colloid $\rho_c=1.188 \text{ gr/cm}^3$ in all cases, and for the solvents $\rho_{\text{decalin}}=0.897 \text{ gr/cm}^3$ and $\rho_{\text{octadecene}}=0.788 \text{ gr/cm}^3$. For a we used a typical value of $a=0.12$.

3.3 Rheometer Setup

In order to observe crystallization a transparent geometry was needed. Although some tests were made using the simpler setup of parallel glass plates, inhomogeneous strain throughout the sample led to partial crystallization and consequently problematic measurements. To properly conduct rheology measurements on the crystal structure, it was decided that cone and plate geometry was essential. A homemade transparent Plexiglas cone was constructed which had a diameter of 38mm, an angle of 0.03 rad and was insoluble in the solvents used during these experiments. This cone was used as the bottom stationary part of the geometry, while a rotating parallel glass plate was used for the top. We tested the homemade geometry against a factory made 25mm titanium cone and it had satisfactory performance (Figure 3.3.1). With a high viscosity oil standard the two geometries showed negligible differences, but with a viscoelastic standard there were differences in moduli up to 7%. This difference can easily be attributed to the loading procedure as the sample is very stiff. For this sample even between factory made geometries there are differences up to 12%. The gap distance was large enough to avoid confinement effects (Cohen et al. 2004).

3. Experimental Setup and Systems

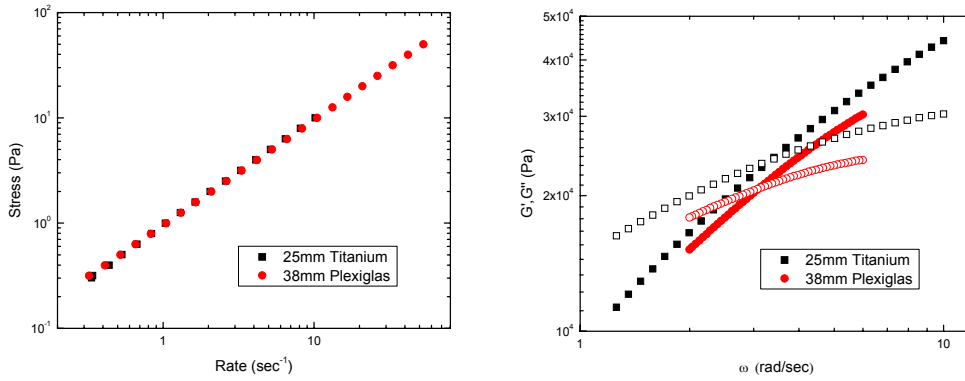


Figure 3.3.1: Comparison between factory made and homemade Plexiglas cone with a high viscosity standard (left) and a highly viscoelastic standard (right).

In order to view and quantify crystallization a laser beam was passed through the bottom of the sample and the scattered pattern appeared on a paper screen. This can be seen in figure 3.3.2. With the scattered pattern we were able to see the amount of crystallization, but also the type and orientation of the crystal structure. If the dispersion was in the glass state (amorphous), a Debye-Scherrer ring could be seen on the screen, whereas if crystallized, Bragg peaks would appear, giving an insight on the induced structure. When the sample was semi-crystallized, a mixture of both scattering patterns could be seen. An example of the scattering patterns expected for parallel and perpendicular shear induced crystal is shown in the insets of figure 3.3.3, which are the Fourier transformations of the microscope images of a sample at $\phi=0.56$ under shear.

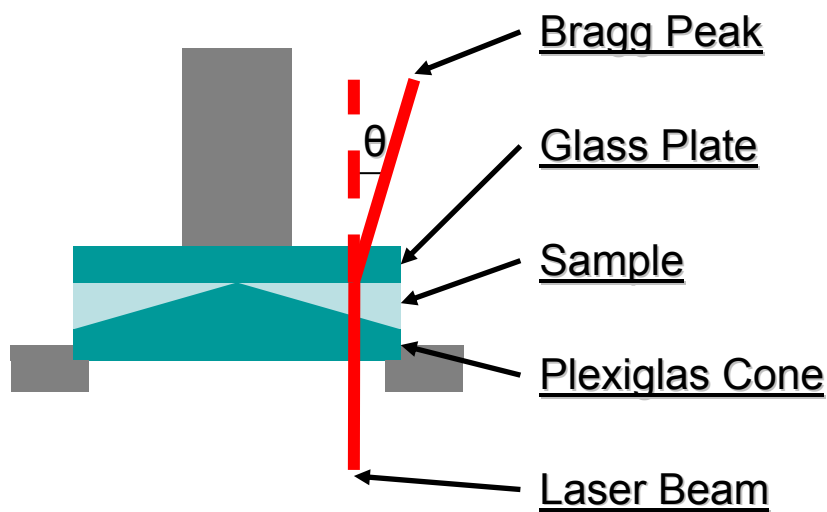


Figure 3.3.2: Representation of the experimental setup used to view crystallization under shear.

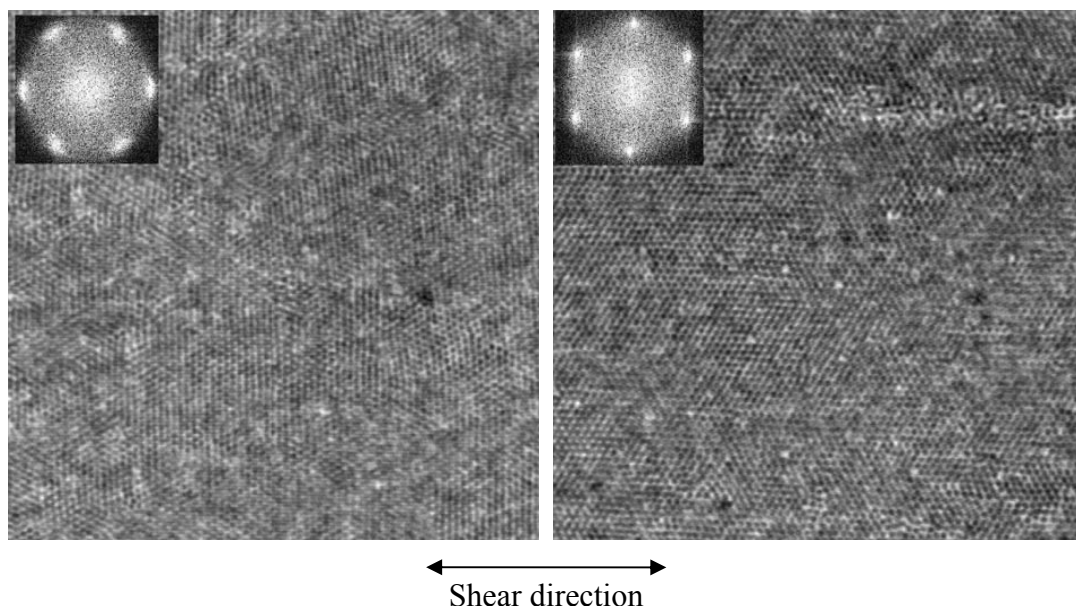


Figure 3.3.3: Microscope images of shear induced crystal at low strain (left) and high strain (right). Insets show Fourier transformation of images (equivalent of Bragg peaks) (Haw et al. 1998).

A Rheometric Scientific stress controlled DSR Rheometer was used for all the measurements involving optical observations (Torque Range: 0.01-200 gr-cm). At the expense of optical feedback, a Rheometric Scientific strain controlled ARES Rheometer was also used in any case that constant strain, Peltier temperature stabilization or Echo measurements were needed (Torque Range: 0.004-10 gr-cm with one transducer and 0.04-100 gr-cm with the second). For the small spheres we used a green laser ($\lambda=532\text{nm}$) and for the larger spheres a red laser ($\lambda=633\text{nm}$). For samples in cis-decalin, sealing the area around the sample with water minimized solvent evaporation. Before every measurement the samples were thoroughly mixed and experiments started immediately after loading. All the measurements were made at a constant temperature of 20°C and loading history was erased before starting measurements by applying a low rate steady shear for about 10 seconds so as to destroy any crystal induced by loading. The amorphous Debye-Scherrer ring on the scattering screen verified the absence of crystal.

4. Rheology

4.1 Creation of crystal

The basic idea is to create the crystal and compare the rheology of this crystal to the glass at same volume fraction. To achieve this we start oscillatory shear at a specific frequency, from low stresses and keep increasing the stress until full crystallization occurs. After the crystal is created we then view the crystal's response to strain with the same process for decreasing stress. This type of test is called a Dynamic Stress Sweep or for short DSS.

In Figures 4.1.1 and 4.1.2 and 4.1.3 we show the DSS measurements of four different volume fractions in cis-decalin, in the glass regime (0.599, 0.608, 0.628, 0.644). The measurements were conducted at a frequency of 10 rad/sec and were plotted as a function of strain instead of stress, since yield strain is expected to depend on volume fraction much less than yield stress (Petekidis et al. 2002). A more detailed view of the process to be discussed is seen in figure 4.1.1. The measurements start out from the linear regime of the glass, which lasts until about 1% strain where shear thinning begins to appear (Regime a). At about 10-20% strain, around the G' , G'' crossover, which may define the yield strain (b), Bragg spots begin to appear, indicating the onset of crystal creation. At this point, the Bragg spots are still faint and the underlying image of the Debye-Scherrer ring dominates. As the strain increases, the amorphous ring disappears as it is being replaced by more intense Bragg peaks. At a strain of about 100% full crystallization is achieved and only the high intensity Bragg peaks remain (c). The speed of crystal creation and stabilization was dependent on the amount of shearing time, so in order to approach equilibrium for each point the number of points and the shearing time of each point were large. Typical values were of 30 points per stress decade at 30 cycles per point. Applying higher strains (>150%) led to disruption of the crystal structure and an increasing reappearance of the amorphous ring (Regime d). Measurements at high volume fractions would additionally exhibit shear thickening at these high strains. This was more evident for the large spheres as expected (Maranzano and Wagner 2001) and was systematically avoided.

The second graph of figure 4.1.1 depicts the DSS at decreasing strain in which we probe the crystal structure once it has been created. If upon increasing the strain, the crystal starts breaking when high strains are reached, on decreasing the strain, the crystal is reformed (e). This can be seen by the intensity of the Bragg peaks. Hence the sharp drop of G' and G'' when reducing strain seen in the second graph of figure 4.1.1. (and both graphs of figure 4.1.2). If the crystal does not start dissolving during strain increase, the backward sweep probes the crystal structure in reverse as shown in figures 4.1.3a and 4.1.3b. In all these measurements the most obvious and interesting finding is the drop of both G' and G'' going from glass to crystal that increases with volume fraction and can be more than one order of magnitude. Performing a second increasing DSS reveals little hysteresis of the crystal

structure. In the third graph of figure 4.1.1 and in 4.1.2 the second forward DSS is also shown. At the point where G' and G'' of the first (glass) and third (crystal) forward DSS begin to merge (f), the crystal structure is optically observed to begin breaking. There is a mixture of Bragg peaks and an amorphous ring until the strain reaches point (d) where the crystal dissolves completely and the Bragg peaks disappear.

There seems to be a small difference in the crystallization sweep of the spheres in octadecene. The whole process is identical, but the spheres in octadecene fully crystallize at a smaller strain. Instead of a strain of about 120% which the spheres in cis-decalin crystallize, the spheres in octadecene fully crystallize at a strain of 70%. This could be due to some small attractive interactions between particles, but this will be discussed further down in the text.

An attempt was made to rheologically observe crystallization for the larger spheres in a similar fashion, but due to shear thickening complications, the system became too difficult to study. Shear thickening is caused by hydrodynamic effects at high shear rates that jam the particles and expunge the solvent from around the spheres creating a temporary solid. If this happens when the sample is being measured, it could be spilled out of the geometry, it could insert bubbles in the sample or at best, create a situation in which the sample needs a large amount of time to relax back to equilibrium. An example of a dynamic stress sweep for the larger spheres ($R=689\text{nm}$) similar to those presented before is seen in figure 4.1.4. The onset of shear thickening begins at 30% and Bragg spots are evident after 10% strain. Full crystallization is finally achieved at about 100% strain despite the onset of shear thickening and at even higher strains ($>150\%$) the crystal brakes down. The jumps in stress caused by shear thickening make it difficult to interpret rheological behaviour and understand why crystallization occurs.

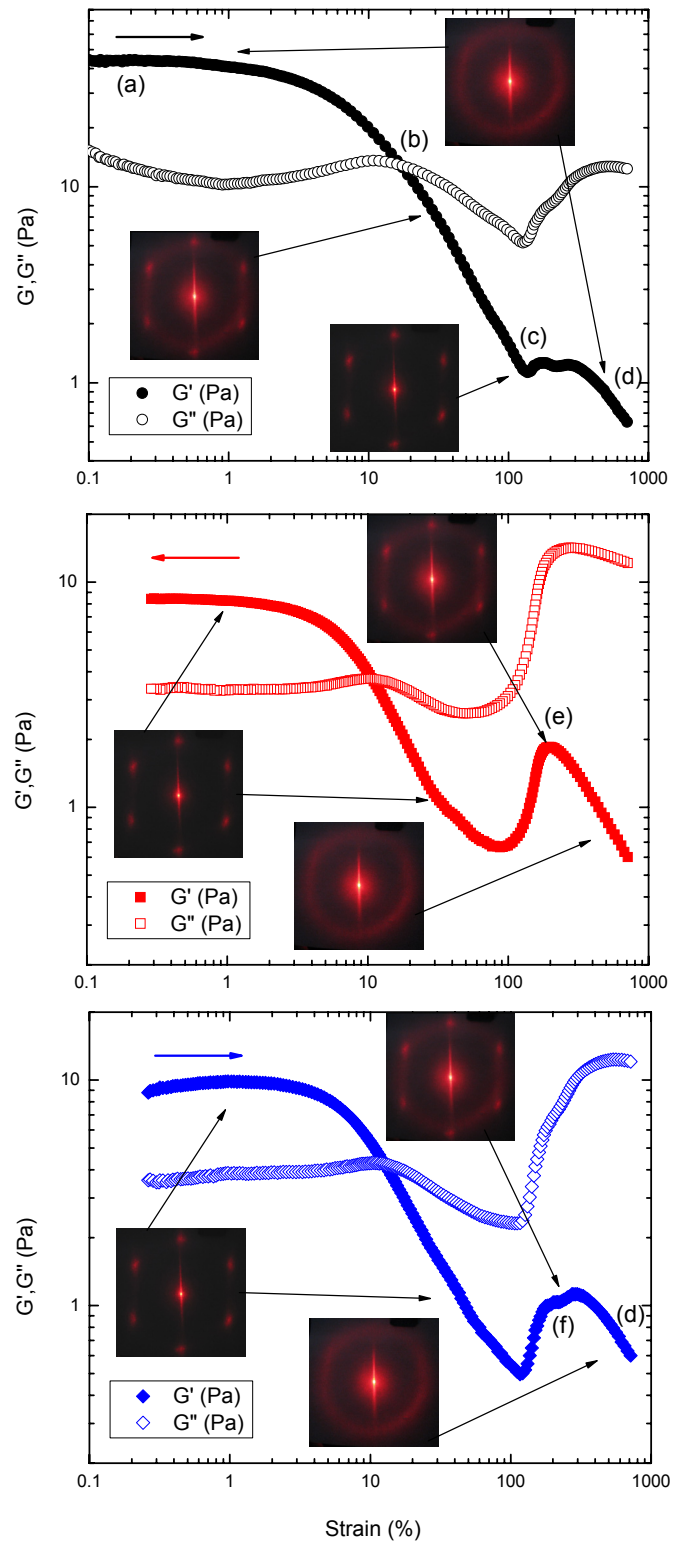


Figure 4.1.1: Dynamic strain sweeps of $\phi=0.599$ in cis-decalin at a frequency of 10 rad/sec. The solid points are values of G' and the hollow points of G'' . The three consecutive DSS are plotted in the order of execution as discussed in the text. The letter notations show critical strain points in the crystallization process and the scattered patterns for different stages of crystallization are shown in the inset photos.

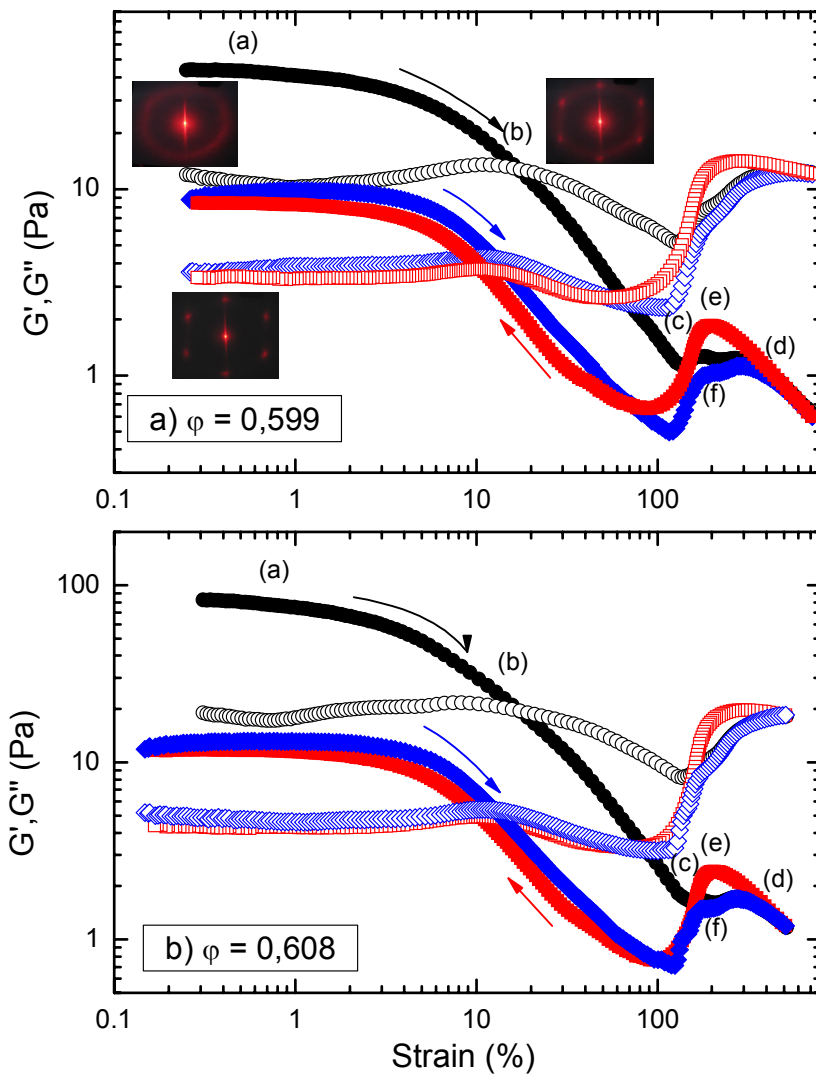


Figure 4.1.2: Dynamic strain sweeps of lower hard sphere glass volume fractions in cis-decalin a) 0.599, b) 0.608 at a frequency of 10 rad/sec. The solid points are values of G' and the hollow points of G'' . The arrows indicate the direction of changing strain and the letter notations show critical strain points in the crystallization process discussed further in the text. The scattered patterns for different stages of crystallization are again shown in the inset photos of subfigure a).

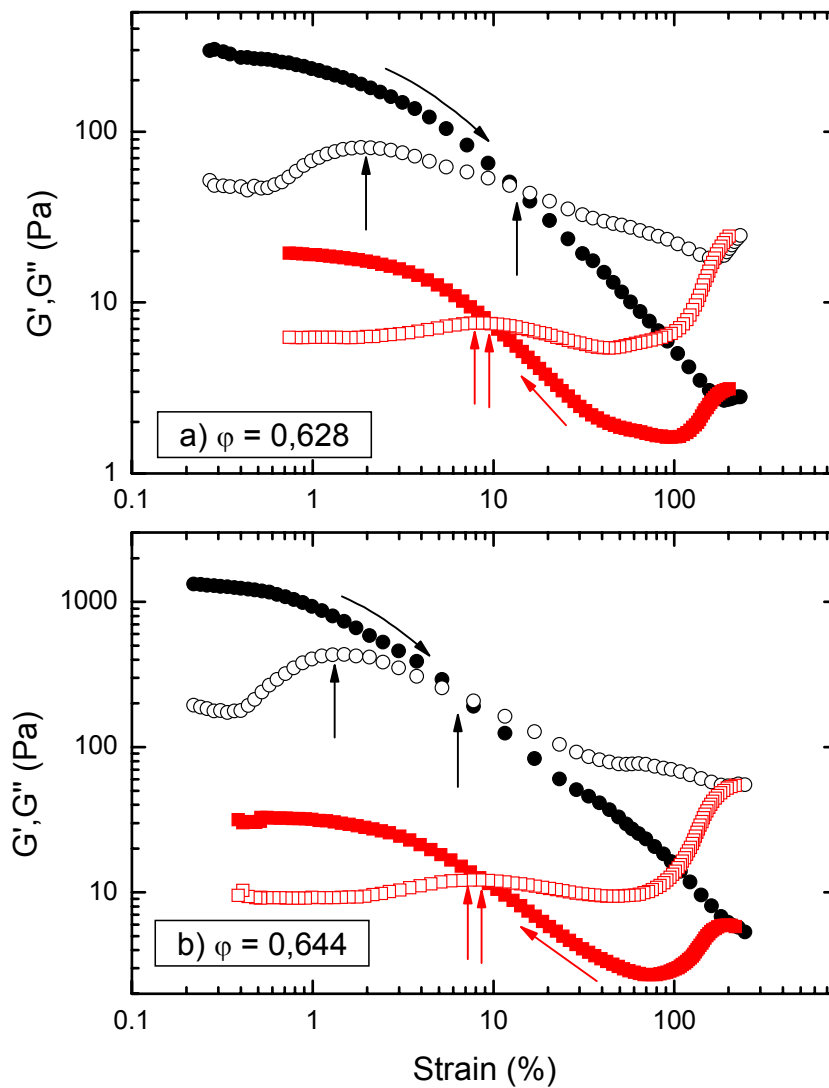


Figure 4.1.3: Dynamic strain sweeps of higher hard sphere glass volume fractions in cis-decalin a) 0.628, b) 0.644 at a frequency of 10 rad/sec. The solid points are values of G' and the hollow points of G'' . The vertical arrows show the yielding and crossover points and the other arrows indicate the direction of changing strain.

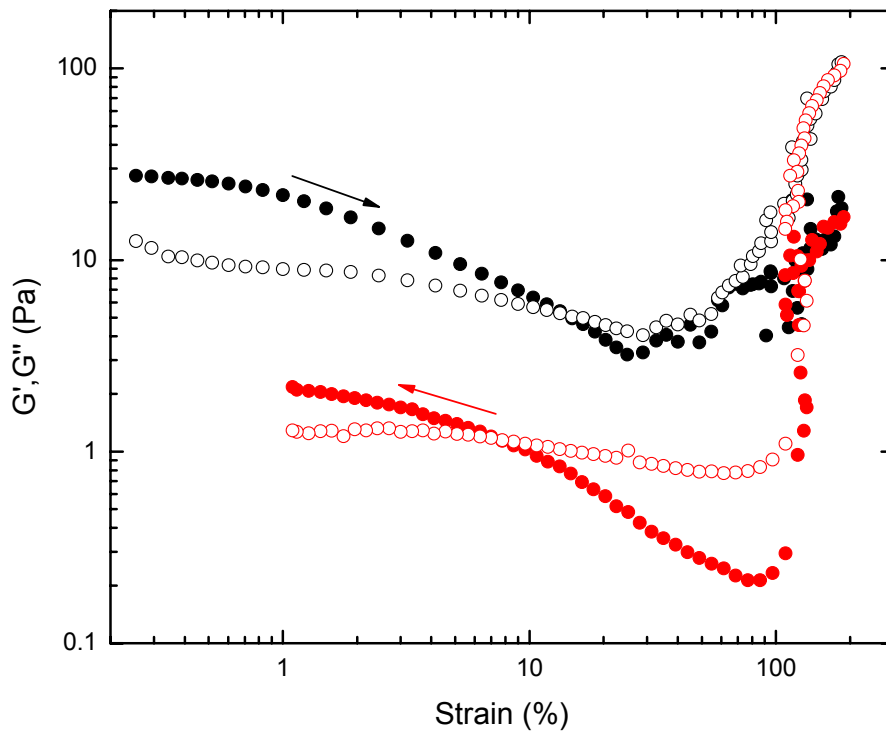


Figure 4.1.4: Dynamic stress sweep of larger spheres ($R=689\text{nm}$) at $\phi=0.63$ and $\omega=10$ rad/sec.

The ARES strain controlled rheometer was also used for some measurements either for the better Peltier temperature stabilization system or for DWS-echo measurements. There were some difficulties with these measurements, first of all being shear thickening. As the instrument is strain controlled, shear thickening can occur without much warning and ruin the sample measurement, or even pose a serious threat to the integrity of the sensitive transducer. With a stress controlled instrument, shear thickening can occur, but the amount of resistance of the sample can never be larger than the stress the instrument is applying, thus shear thickening appears relatively smoothly with increasing stress/strain. In the case of controlled strain, a small change can create large differences in stress, possibly overwhelming the instrument. For example if a strain controlled rheometer was measuring the crystal in figure 4.1.4 and increased strain from 100% to 120% it measure a stress difference of 2 orders of magnitude.

Recent work of Cohen et al. (2006) shows that slip could be an important factor when observing shear induced crystallization under oscillatory shear. In order to check for slip, we used a cone-plate geometry coated with hard sphere particles, which has been seen to inhibit slip. In order to coat the cone and plate, a low volume fraction sample was prepared and by spinning the geometries at high speed a thin film of particles was deposited on the surface. The geometries were then shortly baked (10min) at temperatures slightly higher than the T_g of PMMA in order to partially melt the particles on the surface and make them resistant to detachment. After the geometry was coated we ran a DSS crystallizing loop and compared it to the same uncoated geometry. The results showed that there was no influence of slip on our measurements. We additionally made observations of the shear profile of our geometry with a CCD camera (figure 4.1.5) for various strains and revealed no evident slip. However the CCD camera experiments did reveal shear banding, confirming the observations of both Cohen et al. (2006) doing oscillatory shear and Derks et al. (2004) with steady shear.

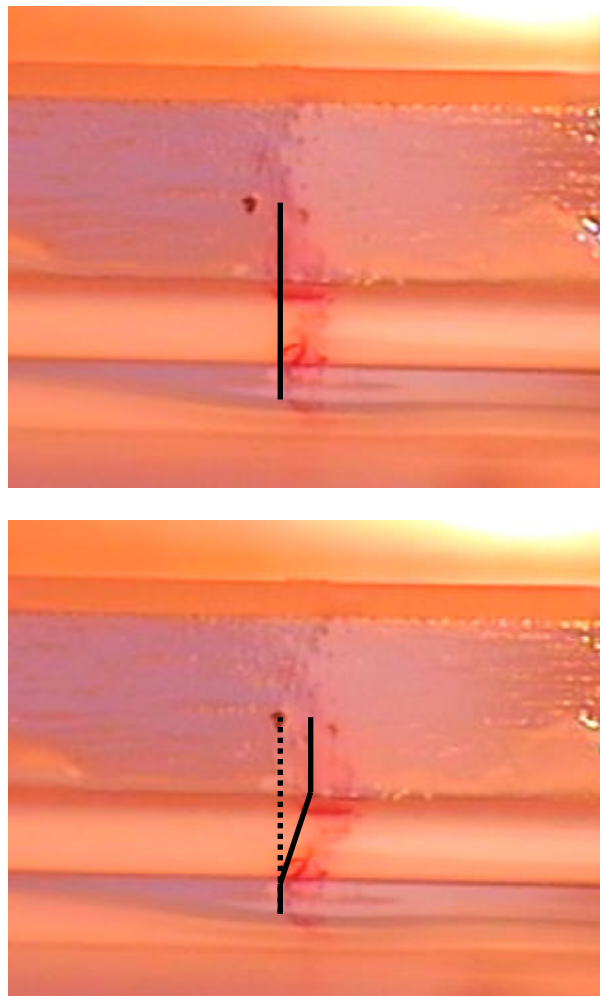


Figure 4.1.5: CCD photos of crystallization experiments (octadecene). The sample was painted with a marker to be able to visualize the shear profile and detect slip. The lines show the shear profile at two strain extremes of oscillation, revealing no slip (top moving plate).

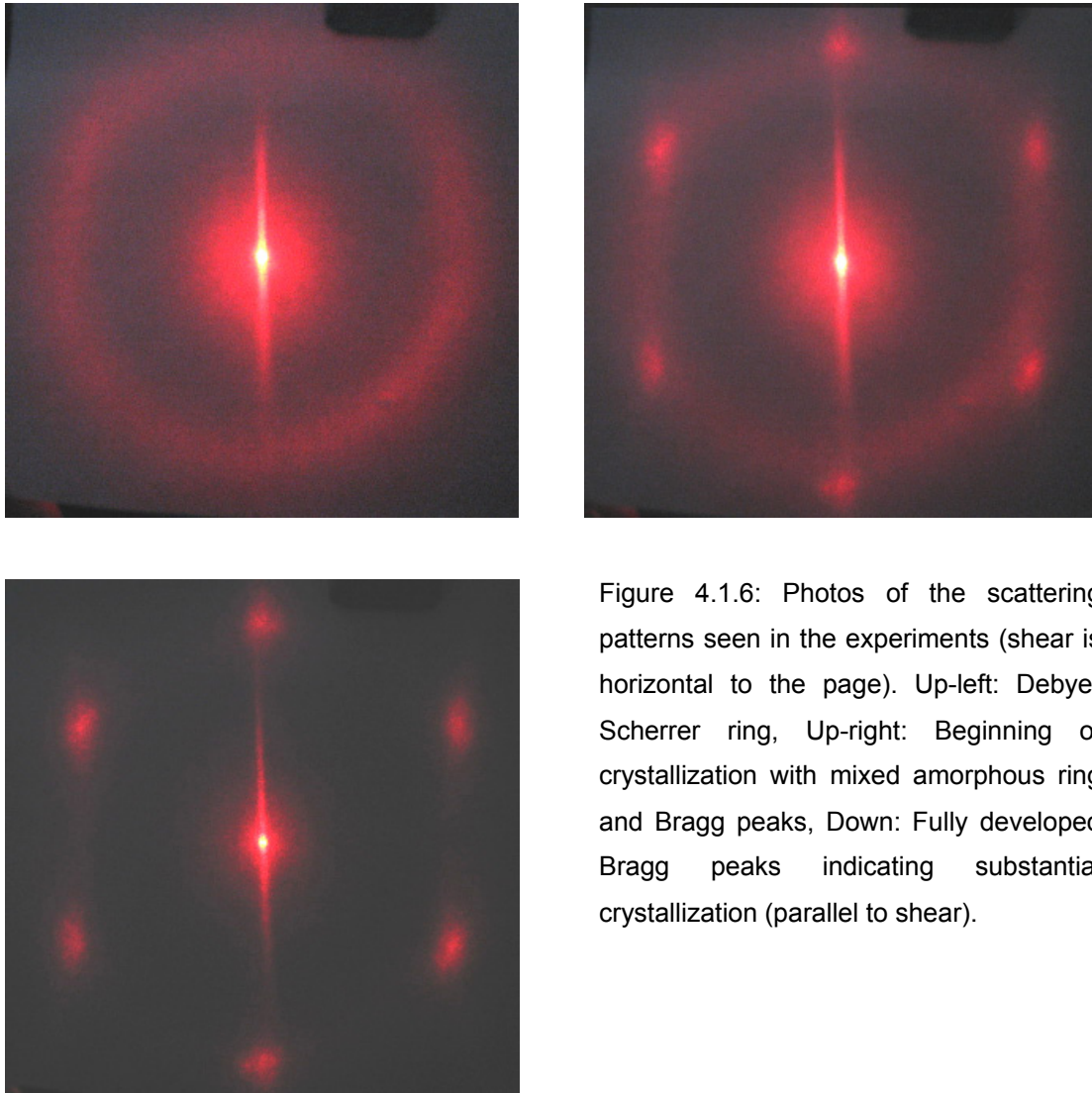


Figure 4.1.6: Photos of the scattering patterns seen in the experiments (shear is horizontal to the page). Up-left: Debye-Scherrer ring, Up-right: Beginning of crystallization with mixed amorphous ring and Bragg peaks, Down: Fully developed Bragg peaks indicating substantial crystallization (parallel to shear).

Only one type of crystal structure was distinguished during the experimental procedures; that of an FCC structure with close packed direction parallel to the direction of shear. Relating to a specific crystallographic direction, this FCC crystal was on the (111) plane and the direction of shear coincided with the $[\bar{1}10]$ (or $[1\bar{1}0]$) direction. The scattering pattern of this crystal, the amorphous structure and an intermediate stage of crystallization can be seen in the insets of figures 4.1.1 and 4.1.2a and more clearly in figure 4.1.6. As they are, it was impossible to take these photos during measurements, as the top glass tool would hide about half the image. These images were taken with a sample of larger spheres, after removing the plates from the rheometer.

As mentioned before in the work of Haw et al. (1998), low oscillatory strains (<50%) produced FCC crystallites with a preferred close packed direction perpendicular to shear, and high strains (>50%) produced a crystal structure with a close packed direction parallel to shear. This seems to contradict these experiments, but we verified this same behaviour with our

samples in a sliding parallel plate geometry (Petekidis et al. 2002) similar to theirs and have concluded that the rotating cone-plate geometry used here and well as the rotating plate-plate geometry somehow suppress the creation of crystals perpendicular to shear. Presumably, due to the rotational geometry, the crystallites are constrained in such a way that promotes growth only parallel to shear. It should be said that Derks et al. (2004) have also used a cone and plate geometry for studying hard sphere crystals. However they focus on steady shear and do not state whether they see any crystals perpendicular to shear when applying oscillatory strain. Ackerson and Pusey (1990) and Ackerson (1988) using a couette type rotating geometry also did not mention any crystallization perpendicular to shear.

Based on these experimental findings a tentative, hand waving argument can be put forward. Figure 4.1.7 shows a sketch of how constriction of the crystal perpendicular to shear can occur on rotating geometry. The lines represent the path of the close packed direction of the crystal and the spheres represent the size of individual crystallites. In the case of the crystal parallel to shear (left), it is easier to create a monocrystal throughout the geometry as the close packed lines follow the direction of shear and are always parallel to one another. In the case of a crystal perpendicular to shear (right), the crystal's close packed lines would collide with each other, creating inconsistencies and a polycrystalline material in the geometry. The red lines show the places where crystal cannot be created. Since the effect of the creation of the perpendicular crystal in sliding plates is not strong as there is a distribution of orientations, the constriction shown here could effectively create an energy barrier that does not allow any crystal other than parallel to shear to be created. All this of course is entirely speculative as at the moment there is no microstructural evidence to support it. A second possibility is that of normal forces, which may be different in rotational geometries and simple plate geometries affecting crystallization creation processes.

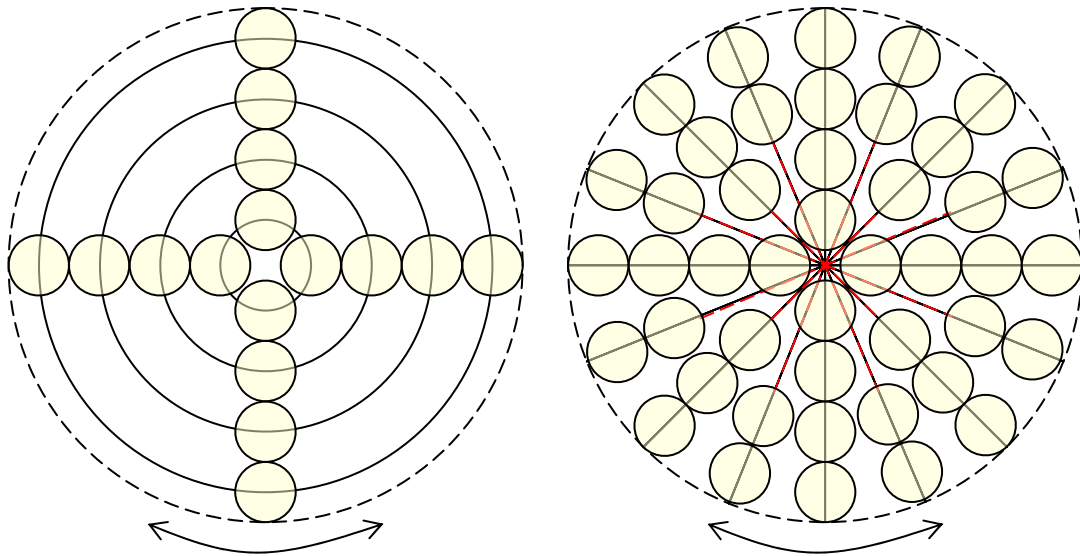


Figure 4.1.7: Representation of constriction of crystal perpendicular to shear on a rotating geometry. The solid lines represent the crystal's closed packed direction Left: Close packed direction parallel to shear and Right: Close packed direction perpendicular to shear.

On all the tested volume fractions and both sizes of spheres, the samples began to show crystallization at about 10%-20% strain, around the crossover point of G' and G'' . This is related to the yield strain of the hard sphere glass (Petekidis et al. 2002, 2003). Furthermore, testing proved that low strains could not fully crystallize the sample even after long shearing times (1 hour) and that higher strains were needed. Haw et al. (1998) saw that low strains (<50%) produced crystallites all throughout the sample after a finite amount of time, but the crystallites were oriented mostly perpendicular to shear. Only much higher strains (>>50%) were able to produce crystals parallel to shear. The inability of our samples to fully crystallize at low strains (>10%), even after a long amount of time, must be due to the rotational geometry, which apparently suppresses creation of crystals perpendicular to shear. At around 100% strain in our geometry, the glass would fully crystallize after a moderate amount of time.

Frequency dependence of crystallization

Besides depending on the level of strain, the speed of crystallization also depends on the size of the spheres. The crystal of the larger spheres could stabilize optically and rheologically considerably faster than the smaller one, due to the reduced contribution of Brownian motion to the kinetics of the particles. For the same reason DSS at low frequencies were unable to induce full crystallization (at an experimental time scale) and the frequency above which crystallization is experimentally viable for the smaller spheres is higher. More specifically the small spheres could not crystallize fully at a frequency of 1 rad/sec. Thus all DSS experiments were done on a frequency of 10 rad/sec in which both spheres could crystallize easily.

To quantify these observations we use the Peclet number, which is a measure of the relative importance of Brownian and shear induced motions and is given by the product of the shear strain rate $\dot{\gamma}$ and the Brownian relaxation time (τ_B). For a dilute system $\tau_B = R^2/2D$, where R is the particle radius and $D (= k_B T / 6\pi\eta R)$ is the Stokes-Einstein-Sutherland diffusivity of a non interacting particle in a medium of viscosity η . For shear rates much smaller than the Brownian relaxation rate ($1/\tau_B$), ($Pe \ll 1$) the intrinsic dynamics of the system relax much faster than the rate at which shear disturbs the structure and thus in our case crystallization is not expected. If the shear rate is sufficiently high, then $Pe \gg 1$ and the structure of the system is altered before it can relax back to equilibrium and thus we can expect changes on the structure of the system. When dealing with glassy hard spheres though, the Peclet number is not enough to show the point at which the structure changes. At small strains, the particle cages do not allow particle rearrangements in the system even at high Peclet numbers. Thus in order to induce crystallization in our systems, both the induced strain must be higher than a critical strain (equal or related to the yield strain) and also the Peclet number greater than unity.

On increase of strain or frequency there is also an increase in the maximum shear rate and subsequently the Peclet number, which indicates the reason why the rate of crystallization rises with increased strains and frequencies. We also see that the Peclet number is proportional to the cube of the particle radius, which in our case essentially means that larger particles need smaller rates to crystallize. Specifically for the sizes of our particles and for fixed values of strain and frequency we find that $Pe_{large}/Pe_{small} \sim 17$. If we approximate τ_B of the short time self diffusivity (before any collisions occur) in the glass regime to be 10 times larger than in the dilute regime (van Meegen et al. 1998), use $\omega = 10$ rad/sec and the yield strain of 10%, we get a Peclet number equal to 1.5 for the smaller spheres.

With an increase in volume fraction, τ_B is expected to rise and with it the Peclet number. This means that it should be easier to crystallize higher volume fraction glasses than lower ones. However, just by observing the crystallization time during the measurements there was no distinguishable difference of the speed of crystallization between examined volume fractions. Though we did observe that at volume fractions below the glass regime, the strain needed to fully crystallize the sample decreased. This seems to go against the Peclet number as τ_B should decrease with decreasing volume fraction, but as the glass cages become loose and cease to exist, the effect of yield strain should disappear, allowing crystallization at smaller strains.

Alternatively, shear induced crystallization can also be described from an energetic point of view. Throughout a glassy hard sphere system, there are high and low energy particle configurations. A system always prefers a lower energy configuration, but a glassy system is mechanically trapped and so remains at high energy configurations. If given enough time, the

particles cooperatively but slowly rearrange to lower energies, thus giving rise to aging. Even though the lowest energy configuration is a crystal structure, the system at rest is unable to get there. With increasing strain, the system is given enough energy so that the entropic barrier that keeps the particles trapped in their cages is slowly reduced and at some point disappears. At this point, the particles are allowed to rearrange themselves into their energetically preferred crystal structure. In the range where the barrier is reduced but not gone, the particles are given an increased possibility of escape from the cage, but not total freedom. Because the entropic barriers throughout the sample are of different height, low strains can only partially crystallize the sample. With increasing oscillation frequency, the particles are given more opportunities to escape, which means that the crystallization process will be more rapid. Rearrangement throughout the whole sample volume will only occur when the strain is high enough for all the barriers to disappear (Duff and Lacks 2007, Smith et al. 2007).

The created crystal could be dissolved either by applying an oscillatory shear with a high enough strain, or by applying a steady shear. Applying an oscillatory shear with high strain (>150%) led either to shear thickening or simply to the breaking of the crystal structure. Crystal breaking attributed to shear thickening was only observed for the larger particles. The smaller particles did not shear thicken easily except at high volume fractions and at very large strains (>250%) or frequencies as expected. A simpler way to break the crystal was to apply steady shear. Whenever there was need to go over from crystal to glass, a low rate steady shear was applied to avoid any possible complications that may stem from shear thickening and very large oscillatory strain (Maranzano and Wagner 2001).

4.2 Linear rheology - Frequency dependence

In order to probe the linear properties of the glass and its crystal counterpart we impose an oscillatory strain in the linear viscoelastic regime and probe different frequencies. This test is called a dynamic frequency sweep or for short DFS. The linear regime of the glass and crystal can be found from the DSS. In all cases we can see that this is less than 1%.

In figures 4.2.1 and 4.2.2 we show the linear viscoelastic data of the glass and shear induced crystal at different volume fractions. The dynamic frequency sweeps were performed in the linear regime with a strain of 0.5% for all the samples. As seen in these figures, the frequency dependence of crystal and glass are similar and as stated before, the values of G' , G'' for the crystal are significantly lower by about one order of magnitude. In these figures we include fits from the mode coupling theory of Mason and Weitz (1995).

In all volume fractions and both for glass and crystal, G' has a slight increase with frequency and in most cases G'' has a minimum. By examining the different volume fractions for glass and crystal, we see that the crystal exhibits a slightly larger slope of G' vs frequency. This means that due to increased contribution of Brownian motion for the crystal structure, the elasticity of the system drops faster with decreasing frequency of oscillation as elastic energy is more easily dissipated by Brownian fluctuations.

The fits used in the figures are derived by Mason and Weitz (1995) from the Mode Coupling Theory and follow these equations:

$$G'(\omega) = G_p + G_\sigma \left[\Gamma(1-a') \cos\left(\frac{\pi a'}{2}\right) (\omega t_\sigma)^{a'} - B\Gamma(1+b') \cos\left(\frac{\pi b'}{2}\right) (\omega t_\sigma)^{-b'} \right] + G'_D(\omega)$$

$$G''(\omega) = G_\sigma \left[\Gamma(1-a') \sin\left(\frac{\pi a'}{2}\right) (\omega t_\sigma)^{a'} + B\Gamma(1+b') \sin\left(\frac{\pi b'}{2}\right) (\omega t_\sigma)^{-b'} \right] + G''_D(\omega) + \eta'_\infty \omega$$

$$G'_D(\omega) = G''_D(\omega) = \frac{3}{5\pi} \frac{k_B T}{a^3} \phi^2 g(2a, \phi) [\omega \tau_D]^{1/2}$$

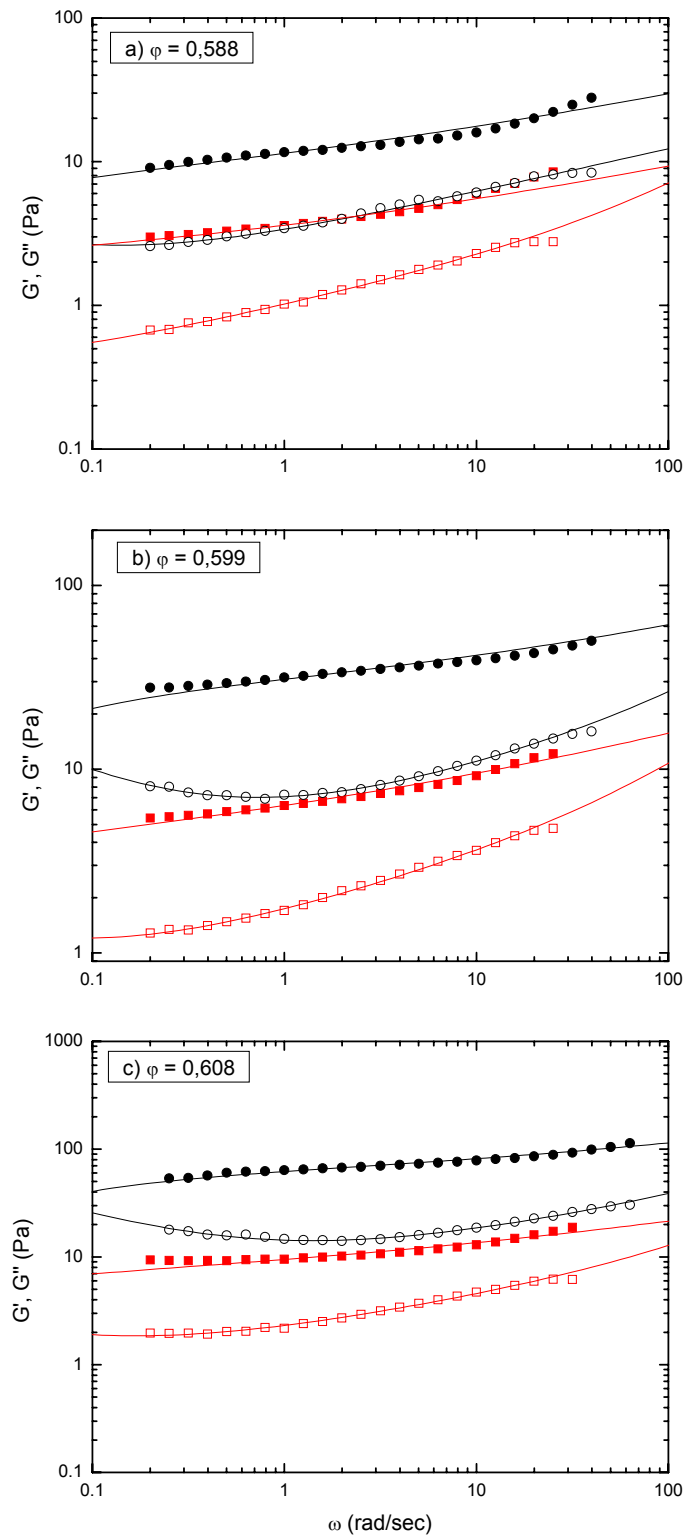
with $\tau_D = a^2 / D_s$ and $g(2a, \phi) = 0.78 / (0.64 - \phi)$, where τ_D is the diffusion time of the short time self diffusion coefficient and $g(2a, \phi)$ is the approximated radial pair distribution function at contact. $\Gamma(x)$ is the gamma function, $a'=0.301$, $B=0.963$ and $b'=0.545$ are parameters predicted for suspensions of hard spheres. η'_∞ is the high frequency viscosity contribution, G_σ is a fit parameter and the plateau value of the elastic modulus is given by G_p . The time t_σ corresponds to the inverse frequency where the minimum of G'' occurs. The $G'_D(\omega)$ and $G''_D(\omega)$ components of the theory were not added in the fits, but even in the worst case (high frequencies), the deviation was less than 1% and thus would make no difference.

This is a physical model that combines a description of the onset of the glass phase using mode-coupling formalism with the high frequency contribution of Brownian motion. The

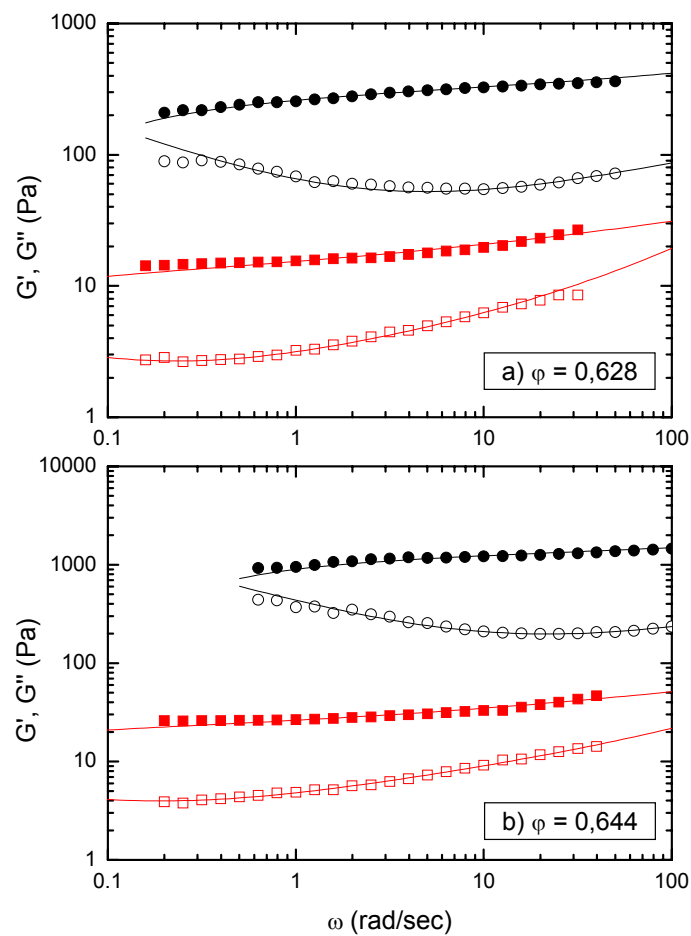
authors use the model on a system approaching glass transition and not on a system that is in a metastable glassy state. Nevertheless, the proposed model is able to capture the shape of our glassy system in addition to the shear induced crystal and will be used to extract the time scale t_0 that will be discussed further in the text.

Figure 4.2.3 shows time associated with the free fit parameter of the G'' minima versus the volume fraction. We believe that this time scale is coupled with the characteristic time that a particle needs to explore its neighbouring particles. Thus when one increases the volume fraction, the particle cages constrict and the characteristic time decreases. Similarly when probing the shear induced crystal, the interparticle distance becomes larger compared to the same volume fraction glass and the characteristic time is increased. This increase is larger as one goes up in volume fraction as the free volume distance for glass closes to zero faster than the free volume distance of crystal.

The mode coupling theory proposed by Mason and Weitz (1995) for the rheology of hard sphere suspensions and the theory which it is based on, proposed by van Meegen and Underwood (1994) for light scattering shows that the time scale corresponding to the minimum seen in G'' increases as the volume fraction nears the glass transition of $\phi = 0.58$, reaches a maximum and then decreases. In our measurements we see that as we increase concentration from liquid to glass, the time scale decreases steadily without any such maximum. Although the minimum is not apparent in the experimental data for lower volume fractions, by using the G'' minimum as a free fit parameter for the theory, we find an increasing time scale as the volume fraction decreases.



Figures 4.2.1: Dynamic frequency sweeps of lower glass volume fractions a) 0.588, b) 0.599, c) 0.608 in the linear regime for smaller spheres in cis-decalin. The solid points are values of G' and the hollow points of G'' . Note the lower G' and G'' for crystal (squares) compared to glass (circles). Added are fits to the data by the MCT theory of Mason and Weitz (1995).



Figures 4.2.2: Dynamic frequency sweeps of higher glass volume fractions a) 0.628 and b) 0.644 in the linear regime for smaller spheres in cis-decalin. The solid points are values of G' and the hollow points of G'' . Note the lower G' and G'' for crystal (squares) compared to glass (circles). Added are fits to the data by the MCT theory of Mason and Weitz (1995).

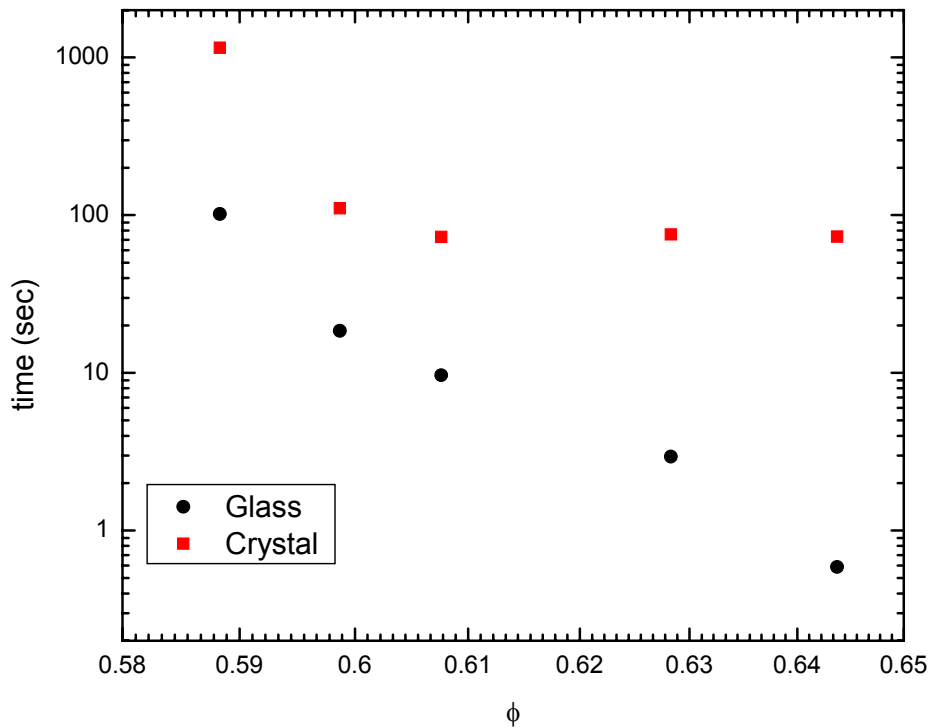


Figure 4.2.3: Values of time that correspond to the minimum of G'' (from fits to DFS) as a function of volume fraction.

In the next figure 4.2.4 we plot the same time as before but now against the inverse of the distance of the volume fraction from the maximum packing distance $1/\phi_{\text{free}}=1/(\phi_{\text{max}}-\phi)$, equivalently the inverse of the free available volume. For crystal the maximum FCC packing is $\phi_{\text{max}}=0.74$ and for glass the random close packing is $\phi_{\text{max}}=0.66$ (Schärfl and Sillescu 1994). The graph shows a clear correlation between the free volume and the time associated with the minimum of G'' . As the free volume decreases there is a steady decrease in the time it takes for a particle to explore its neighbourhood (line is a guide to the eye). Note that the error of determining the minimum increases at lower frequencies (large time) due to low rheometer torque (and lack of points). Because of this, values of time larger than about 20 sec (0.3 rad/sec) are uncertain at best.

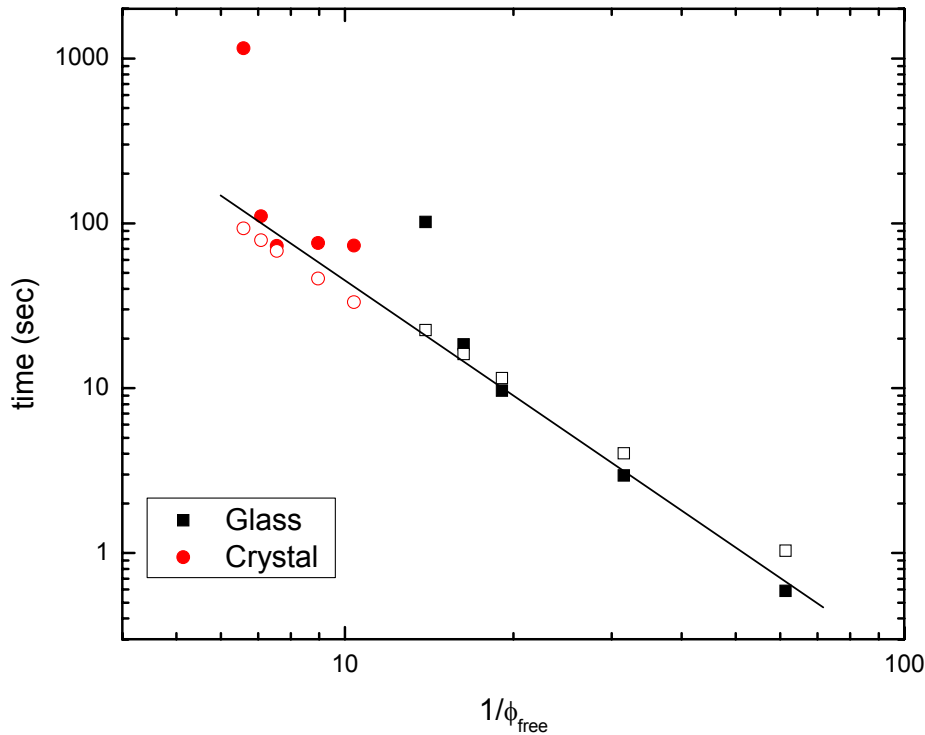
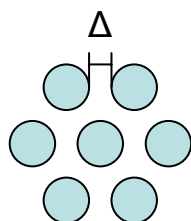


Figure 4.2.4: Values of time that correspond to the minimum of G'' from fits to DFS (solid) and results from simple calculations (open) as a function of the inverse of the distance from maximum packing. Maximum packing is 0.66 (RCP) for glass and 0.74 for FCC crystal.

We can make a rudimentary calculation of the time (t_b) needed for a particle to travel a distance Δ equal to the mean distance between particles as following:

$$t_b = C \frac{\Delta^2}{D_0}, \quad \Delta = 2R \left(\sqrt[3]{\frac{\phi_{\max}}{\phi}} - 1 \right)$$


with Δ the distance as shown in the above sketch for crystal maximum packing and C an arbitrary co-efficient used to fit the data. In figure 4.2.4 we can see that the general slope of the calculated points agrees with the experimental points, but the co-efficient is of the order of 10^4 which is discouraging.

A co-efficient of up to 100 could be explained by the effect of hydrodynamics on the diffusion co-efficient and also the idea that not just one, but many particles are moving, thus delaying the mean time needed to reach a neighbor. Cooperative effects have been observed by van Meegen (1998) that lead to a less tight cage. It is also logical to assume that the t_b we measure at the minimum of G'' is not the beginning of the relaxation process, but the very end, where everything has relaxed. Thus if we add the motion of the particles, the hydrodynamic effect of the self diffusion and the fact that we are looking at the end of the process we could explain the large co-efficient. Perhaps there are additional effects that we are unaware of which contribute to the co-efficient.

Previous theoretical work of Loose and Ackerson (1994) on the structure factor of FCC and HCP structures under shear shows that a crystal structure under shear has less frequent particle collisions than the same volume fraction glass. This may explain the significantly lower viscoelastic properties of crystal compared to glass, as particle collisions are directly proportional to elasticity. In addition, this can be also understood by looking at the mechanism from which crystal is created. Adding to the fact that the FCC crystal is the preferred energetic state, essentially the material assembles into the crystal structure as an effort to ease the imposed stress. This becomes obvious when looking at the fixed orientation and monocrystallinity (Amos et al. 2000) of the shear induced crystal, as opposed to the polycrystalline structure that hard spheres assemble to when left at rest. Recent studies (Solomon and Solomon 2006) have shown that the shear induced crystal made with high strains, similar to the crystal studied here, is not pure FCC, but has stacking faults, making it a mixture of FCC and HCP.

4.3 Linear rheology - Concentration dependence

Figure 4.3.1 shows the elastic and viscous moduli at the glass and crystal state of the three systems, smaller spheres in cis-decalin, smaller spheres in octadecene and larger spheres in cis-decalin. The smaller spheres were measured at 1 rad/sec and the larger spheres at 10 rad/sec. The values have been normalized with sphere size and thermal energy. In all three systems it is clear that the viscoelastic values of the crystal are always lower than that of glass and that the difference between them grows as the volume fraction increases. There seems to be a plateau value of the elasticity for the larger sphere crystal, but since the larger spheres have about 17 times less torque than the smaller spheres, these crystal values are subject to rheometer torque error (They are just out of rheometer torque). Since the viscous moduli generally follow the trend of the elastic moduli, only the elastic moduli will be discussed further in the text.

Figure 4.3.2 shows the elastic modulus of glass and shear induced crystal for the smaller sphere samples examined, plotted against volume fraction. These values were taken at a frequency of 1 rad/sec and G' has been again been normalized with sphere size and thermal energy. Figure 4.3.3 has the same values of the elastic modulus plotted against the inverse of the distance of the volume fraction from the maximum packing distance $1/\phi_{\text{free}}=1/(\phi_{\text{max}}-\phi)$, as done before. Added to this figure are values from theory and simulation.

The larger spheres were not added to the figure, as they needed to be in the same Peclet number in order to be comparable. This means that for smaller spheres at frequency 1 rad/sec, the larger spheres should be at a frequency of 1/17 rad/sec.

In figure 4.3.2, looking at the G' of the crystal and the glass for different volume fractions we can see that crystal generally has both a lower absolute value as discussed above and seems to have a weaker volume fraction dependence than the glass. Also, looking at the differences of the smaller spheres dispersed in the two different solvents, we can see that the spheres in cis-decalin strangely have higher moduli than the spheres in octadecene. In defence of this, we take into account the statistical error of about 1% in determining volume fractions with random close packing and add the fact that evaporation during loading is an important factor for the high volume fractions used in these experiments. However as stated earlier, there is some doubt if the particles in octadecene have truly hard interactions or if there are added interactions present. Because of the large refractive index mismatch, there might be a small attraction due to van der Waals forces.

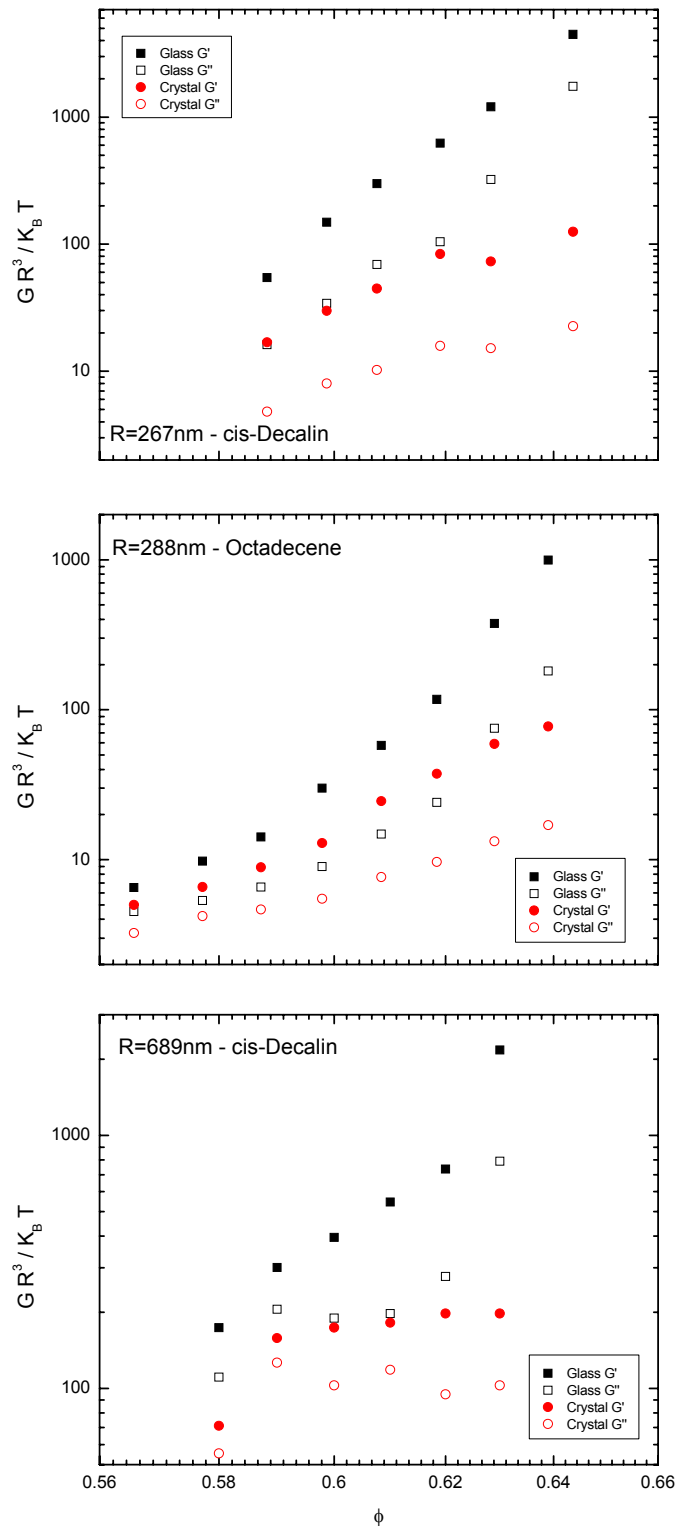


Figure 4.3.1: Elastic and viscous moduli at the glass and crystal state of the three systems used, normalized by thermal energy and sphere radius. The values of the smaller spheres were taken at a frequency of 1 rad/sec and the larger spheres at 10 rad/sec.

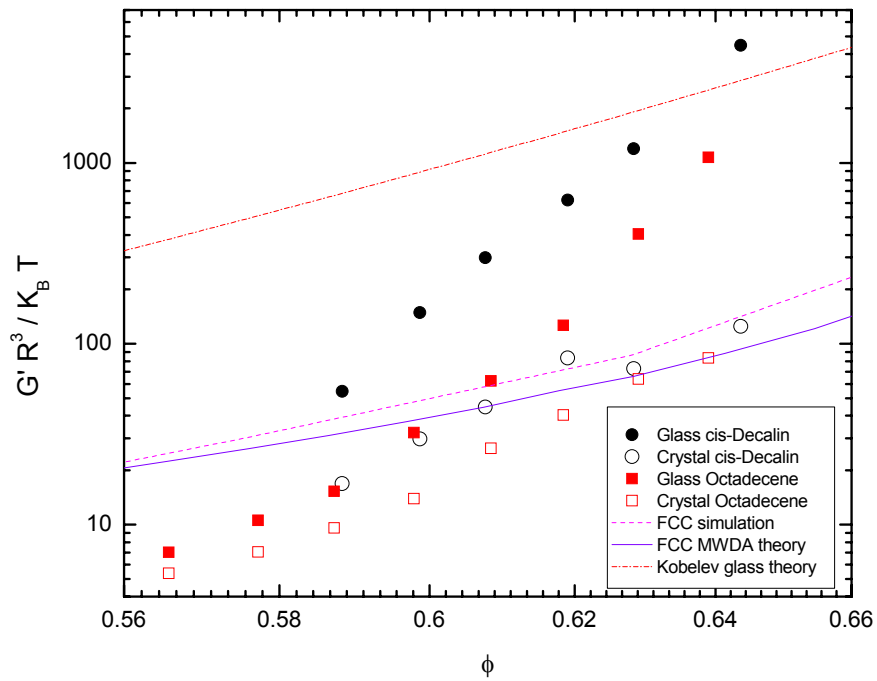


Figure 4.3.2: Graph of near-zero frequency ($\omega=1\text{rad/sec}$) normalized linear values of G' for glass and crystal plotted against volume fraction. Also included are lines from theory and simulation discussed further in the text.

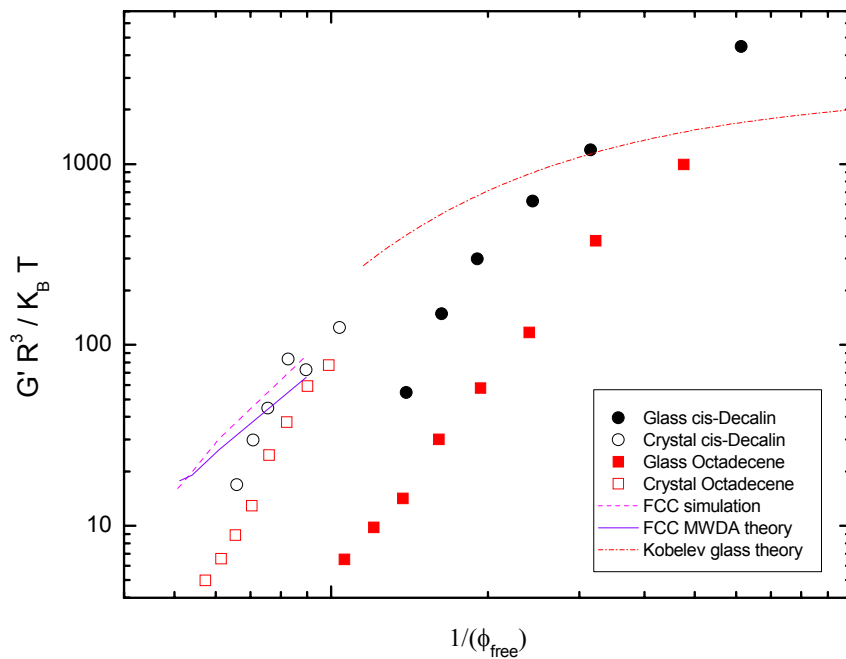


Figure 4.3.3: Graph of near-zero frequency ($\omega=1\text{rad/sec}$) normalized linear values of G' for glass and crystal plotted against the inverse of the distance from maximum packing. Maximum packing is 0.66 (RCP) for glass and 0.74 for FCC crystal. Also included are lines of simulation and theory discussed further in the text.

According to Poon and Pusey (1995), from a simple model Van der Waals attractions between two particles are given by the following formula:

$$U_A(r) = -\frac{A}{6} \left[\frac{2R^2}{r^2 - 4R^2} + \frac{2R^2}{r^2} + \log \left(1 - \frac{4R^2}{r^2} \right) \right]$$

$$\text{with } A = \frac{3}{4} k_B T \left(\frac{\sqrt{n_1} - \sqrt{n_3}}{\sqrt{n_1} + \sqrt{n_3}} \right)^2 + \frac{3h\nu_e}{16\sqrt{2}} \frac{(n_1^2 - n_3^2)^2}{(n_1^2 + n_3^2)^{3/2}}$$

where r is the centre to centre separation, A is the Hamaker constant, n_1 is the refractive index of the particle and n_3 of the solvent, h is Planck's constant and ν_e is the main electronic absorption frequency in the ultraviolet with $\nu_e \approx 3 \times 10^{15} \text{ s}^{-1}$. In this way the attraction for octadecene particles is calculated to be of the order of the less than half the thermal energy at a centre to centre distance equal to $2R$, whereas for cis-decalin it's 20 times less. Even though the attraction is small, it could account for the small drop in the viscoelastic properties at small frequencies (Pham et al. 2006) and maybe the difference in the crystallization strain noted earlier.

We compare the experimental findings of the shear induced crystal with the modified weight density approximation theory (MWDA) of Laird (1992) and molecular dynamics simulations of Pronk and Frenkel (2003). The MWDA theory of Laird specifies the Helmholtz free energy as a function of particle density and calculates the elastic constants through minimization of Helmholtz energy. Pronk and Frenkel molecular dynamics simulations use the application of strain and measure the stress response on a FCC (and HCP) lattice to get the elastic constants. Comparing the theory and the simulation with the experimental values, we can see that even though we don't have an exact match, we do have results of the same order of magnitude. Additionally, Phan et al. (1999) has some rheological measurements on a random crystal made at rest. They have generally lower values than our crystal measurements and show a power law increase with volume fraction. The measurements were not made with a rheometer, but by using a light scattering set-up combined with mechanical perturbations. In addition to this, the measurements were made at high frequencies and strains outside the linear regime, so in conclusion we are not able to compare them to our measurements.

In Figure 4.3.3 it is worth noticing that the elastic modulus of the crystal is higher than the glass for the same distance from maximum packing. This is a reasonable result, as an ordered structure should have a higher elastic modulus than an amorphous structure that has the same free volume.

A way of determining the interparticle potential of the particles is to perform a power law fit of $G' \sim \phi^m$ on the linear experimental values. Since the average distance between particles is related to the volume fraction and $G' \sim (1/r)(\partial^2 U / \partial r^2)$, with $G' \sim \phi^m$ there is a predicted potential

$U \sim r^{-n}$ for $m=1+n/3$ (Paulin et al. 1996). Our measurements (1 rad/sec) on glass for decalin yield an exponent of $m_{\text{dec}}=48$ and for octadecene an exponent of $m_{\text{oct}}=42$. The hard sphere system examined by Petekidis et al. (2004) yields a similar exponent of $m_{\text{hard}}=41$. Systems with softer interactions are known to exhibit smaller exponents. Star polymers examined by Ozon et al. (2006) have $m_{\text{stars}}=5.7$ and soft core-shell particles of Deike et al. (2001) have $m_{\text{core}}=4$. Also the nanoparticles of Rao et al. (2006) which approach hard interactions are at $m_{\text{nano}}=17$. The theoretical predictions on hard spheres by activated hopping MCT of Kobelev and Schweizer (2005) which can be seen in figures 4.3.2 and 4.3.3, yield a relatively small exponent of $m_{\text{theo}}=15$ but generally have higher values than our measurements.

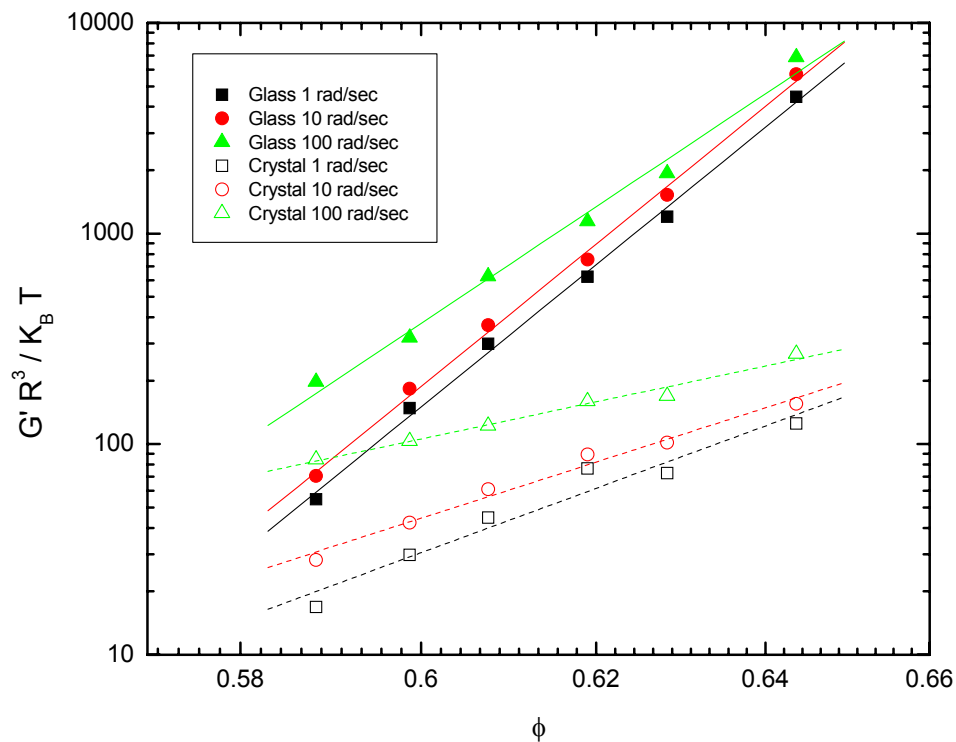


Figure 4.3.4: Normalized values of G' of glass and crystal versus volume fraction for smaller spheres in cis decalin at three different frequencies.

As previously mentioned, the slopes of G' vs ω for glass and crystal have a different dependence on volume fraction. This means that the slopes in Figures 4.3.1, 4.3.2 and 4.3.3 change according to the frequency at which the points were taken. The next figure (4.3.4) shows the frequency dependence of the slopes for the smaller spheres in cis-decalin. Three frequencies are shown of 1, 10 and 100 rad/sec. For glass, the power law exponents are 48, 47, 38 and for crystal 21, 19, 12 with increasing frequency. That means that the slope of the crystal can be equalized to the slope of the glass if we increase the frequency from which we take the values of G' .

Having said that, in Figure 4.3.2 the slope of the glass in both solvents used is approximately twice the slope of the shear induced crystal and in Figure 4.3.3, the slope of the shear induced crystal is about twice the slope of the glass. If we attempt to change the frequencies at which we take the points in order to equalize the slopes, in the case of Figure 4.3.2, we have to extrapolate the G' values of glass at 200 rad/sec and keep crystal at 1 rad/sec and in the case of Figure 4.3.3, we can achieve equal slopes by extrapolating the crystal frequency of 200 rad/sec and leaving the glass at 1 rad/sec. The reversal of the slope change is understandable as the x-axis of the two figures is different, but the physical meaning behind the factor of 200 between the two slopes is still not clear.

As said before, the larger spheres need to be in the same Peclet number with the smaller spheres in order to be comparable and by this the smaller spheres should be measured at a frequency 17 times more than the larger ones. Figure 4.3.5 shows such a comparison, with the large spheres being at a frequency of 10 rad/sec (the bulk of data is at that frequency) and the smaller spheres extrapolated from the frequency sweeps to the value of 170 rad/sec. If points for the two sizes are taken at the same frequencies the absolute values and slopes are very different, but on this graph we can see that the values are comparable and have a similar slope showing that these analysis are very sensitive to frequency.

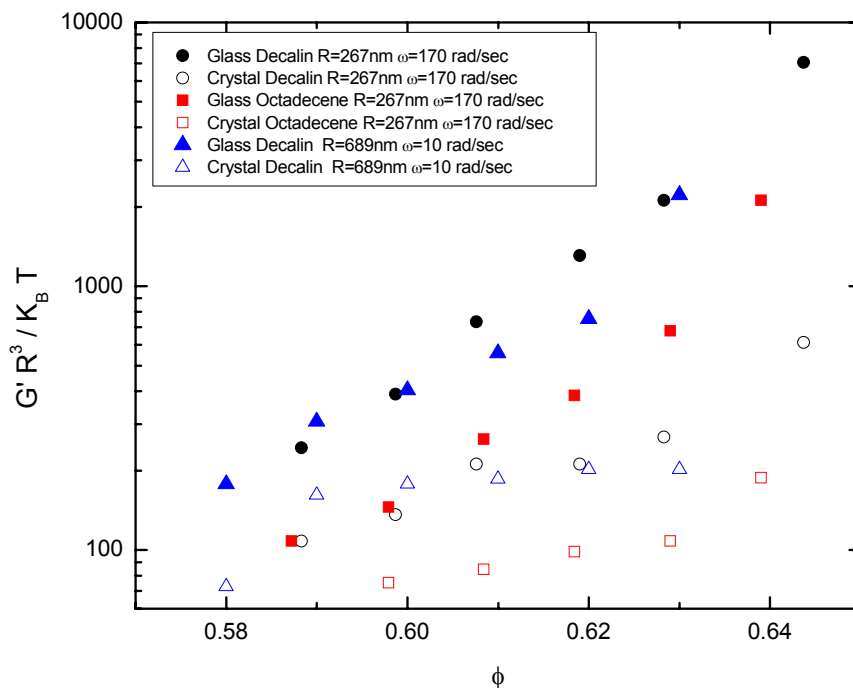


Figure 4.3.5: Graph of linear values of normalized G' for glass and crystal in the two different sphere sizes plotted against volume fraction. The small spheres are plotted at $\omega=170$ rad/sec and the larger ones at $\omega=10$ rad/sec to compensate for frequency differences and be at the same Pe.

4.4 Yield Stress and Strain

In Figure 4.4.1 and Figure 4.4.2 we can see the volume fraction dependence of the critical strain (maximum of G'') and crossover strain taken from the DSS of the small spheres in cis-decalin at a frequency of 10 rad/sec. The critical strain is the point where the system manifests a maximum viscous response (G'') at the expense of elasticity and the crossover strain, where G'' becomes equal to G' , is the point above which viscous behaviour dominates and strong irreversible rearrangements begin to occur.

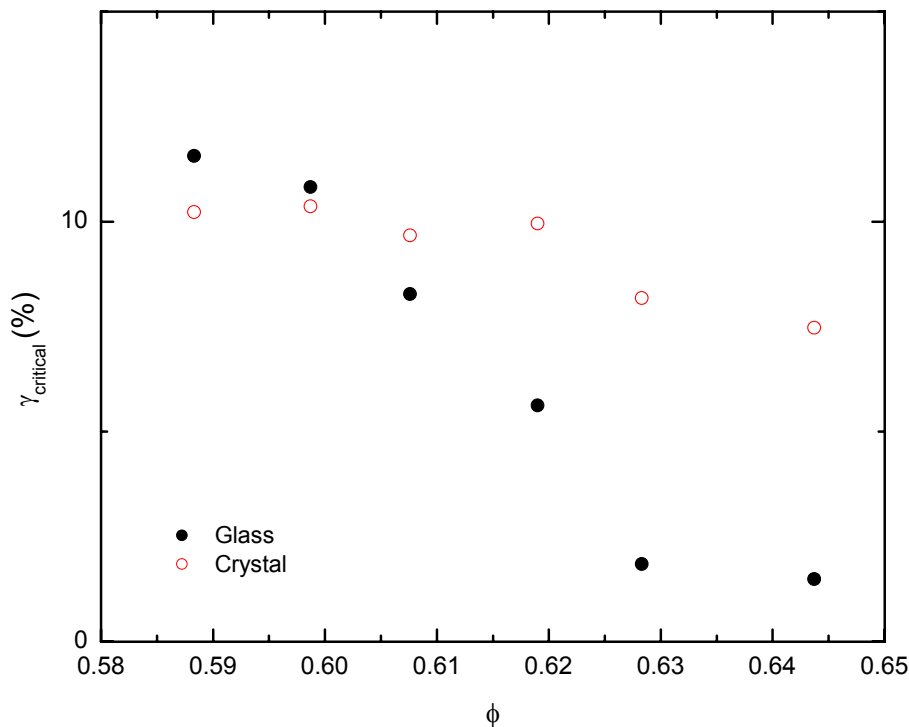


Figure 4.4.1: Critical strains as a function of volume fraction for glass (filled) and crystal (hollow). The points were taken from DSS at $\omega=10$ rad/sec as shown in figures 4.1.2 and 4.1.3.

In Figure 4.4.1 we can see the critical strain for both glass and crystal drop with increasing volume fraction. We believe this is because of the decreasing distance between neighbouring particles that makes it easier for fluidisation to begin. Particles will start hitting each other at lower strains as the cage becomes tighter, resulting in dissipation of energy that leads to an increase of G'' . The critical strain for crystal does not drop as fast as glass because of the larger distance from crystal maximum packing (0.74) as opposed to the glass random close packing (0.66) and the subsequent increase in the space available to each particle.

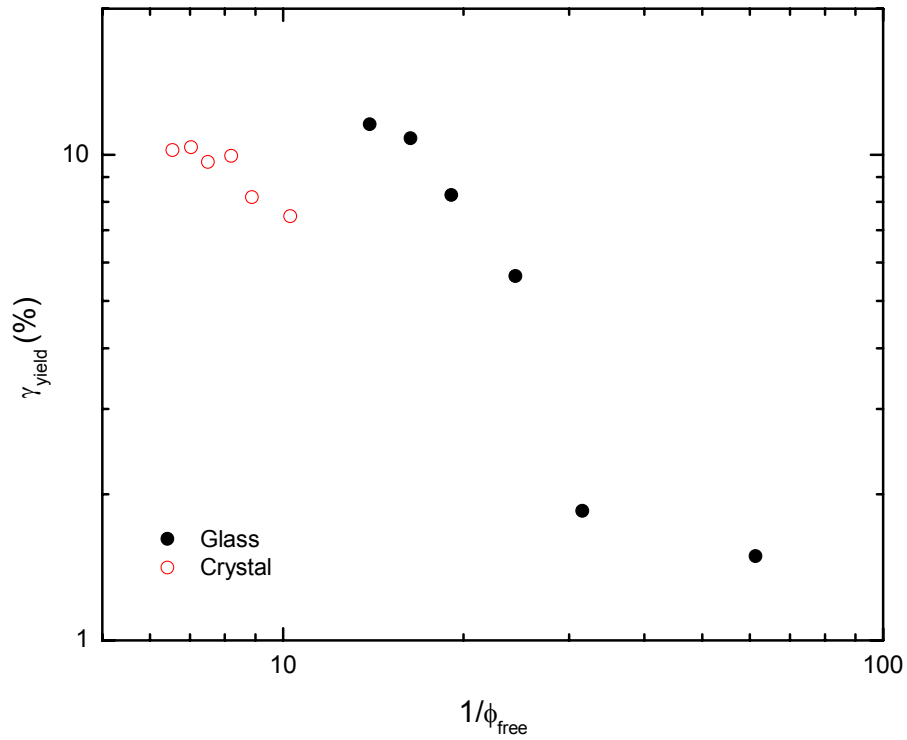


Figure 4.4.2: Critical strains as a function of the reciprocal of the free volume for glass (filled) and crystal (hollow).

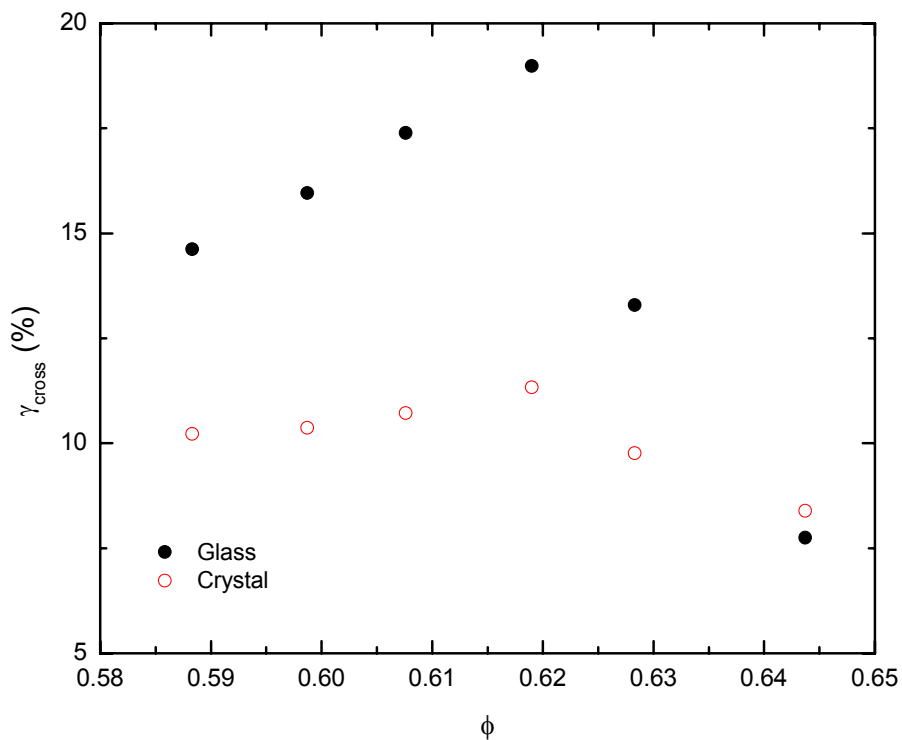


Figure 4.4.3: Crossover strains as a function of volume fraction for glass (filled) and crystal (hollow). The points were taken from DSS at $\omega=10\text{rad/sec}$ as shown in figures 4.1.2 and 4.1.3.

This is more clearly shown in the next figure (4.4.2), where we plot the same points with $1/\Phi_{\text{free}}$. We see that the fluidization strain for the crystal remains high as it has a large distance from maximum packing, but the glass responds with a sharp drop as it comes close to its maximum packing.

In Figure 4.4.3, we can see the crossover strain, again for both glass and crystal. Glass seems to generally have a higher crossover strain than crystal and there seems to be a clear peak in the crossover behaviour for glass. For a glass the crossover strain shows irreversible rearrangements and the 'breaking' of the hard sphere cages. For a crystal, the crossover strain again shows irreversible rearrangements and the point where the crystal flows because of crystal layers slipping one over the other (Ackerson 1990). The reason that the crystal has generally a lower crossover strain than the glass is probably because the slipping layers make it easier for a crystal to actually start flowing.

The results on glass shown in Figure 4.4.3 are very similar to those presented by Petekidis et al. (2002, 2003, 2004) on irreversible rearrangements of a non-crystallizing polydisperse system of hard spheres measured by DLS Echo and creep and recovery experiments. We believe that the maximum in the crossover strain is the result of two competing processes. As one decreases the glass volume fraction the particles loosen their cages and the yield strain starts decreasing until the system becomes a liquid and no yield strain exists. As one keeps on increasing to higher volume fractions, stricter glass cages are formed making the material more brittle and decreasing the crossover strain. Kobelev and Schweizer (2005) have made theoretical predictions for yield strain on glassy systems that qualitatively agree with our experimental data. The crossover strain for the shear induced crystal isn't affected by volume fraction changes as much as glass, again due to the increased free volume available for each particle and the larger distance from maximum packing.

The frequency dependence of the crossover strain in polydisperse glass (Petekidis et al. 2003) shows a weak increase with frequency and a qualitative agreement with our measurements. It seems that measurements of the crossover strain on monodisperse crystallizing glass are lower than the polydisperse glass, probably due to the added yielding mechanism of crystallization.

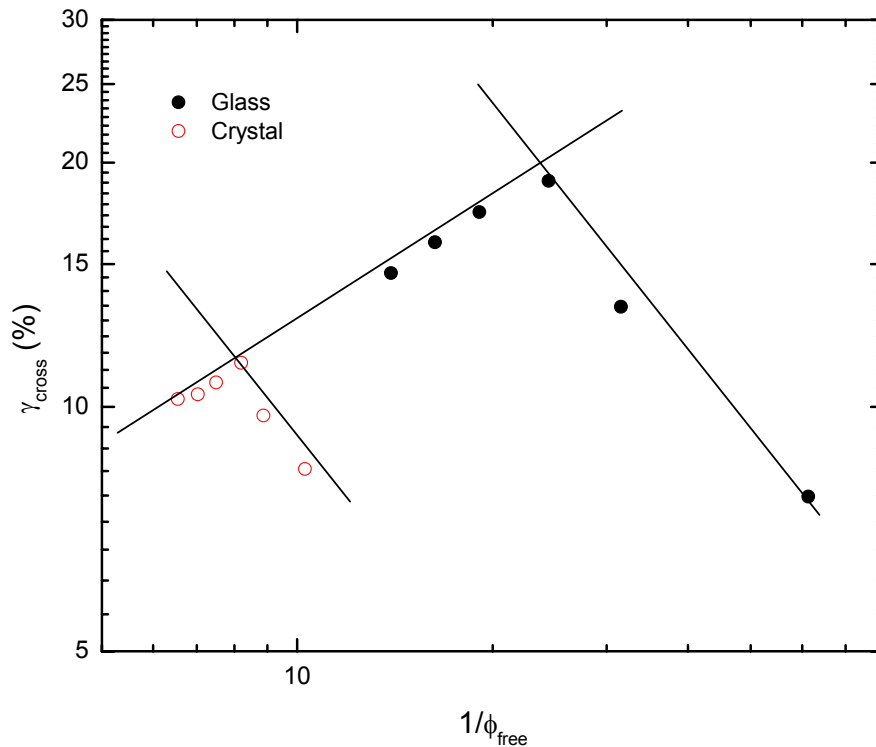


Figure 4.4.4: a) Crossover strains as a function of the reciprocal of the free volume for glass (filled) and crystal (hollow). The lines have slopes of 0.5 and -1.

In figure (4.4.4) we plot the same crossover points as before, but now with $1/\Phi_{free}$. Something interesting to note is that between glass and crystal, the two lines that follow the two competing processes discussed earlier have the same slope. For the first process, as the volume fraction is increased from the liquid regime and cages are formed, the slope is 0.5. For the second process, as the cages become tighter and the system becomes brittle, the slope is -1.

If Δ is solved for $(1/\Phi_{free})$ then we get the following expression:

$$\Delta = 2R \left[\left(1 - \frac{1}{\phi_{max} (1/\phi_{free})} \right)^{\frac{1}{3}} - 1 \right] \Rightarrow \Delta \sim \frac{1}{(1/\phi_{free})}$$

We see that the interparticle distance Δ scales approximately with $(1/\Phi_{free})^{-1}$ and as such, could be the source of the -1 slope in the second process, but the source of the 0.5 slope in the first process remains an open question.

4.5 Lissajous Stress-Strain

Stress vs strain Lissajous plots are shown in figure (4.5.1). In the linear regime, if the stress response is purely elastic, the Lissajous plot should show a straight line whose slope determines the elastic modulus. If a response is purely viscous, then an ellipse should appear, with axes of symmetry x and y . In the case of a viscoelastic behaviour, the shape should be a composition of the two, showing some sort of ellipsoid. If the sample gives non-linear responses, the Lissajous plots can give details on stresses in the period and may elucidate the mechanisms involved (Lee and Wagner 2003). These measurements were made in the strain controlled ARES instrument during the DWS-Echo experiments discussed in the following chapter. The curves are in arbitrary torque and motor angle units that have a linear relation to stress and strain respectively.

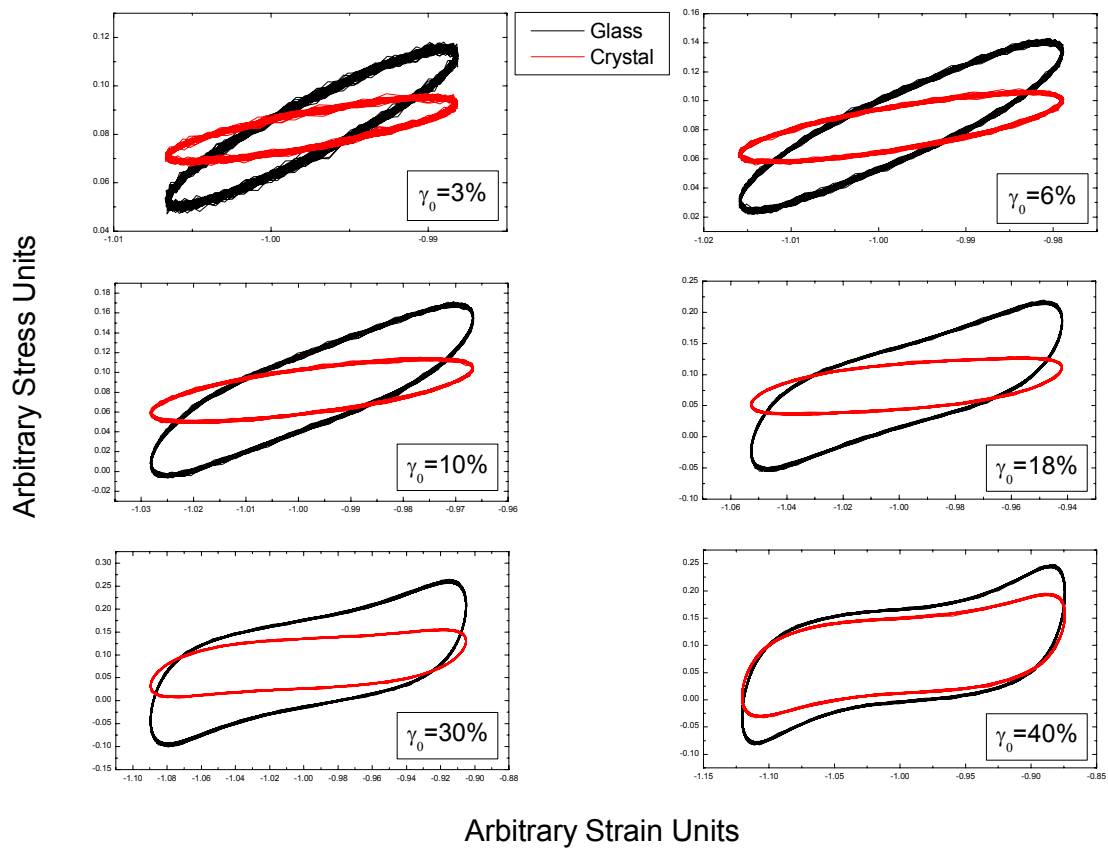


Figure 4.5.1: Lissajous plots of various strains of glass (black) and crystal (red) in arbitrary strain and stress units.

With a first look the Lissajous plots show that the non-linearities associated with high strain come sooner for the glass ($\geq 18\%$) than for the crystal ($\geq 30\%$). This can also be seen in the DSS curves and critical strains, where the linear region for crystal is larger than that of glass. The non-linearities we see in figure 4.5.1 come into play as stress increases at the extremes of oscillation. Microscopically this means that at low strains particle cages are only slightly distorted and the stress remains proportional to the applied strain, although slightly out of phase. As the strain is increased past the yield strain, the particles experience increased collisions causing a type of periodic thickening at the extremes of oscillation (Le Grand and Petekidis 2007). For the crystal this thickening is less pronounced than the glass (seen clearly at 40%) and starts presenting itself at higher strains. This can be explained again with the notion of slipping layers as they lower particle collisions and allow the crystal particles to avoid collisions at higher strains.

In addition, after analysis of the Lissajous plots with a Fourier transform, we found no even harmonics indicating the presence of a no slip condition (Wilhelm et al. 1998).

4.6 Aging

Rheological aging is examined in figures 4.6.1 and 4.6.2 by showing the time dependence of G' and G'' respectively in the linear regime for a glass and the shear induced crystal sample. Even though continuous measurements showed minimal effects, to avoid unnecessary stress to the sample and perhaps cause stress induced structural aging, each point was measured for a relatively short time at an interval of 30 minutes. In this part, the smaller particles dissolved in octadecene were used, in order to exclude evaporation effects during the long periods of measurement.

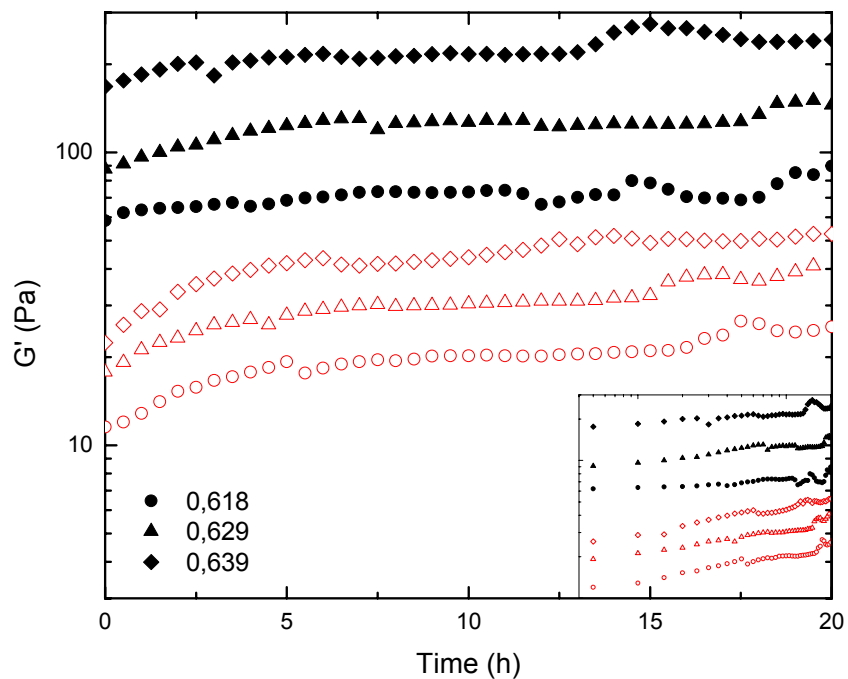


Figure 4.6.1: G' time dependence in glass and crystal states for three different volume fractions for the small spheres in octadecene: 0.639, 0.629, 0.618. The solid points are values taken from glass and the hollow points are values taken from crystal. The inset shows the same data plotted with a log-log scale.

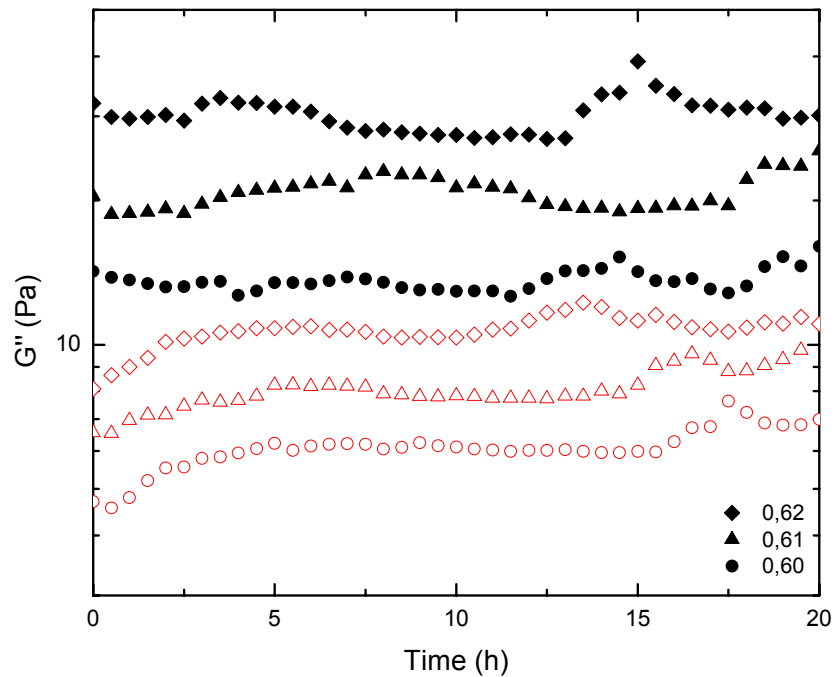


Figure 4.6.2: G'' time dependence in glass and crystal states for three different volume fractions for the small spheres in octadecene: 0.639, 0.629, 0.618. The solid points are values taken from glass and the hollow points are values taken from crystal.

When submitted to small linear perturbations, we could see that a glass sample, as expected, would exhibit rheological aging with increasing values of G' and G'' . Unfortunately G'' values are mostly erratic due to rheometer torque limitations. Furthermore when the shear induced crystal was left at rest for long periods of time (>10 hours), it seemed to keep its structural integrity and not dissolve. But when the crystal was rheologically probed, we witnessed a similar aging behaviour to that of glass. The inset of figure 4.6.2 shows a rough power law increase of G' for both crystal and glass, with the crystal having approximately twice the slope of glass.

The aging of crystal may look counterintuitive since a thermodynamically preferred crystal structure should not age. Glass structure is metastable and the particles don't have enough thermal energy to overcome the entropic barriers to the preferable crystal structure, which is the energetic minimum. By shearing the spheres, the entropic barriers drop and they are able to change to a more stable state in which they remain. Because of this stability, the hard sphere crystal might ideally be expected to show no aging compared to the same volume fraction glass.

Taking the above into account, we conclude that either perhaps the shear induced crystal created in these experiments was not fully made, maybe it started breaking and turned into glass or that after the end of shear the crystal continued to evolve. It is possible that due to

the rotational nature of the geometry, the hard sphere crystal would slowly realign itself after cessation of shear into a more preferable non-rotational structure, similarly to how hard spheres rearrange from random HCP crystallites to pure FCC at rest (Martelozzo et al. 2002). It is also possible that parts of the sample were inadequately sheared during the induced crystallization process and may have created glassy patches. These areas could only have been in optically non-accessible areas such as around the tip cut-off point in centre of the cone and near the edge of the geometry. Although this may seem as a plausible reason for the aging of the crystal, in reality there would have to be a substantial amount of glass throughout the bulk of the sample in order to have the aging results seen in figure 4.6.1. If the crystal structure dissolved into glass it would be seen in the absence of Bragg peaks. There is also a chance that the small change of interactions in octadecene could also change the properties of the crystal with time, although how this would come about is unknown. Some experiments were conducted on Couette geometry, but the results were qualitatively the same, strengthening the argument of crystal structure time dependence due to rotational geometry.

In order to experimentally solidify the argument that orientations other than parallel to shear have higher moduli, rheological observations of random crystallites were made. A sample of smaller spheres in cis-decalin was brought to a volume fraction of 0.57 and was observed. It was optically seen that random crystallites would form throughout the sample within 22 hours. The sample was then loaded into a Couette geometry and sealed with a solvent saturation trap. The sample was then measured for a small amount of time every 1 hour. After 22 hours had passed, the sample was sheared in order to create a crystal and then measured again. Figure 4.6.2 shows the results of this experiment. The sample evolves from an amorphous value of G' of 4Pa to 3Pa as the random crystallites are created. The shear induced crystal has an even lower G' which is 2Pa.

This indeed shows that shear induced crystal has smaller viscoelastic quantities (G' and G'') than a randomly oriented crystal. It proves that if shear induced crystal does reorient, the time dependent measurements will rise. Unfortunately it does not prove that reorientation is the cause of the rise we see. In summary, it seems that crystal ages, but there still remains an open question on the effect of the rotational geometry on the aging of crystal and on the exact restructuring which happens.

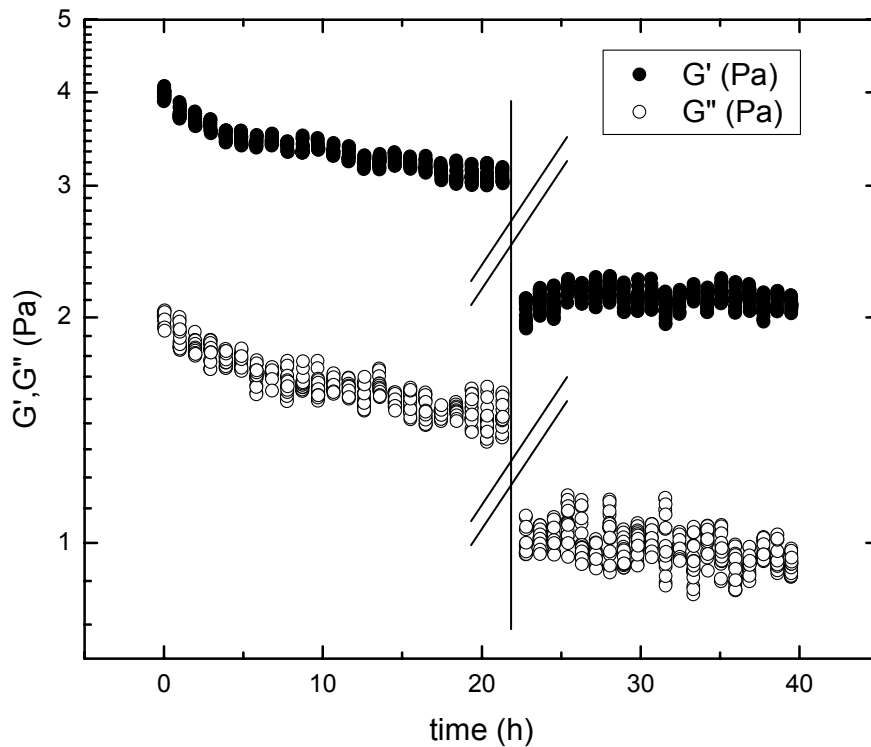


Figure 4.6.2: Before the break the evolution of rheological properties during crystal formation at $\phi=0.57$ is shown. During the break, crystallization was induced by shear and after the break we have the evolution of the shear induced crystal.

In addition to this, we also saw a correlation between small changes in measured temperature (± 0.1 °C) and the aging process. There were a series of rapid jumps in the time dependence of the viscoelastic properties of both glass and crystal. These jumps seemed to occur simultaneously with small but rapid changes in temperature. Both crystal and glass were subject to these anomalies.

According to (Mazoyer et al. 2006), the jumps in the viscoelastic properties could be the result of internal flows caused by temperature differences throughout the sample similarly to the effect on the characteristic internal relaxation. Internal flows could shear the sample and possibly cause over or under aging. In order to avoid these fluctuations, aging experiments were also carried out on a Peltier temperature stabilized system (± 0.01 °C) instead of the standard bath system. Results showed that the jumps were still present, although they were somewhat less in frequency and magnitude. This supports the idea that the temperature stabilization is not necessarily responsible for the erratic aging, but more that random external temperature fluctuations are the cause of internal shear.

5. Dynamic Light Scattering Echo

5.1 Introduction

To complement the rheological techniques and see what is happening on a microscopic level to the glass when it is sheared into crystal, we performed some Light Scattering Echo experiments. This technique, like classic light scattering, examines the degree of correlation of light between one moment in time to another. As this correlation in light is related with microscopic particle movement, it shows the correlation between particle positions. When a correlation function shows total de-correlation for a time τ , this means that the structure after time τ has changes compared to its initial structure over length scales which are determined by the scattering conditions. At rest this would mean that the system has rearranged itself in such a way that there is no correlation between the particles' positions after time τ .

When applying oscillatory shear, the sample de-correlates as the medium is distorted by flow and partially re-correlates at intervals multiple to the period of oscillation when the flow field has returned to its initial position. The amount of correlation which is recovered gives a measure of the amount of particles which returned to their initial position after one period of oscillation.

In normal dynamic light scattering (DLS) experiments the dynamics of the sample are examined through the measurement of the time autocorrelation function $g^{(2)}(\tau) \equiv \langle I(t)I(t+\tau) \rangle / \langle I(t) \rangle^2$ of the scattered intensity, $I(t)$ (Berne and Pecora 1976). In the case of transparent samples, the single scattering limit, the scattering at a particular wavevector are determined with $q = (4\pi n / \lambda) \sin(\theta / 2)$ as the wavevector, where λ is the wavelength, θ the scattering angle and n the refractive index. The length scale probed in this case is $2\pi/q$. On the other hand for opaque samples as in our case, the technique of Diffusing Wave Spectroscopy (DWS) is used in the limit of strong multiple scattering. In this case the dependence on the scattering wavevector is lost and the measured correlation and relaxation times depend on the scattering geometry (transmission or backscattering), as well as the number of scattering events N , the geometry of the incident beam and the intrinsic dynamics of the sample (Weitz and Pine 1993). The length scale probed by DWS is smaller than classic DLS and is of the order of λ / \sqrt{N} .

As mentioned, the autocorrelation function $g^{(2)}(\tau)$ decays with the application of oscillatory shear. If after one period of oscillation T (or mT), the scatterers return to their original positions, meaning a purely reversible deformation, the light speckle pattern reverts to its original configuration and $g^{(2)}(mT) - 1 = 1$. This is seen on the top scheme of figure 5.1.1 as an echo experiment that was performed on a sample of hard spheres near the random close

5. Dynamic Light Scattering Echo

packing where essentially no Brownian motion is present. The correlation function reveals 'echoes' of amplitude 1 at delay times equal to integer multiples m of the period of oscillation T . However, if the shear and/or the intrinsic motion induce some irreversible re-arrangements and the particles are not at their original positions, the echoes will have amplitudes that are smaller than 1. This can be seen in the bottom scheme of figure 5.1.1, where the Brownian motion causes the echoes to decay. We can decouple the shear induced from the Brownian re-arrangements by comparing the decay of the correlation function at rest to the echoes, again shown in the figure.

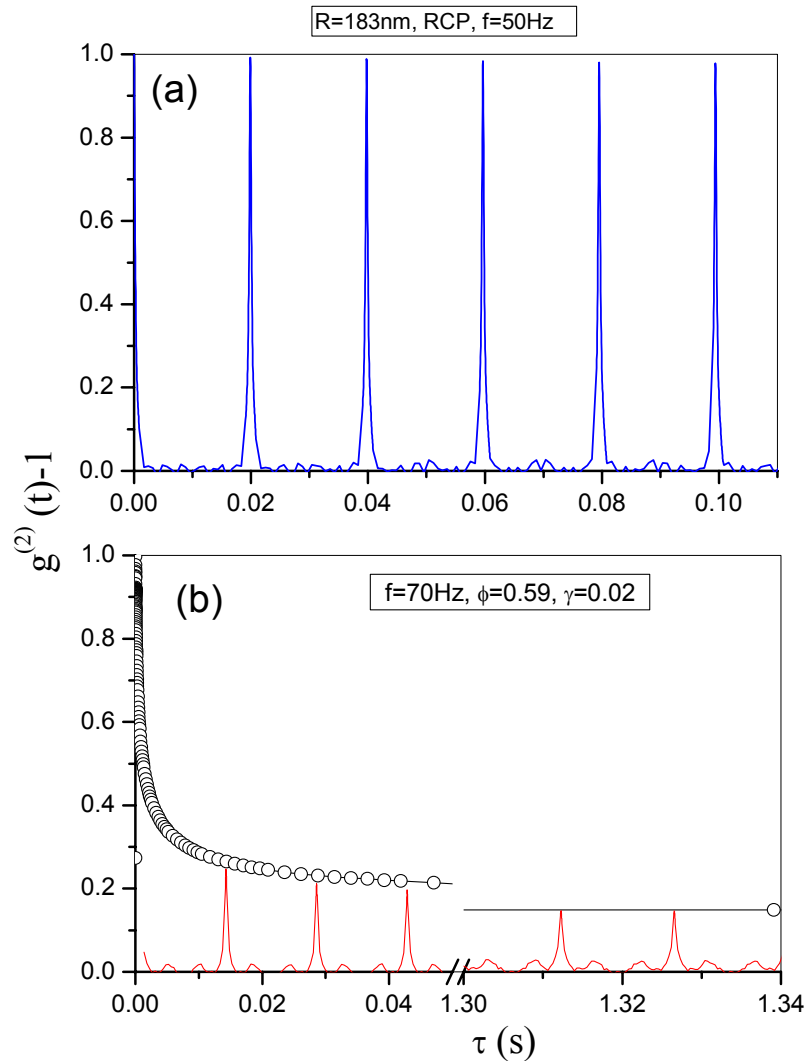


Figure 5.1.1: Echoes in the linear regime of random closed packed spheres (top) showing purely elastic response with no decay and a lower volume fraction (bottom) where we see decay due to Brownian motion (Petekidis et al. 2003).

In the simple case of a non-sheared dilute suspension of particles undergoing Brownian motion, in the strong multiple scattering limit, it is shown (Weitz and Pine 1993) that the correlation function approximately decays as an exponential according to:

$$\sqrt{g^{(2)}(\tau)-1} \approx \exp\left(-\frac{1}{6}Nk^2 \langle \Delta r^2(\tau) \rangle\right) \text{ (Eq. 5.1.2)}$$

where N is the average number of times a photon is scattered, $k = 2\pi n / \lambda$ is the propagation vector of light and $\langle \Delta r^2(\tau) \rangle$ is the particle's mean square displacement. Even though light scattering generally measures the collective motion of particles, it has been argued for large particles that DWS largely measures the self diffusion (Weitz and Pine 1993). Thus we will assume that the above equation applies to our experimental system.

If we apply oscillatory shear to the sample, we induce displacements additional to those due to Brownian motion, thus for the echo measurement we can write:

$$\sqrt{g^{(2)}(\tau)-1} \approx \exp\left(-\frac{1}{6}Nk^2 \left[\langle \Delta r^2(\tau) \rangle_B + \langle \Delta r^2(\tau) \rangle_S \right]\right), \tau = mT \text{ (Eq. 5.1.3)}$$

where $\langle \Delta r^2(\tau) \rangle_B$ is the displacement attributed to Brownian motion and $\langle \Delta r^2(\tau) \rangle_S$ the displacement associated with the additional shear induced diffusion.

Since the length scale probed by DWS is proportional to λ / \sqrt{N} , small motions will cause $g^{(2)}(\tau) - 1$ to decay to zero if the scattering events N are too many. For this we are forced to work with a small number of scattering events, where Eq. 5.1.2 may not be valid. Even though working between the limit of single scattering and strong multiple scattering is difficult, there has been work on double scattering (Sorensen et al. 1976). For the transmission geometry and our particular spheres, the dynamics are very similar to those measured by DWS at an approximated $N=2$. Thus by eliminating single scattering with a polarizer we can give a reasonable description of $g^{(2)}(\tau)$.

5.2 Experimental Setup

The echo experiments were carried out on the ARES strain controlled rheometer in the backscattering setup shown in figure 5.2.1, able to carry out rheological and scattering experiments simultaneously. A similar Plexiglas cone and glass plate were used as for the rheological experiments on the DSC stress controlled rheometer. The green laser ($\lambda=532\text{nm}$) shines from the top and the scattered light intensity is measured at backscattering. A photon multiplier tube is used for short times and echo measurements and an 8-bit monochrome CCD camera for longer times at rest. In order to cut off reflections and single scattering events, a crossed polarizer is put between the sample and the detector. Since the camera can image multiple light speckles through time, it is able to ensemble average as well as time average the intensity autocorrelation function.

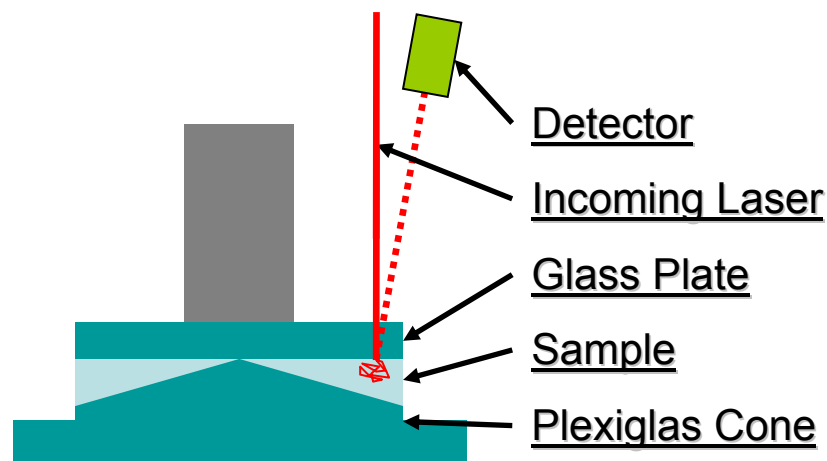


Figure 5.2.1: Representation of echo experimental setup.

5.3 Results - Discussion

Only the smaller spheres in octadecene were studied with the technique of light scattering echo. Before any measurements started, the glass was rejuvenated with a steady shear of small rate to break any crystal made by loading. Consecutive dynamic time sweeps at a frequency of 10 rad/sec (or 1.6 Hz) were made in order to measure the scattering response at different strains. Increasing strain amplitudes were examined as the crystal was being formed and then decreasing amplitudes after it was formed in order to probe the crystal structure. The crystallization strain of the sample was found by examining the rheological data and also by looking at the formation and disappearance of iridescence on the sample surface, which is indicative of crystallization.

The next figure (5.3.1) shows the correlation function taken with no strain applied, of a glass and a crystal, at a volume fraction of 0.602. The first part of the curves is taken with the photon multiplier tube and the second part with the CCD camera. The oscillations seen with the PM tube are possibly due to mechanical vibrations.

Something that is immediately clear by looking at the graph is that the crystal de-correlates more than the glass. This can be explained by the ability of the particles when arranged into a crystal to move larger distances in their cage than the glass particles at small times, because of increased free space for each individual particle. At longer times, as the crystal is spatially arrested in its lattice, it would be expected that the crystal correlation function would remain stable, whereas that one from a glass would de-correlate due to the slow modes. The glass aging related with these slow modes that may be related to dynamic heterogeneities, seen in several experiments (Weeks et al. 2000, 2002, Kegel and van Blaaderen 2000, Conrad et al. 2006). Due to instabilities of the scattering setup, longer times were not to be trusted and as such the experimental verification of this has not been possible at this time.

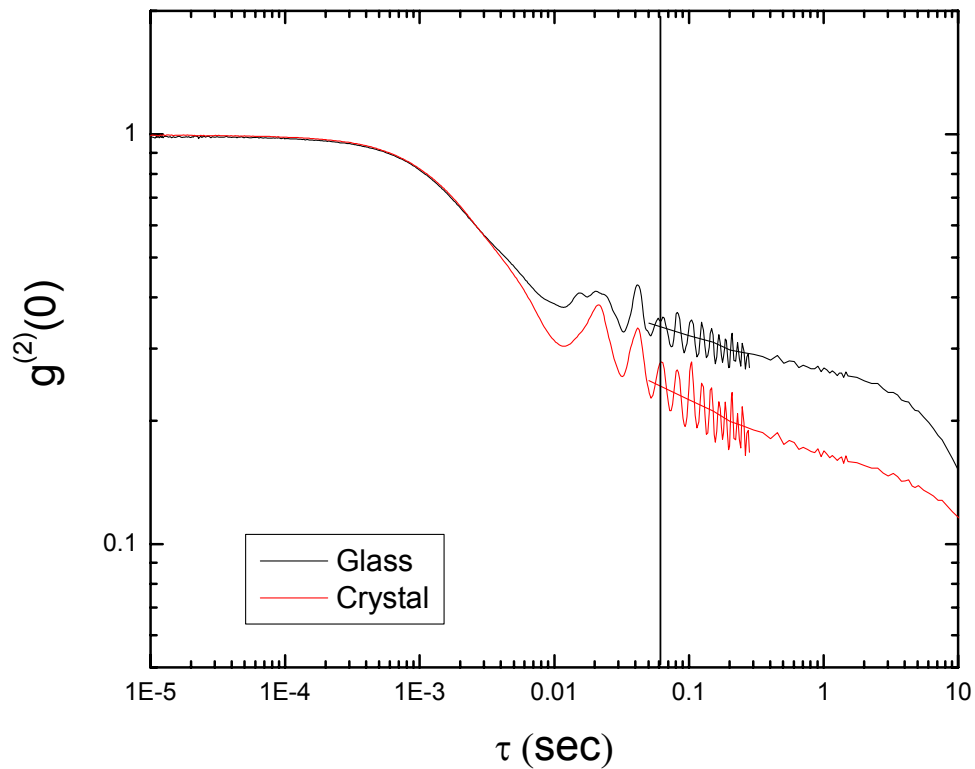


Figure 5.3.1: Normalised DWS response of smaller spheres in octadecene at $\phi=0.602$ comparing glass and shear induced crystal.

As the strain is increased (and consequently the strain rate), the correlation functions (figure 5.3.2) and the echoes (figure 5.3.3) decay increasingly faster. This is due to the faster shift in the particle positions by the shear deformation. The echoes become increasingly thinner because of the shear rate, but also reduce in height because of the occurrence of irreversible re-arrangements.

5. Dynamic Light Scattering Echo

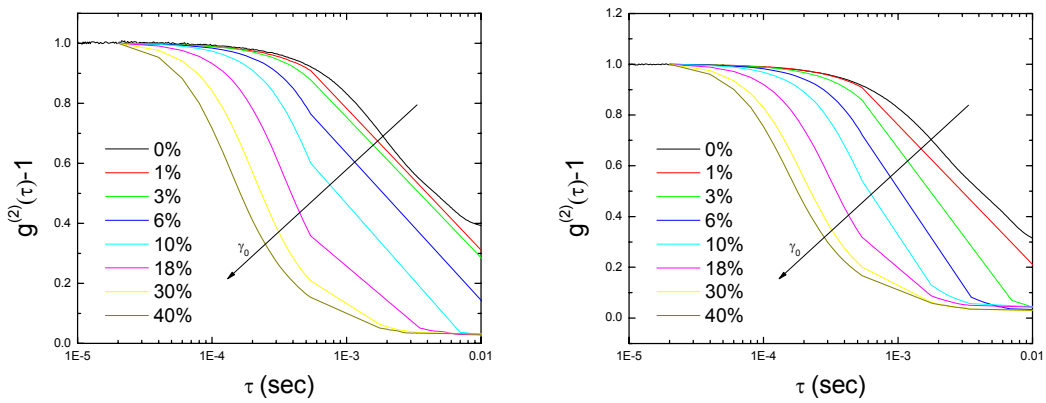


Figure 5.3.2: Normalized initial decay of correlation function with increasing strain (left) and decreasing strain (right).

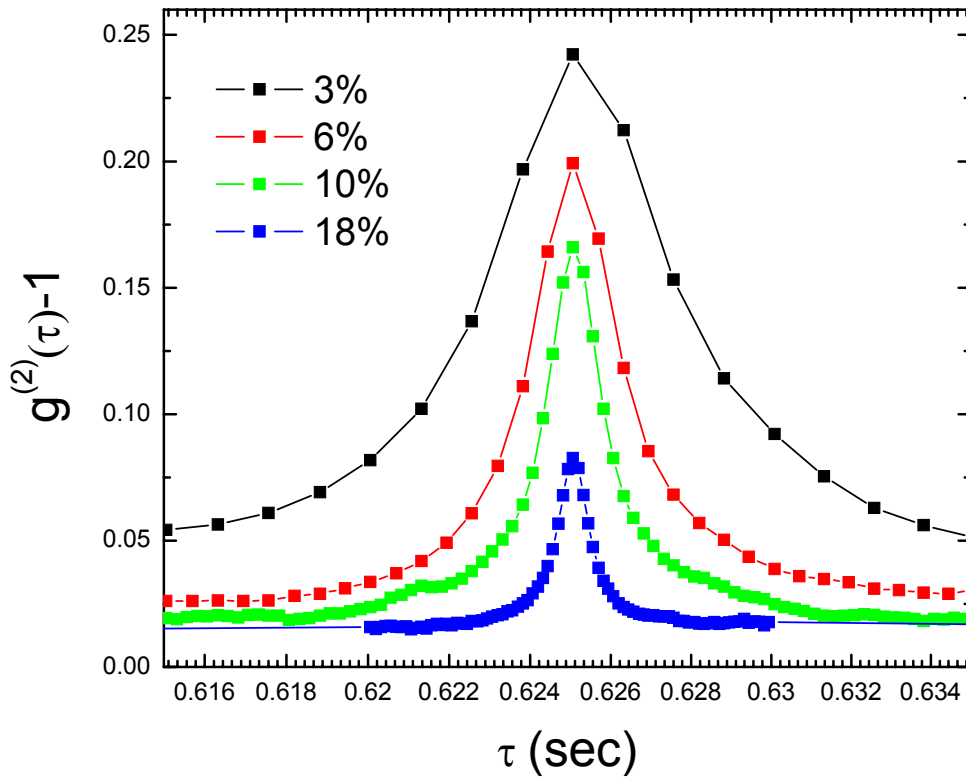


Figure 5.3.3: The first echo of the correlation functions for several strains at 1.6 Hz.

The reciprocal of the half width at half height taken from the first echoes can give us the decay rate Γ (Figure 5.3.4). We find that the decay rate increases linearly with the strain as also seen in the work of Petekidis et al. (2003). It seems that the decay rate is only a function of strain rate and does not depend on the structure of the measured sample. This is acceptable as a homogeneous strain field should cause a linear increase in the decay rate of

5. Dynamic Light Scattering Echo

the echoes, independently of the structure of the material (with small deviations) as long as there is no slip (Hébraud et al. 1997).

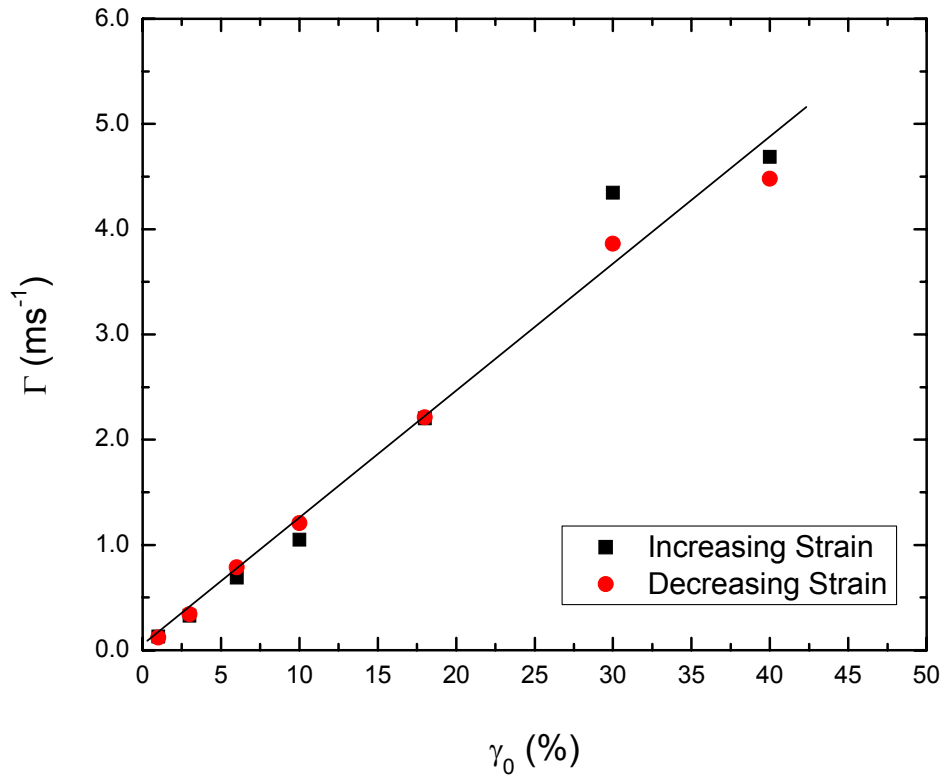


Figure 5.3.4: The decay rate Γ , taken from the half width at half height of the first echoes at different strains. The line shows the linear increase of Γ with γ_0 .

If we extract the height of the echoes at the multiples of the period at different strains we get figure 5.3.5. We can see that at low (linear) strains the echoes generally follow the correlation function at rest, but at higher strains, there are more rearrangements and thus the echoes become smaller. At longer times there are larger deviations as the statistics become poorer.

5. Dynamic Light Scattering Echo

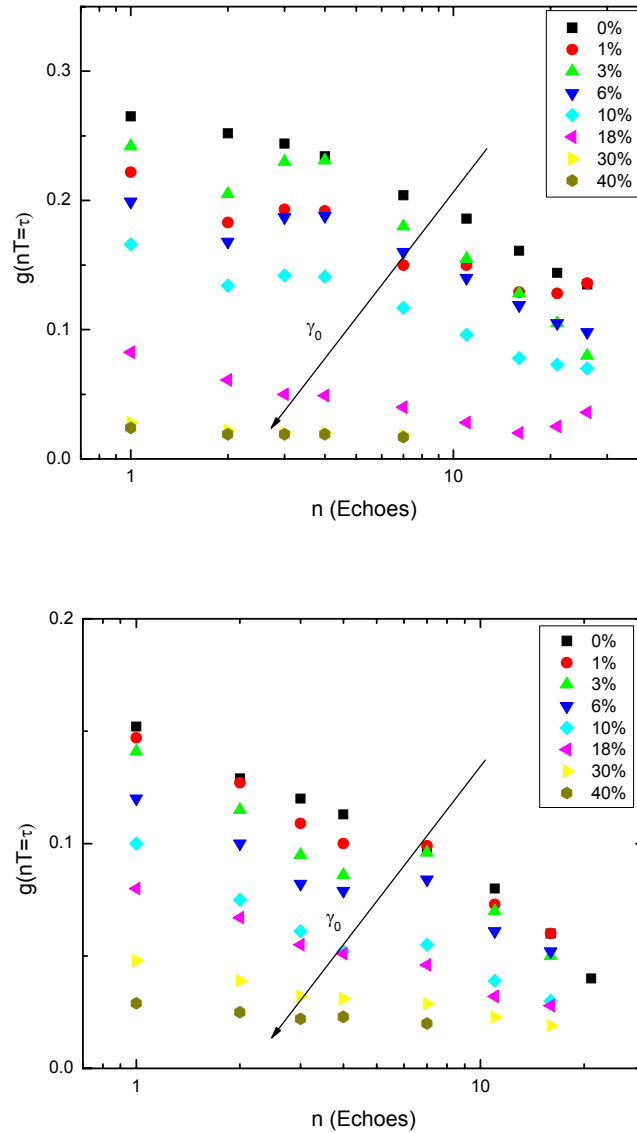


Figure 5.3.5: The normalized peaks of the echoes at multiples of the period nT at different strains. Both increasing (top) and decreasing (bottom) strains are shown.

By taking the heights of the first echoes at different strains we get figure 5.3.6. We start in the glassy regime and as the strain is increased, the echoes drop showing increasing irreversible re-arrangements. When the echo value reaches zero ($\gamma=40\%$), none of the particles return to their initial positions (within a length scale of $\lambda/2$) after one period of shear and the crystal is formed. As we decrease the strain, the amplitudes of the echoes of the shear induce crystal follow a different path leading to a smaller value than the glass at strain 1%. These small strains are linear and no shear induced diffusion is seen. The situation is identical as when the sample is at rest (linear regime), and the correlation function has decayed more due to the increased in cage diffusion of each particle in the case of the crystal structure. As the strain becomes non-linear the echo height from glass continues to be higher than the crystal, but at some strain becomes equal. This of course means that the shear induced diffusion of the

5. Dynamic Light Scattering Echo

glass at high strains is similar to that of crystal. The reason for this is not obvious, but the simulations which will be discussed in the next chapter, were able to give us some insight.

In the simulations we saw that, because of the crystal sliding layers, the shear induced displacements were large in the direction of shear, but very small in the other directions. For the glass structure on the other hand, particles were displaced similarly in all directions due to shear, although slightly more in the shear direction. Thus if the shear rate (or oscillatory strain at a given frequency) exceeds a certain value, the Brownian diffusion advantage the crystal had at small strains will be overshadowed by the increased shear diffusion of the glass at larger strains. If the simulations are correct, then for our experiments, at 30-40% strain the crystal Brownian diffusion advantage is diminished as the glass shear diffusion is increased when it is being reconfigured to a crystal.

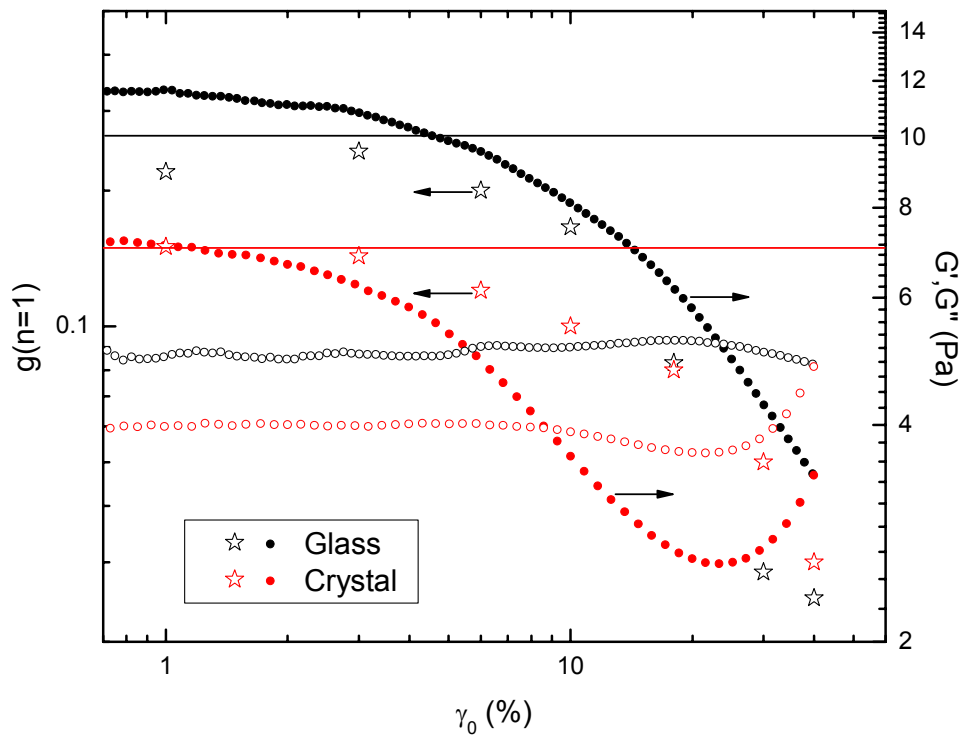


Figure 5.3.6: Height of first echo with strain for glass with increasing strain and shear induced crystal structure for decreasing strain. The horizontal lines show the height of the correlation at rest at the point of the echo for glass (black) and crystal (red). The overlapping graph is the increasing and decreasing DSS of the same sample. Note the higher echo heights of the crystal compared to the glass at high strains (30%-40%).

6. Brownian Dynamics Simulations

6.1 Introduction

In addition to rheology and light scattering echo, a number of Brownian dynamics simulations were conducted on hard sphere systems under oscillatory shear to complement the findings of the experimental techniques. The original code for these simulations was written by Andy Downard working in John Brady's group at the California Institute of Technology. The motivation to begin these simulations was to try and use the advantages of numerical computation to elucidate some issues on shear crystallization creation and destruction and to view the microscopic differences between glass and crystal structure. The code used here assumes Brownian diffusion of particles with hard sphere interactions. Hydrodynamic effects are ignored as the computational cost is high and the effect on structure at low Peclet numbers maybe negligible (Foss and Brady 2000, JFM).

A simple description of how the algorithm works is as follows: The algorithm positions a predetermined number of particles in a three dimensional box either randomly, or in preassigned positions. It then displaces them sequentially in a random Brownian step and applies a predetermined deformation. The Brownian step and the deformation, which is nothing more than a strain displacement in the velocity direction, change in magnitude according to the size of the predetermined time step. If any two particles' radiuses overlap after the end of these displacements, they are pulled back equally across the line that connects their centres so their distance becomes $2R$ and the force needed to push the particles away is calculated. This force corresponds to the calculated shear stress when the system is sheared. The algorithm then repeats the displacements and overlap checks, creating a repeating cycle. The positions of the particles are saved in predetermined intervals for further analysis.

In order to avoid wall effects in the simulated system, periodic boundary conditions are applied. When periodic boundary conditions are applied in a box, a particle can move freely to the edge and if it passes the edge boundary, it then appears on the opposite side of the box. Similarly, a particle on the edge of the box feels the particles on the opposite side of the box and interacts with them without knowing that they are actually ghost images. To the studied particles this should feel like an infinitely large system with an infinite amount of particles and as such, resembling a real system. Figure 6.1.1 shows a representation of the periodic boundary conditions. In the case of shear, the imaginary particles' shear velocity changes as compared to their real images as shown in figure 6.1.2 to keep the periodicity in order.

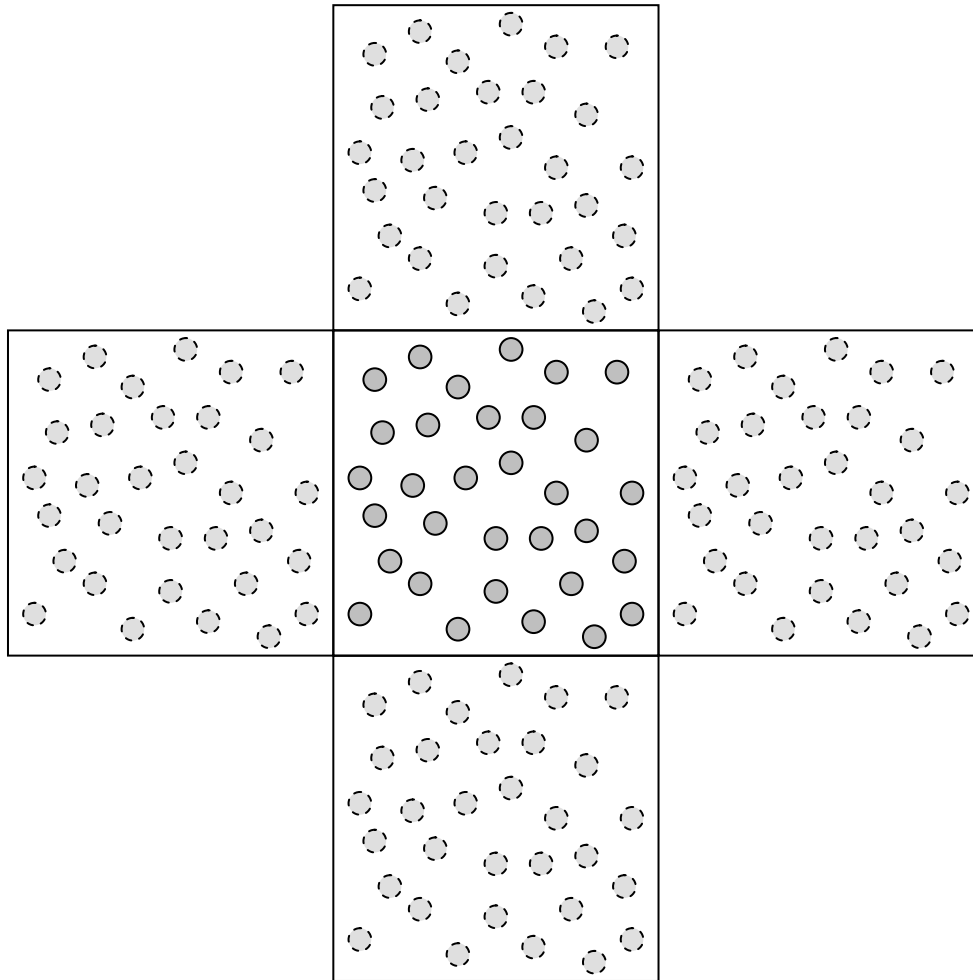


Figure 6.1.1: 2-D Representation of periodic boundary conditions. The surrounding boxes are copies of the centre box, the darker particles in the centre box are 'real' and the lighter ones on the outside boxes are 'imaginary'. The 'real' particles on the edge of the box can feel the 'imaginary' particles next to them and act accordingly.

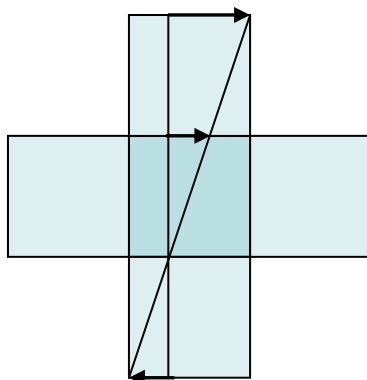


Figure 6.1.2: In the event of shear, the imaginary particles in the top and bottom boxes are sped up or slowed down as shown by the shear profile to keep the periodic boundary conditions in order.

6.2 Algorithm Details

Displacement equations

The details of the simulation algorithm are discussed nicely by Foss and Brady (2000, JOR), but a short description follows. Brownian dynamics can be described as a simplification of Stokesian dynamics, where hydrodynamic interactions between particles are neglected. For N rigid particles of radius R in a medium moving with velocity \mathbf{U} of viscosity η , where the Reynolds number is $Re \ll 1$ and Stokes number $St \ll 1$, the motion of the particles is described by the N -body Langevin equation:

$$\mathbf{m} \frac{d\mathbf{U}}{dt} = \mathbf{F}^H + \mathbf{F}^B + \mathbf{F}^P \quad (\text{Eq. 6.2.1})$$

where \mathbf{m} is the generalized mass/moment tensor, \mathbf{U} is the particle translational/rotational velocity vector, \mathbf{F}^H is the hydrodynamic force vector, \mathbf{F}^B is the stochastic force vector that gives rise to Brownian motion, and \mathbf{F}^P is the deterministic non-hydrodynamic force vector. For negligible hydrodynamic interactions the hydrodynamic force reduces to Stokes drag $\mathbf{F}^H = -6\pi\eta R\mathbf{U}$.

The form of the stochastic or Brownian force \mathbf{F}^B that arises from the thermal fluctuations in the fluid is given by the fluctuation-dissipation theorem:

$$\overline{\mathbf{F}^B(t)} = 0$$

$$\overline{\mathbf{F}^B(t)\mathbf{F}^B(t+\tau)} = 2kT(6\pi\eta R)\mathbf{I}\delta(t) \quad (\text{Eq. 6.2.2})$$

The overbars denote an ensemble average over the thermal fluctuations in the fluid, kT is the thermal energy, and $\delta(t)$ is the Dirac delta function.

The particle evolution equation is obtained by integrating equation 6.2.1 twice over a time step Δt to finally get the random Brownian displacement vector:

$$\Delta\mathbf{x} = Pe\langle\mathbf{U}\rangle\Delta t + \mathbf{X}(\Delta t) + \mathbf{F}^P\Delta t = Pe\langle\mathbf{U}\rangle\Delta t + \mathbf{X}(\Delta t) + \Delta\mathbf{x}^{HS}$$

and $\overline{\mathbf{X}} = 0$, $\overline{\mathbf{X}(\Delta t)\mathbf{X}(\Delta t)} = 2D\mathbf{I}\Delta t$, $D = \frac{kT}{6\pi\eta a}$ (Eq.6.2.3)

This equation shows that at each time step the displacement is equal to the sum of the displacement from the imposed velocity $\langle\mathbf{U}\rangle$ (shear), the random Brownian displacement ($\mathbf{X}(\Delta t)$) and the displacement due to interparticle forces ($\Delta\mathbf{x}^{HS}$). To get the equation, it was assumed that there are no hydrodynamic interactions and as such rotational and translational motions are decoupled. \mathbf{X} is non-dimensionalised by R , t by R^2/D and $\langle\mathbf{U}\rangle$ by D/R .

If we assume that Ψ is a random vector and each element of the vector is selected from a uniform distribution of random numbers ranging from -1 to 1 with a mean value of zero,

$$\text{then } \mathbf{X}(\Delta t) = \sqrt{2D\Delta t}\Psi\sqrt{3}.$$

If we make all the equations non-dimensional, then for every time step each particle moves:

$$\begin{aligned}\Delta x &= \sqrt{2\Delta t}\Psi\sqrt{3} - Pe' \cdot \gamma_0 \cdot \sin(Pe' \cdot t) \cdot y \cdot \Delta t \\ \Delta y &= \sqrt{2\Delta t}\Psi\sqrt{3} \\ \Delta z &= \sqrt{2\Delta t}\Psi\sqrt{3} \\ \text{and } Pe' &= \frac{\omega R^2}{D}\end{aligned}\quad (\text{Eq.6.2.4})$$

where γ_0 is the peak amplitude of shear, ω is the frequency of oscillation, Ψ is a random number ranging from -1 to 1 with a mean value of zero, x is the velocity direction and y is the velocity gradient direction. The Peclet number defined in the simulation (Pe') is different than the Peclet number used in the experiments (Pe), as the former relates to a specific frequency of oscillation and the latter to a shear rate. The relation between the two is $Pe = \gamma Pe'$.

Stress calculation

According to Foss and Brady (2000, JOR). in order to calculate the stress, the algorithm directly calculates the pairwise interparticle forces that would have resulted in the hard sphere displacements during the course of a time step. By examining Eq.6.2.3 and equating the contribution due to interparticle force with the hard sphere displacement we get in dimensional form:

$$\mathbf{F}^P = 6\pi\eta a \frac{\Delta x^{HS}}{\Delta t} \quad (\text{Eq.6.2.5})$$

This is simply the average Stokes drag on the particle during the course of the hard-sphere displacement. Once the interparticle forces from each collision are known, they can be used to calculate the stress. The bulk stress, which is defined as the average stress over the volume V containing n particles is given by:

$$\langle \boldsymbol{\Sigma} \rangle = -\langle p \rangle_f \mathbf{I} + 2\eta(1 + \frac{5}{2}\phi) \langle \mathbf{E} \rangle - nkT\mathbf{I} - n \langle \mathbf{x}\mathbf{F}^P \rangle \quad (\text{Eq.6.2.6})$$

$\langle p \rangle_f$ is the average fluid pressure, $-nkT\mathbf{I}$ is the isotropic stress associated with the Brownian thermal motion and $2\eta(1 + \frac{5}{2}\phi) \langle \mathbf{E} \rangle$ is the hydrodynamic contribution to the stress that reduces to the single particle Newtonian Einstein correction. All the rheologically interesting behaviour is contained in the $\langle \mathbf{x}\mathbf{F}^P \rangle$ contribution. In the case of simple shear and these simulations, only one of the tensor values is needed. To calculate the contribution of each particle to the stress we use this non-dimensional equation (normalized with $k_B T/R^3$):

$$\Sigma_{12} = -\frac{r_x \Delta y^{HS}}{V \Delta t} \quad (\text{Eq.6.2.7})$$

6.3 Simulation runs - Results

Initial configurations – Crystallization at rest

We began our simulations trying to recreate the conditions at rest of hard sphere suspensions. Ideally the simulation should show that at volume fractions below 0.494 the system is a fluid, at $0.494 < \phi < 0.545$ a mixed amorphous and crystal state, at $0.545 < \phi < 0.58$ a full crystal and for $\phi > 0.58$ an arrested amorphous glass. Since the simulation is run with non-dimensional parameters, distances are in particle radii and time is in Brownian time t_B .

To begin with, simulations of 105, 501 and 1005 particles were conducted at $\phi = 0.40, 0.56, 0.60, 0.62$ and 0.63 in a cubic box. The time step used was $\Delta t = 2\pi \cdot 10^{-4} t_B$ and the full simulation time was $10^6 \Delta t = 2\pi \cdot 100 t_B$. An additional algorithm for creating the initial configurations was used for $\phi = 0.60$ (Donev et al. 2005). The simulations of 0.40 showed no crystallization (as expected). The following table (6.3.1) shows the approximate time of crystallization for different particle numbers and volume fractions. Full simulation time was about $200\pi t_B$. All simulations that resulted in crystallization, created a monocrystal throughout the cubic cell in a seemingly random orientation. (as opposed to real systems that make small randomly oriented crystallites).

| N \ ϕ | ϕ | | | | |
|------------|--------|------|----------------------------|------------|------------|
| | 0,56 | 0,60 | 0,60 (Donev et al 2005) | 0,62 | 0,63 |
| 105 | 31 | 13 | 25 | 6 | 126 |
| 501 | 226 | 106 | 188 | Almost? | No crystal |
| 1005 | 565 | 113 | 163 / 400 | No crystal | No crystal |

Table 6.3.1: Table of crystallization times at rest for different volume fractions and number of particles. All times are in τ_B units.

The created crystal in any case looks like an FCC crystal, but is slightly distorted. Although the system at $\phi \geq 0.60$ should be in an arrested state and not exhibit crystallization, we can see from the above table that it does. The crystallization time seems to depend on the number of particles in the simulation and also on the initial conditions. When more particles are involved in the simulation and when better initial configurations are imposed (Donev's et al. 2005) the crystallization is delayed. We also discovered that if the Donev algorithm is used to create a packing of 0.64 and then is normalized to 0.60 for use with the simulation, the delay of crystallization reaches about $400 \tau_B$ for 1005 particles.

The built in algorithm of the simulation creates an initial configuration by randomly placing the centers of the particles in the box and then imposing the hard sphere potential. This means that spheres are placed in a volume with no constrictions on their positions and suddenly a

6. Brownian Dynamics Simulations

hard potential is imposed, consecutively displacing every sphere until there are no more overlapping particles. Donev's algorithm creates configurations by starting with a low volume fraction of particles and then increasing particle radius while moving them in a ballistic trajectory and simultaneously enforcing the hard potential. In this way, by slowly increasing the volume fraction to the desired value, Donev's algorithm simulates a more realistic situation (evaporation).

Since the number of particles can influence the speed for which crystallization occurs, we can deduce that crystallization in volume fractions higher than that of 0.58 in this simulation occur primarily due to periodic boundary conditions. Although higher degrees of initial randomness in the system delay crystallization, an arrested glassy state should not be able to crystallize whatever the initial conditions.

The periodic boundary conditions can inflict undesired effects to the system if the individual particle can affect other particles over the distance of the box size. A particle in a low volume fraction diffuses freely around the simulation space and doesn't come into contact with any other particles. This means that the motion of each particle can only affect itself. As the volume fraction rises, particles will increasingly collide with each other and each particle will affect more of its neighbouring particles as each collision will cause other successive collisions. Essentially this means that the motion of each individual particle in the simulation is influenced by other particles in a distance increasing with volume fraction causing cooperative motion. At low volume fractions, particle collisions dissipate at a short distance, whereas at high volume fractions a much larger distance is needed due to larger propagation of collisions. At volume fractions close to maximum packing examined here, these distances may grow beyond the size of the box. If the box size is smaller than this distance, then the particle motions are impacted by periodic effects. If the system begins as non ordered, it may be forced to conform to the periodicity of the box, thus turning a glassy system to a distorted crystal. If the examined system is periodic in nature, as the hard sphere FCC crystal structures, then effects should be negligible as long as the box is tailored to the periodicity of the system.

In figure 6.3.2 we show the pair distribution function $g(r)$ plotted against r , averaged from the amorphous part of the 1005 particle simulations. $g(r)$ is a measure of the probability to find a particle at a certain distance from another. First of all it seems that the two initial configurations make little difference in the $g(r)$ at $\phi=0.60$. Besides this it is interesting to note the sharp peak at $r=4$ for the amorphous structures of $\phi=0.56$ and higher. The peak remains exactly at $r=4$ for 0.56, 0.60 and 0.62. This means that there is a statistically significant amount of pairs of three particles that touch each other and are in a straight line. This peak is seen in all the initial configurations of the simulation program and also Donev's algorithm and the amount of frames averaged didn't make a difference. These statistically significant three

6. Brownian Dynamics Simulations

particles in a row could act as nucleation points for the crystal to grow and coupled with the periodicity can create crystallization within the simulation time. A similar double peak was seen experimentally by Smith (2004) in dense crystallizing hard sphere depletion gels under oscillatory shear.

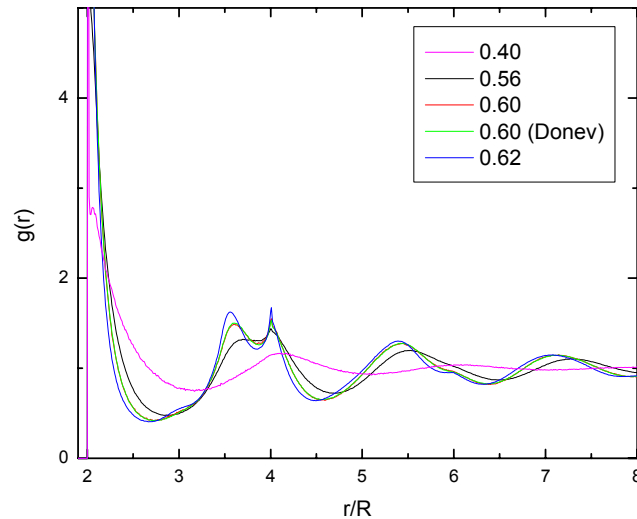


Figure 6.3.2: Pair distribution function $g(r)$ for the initial configuration of the simulations averaged over the initial frames

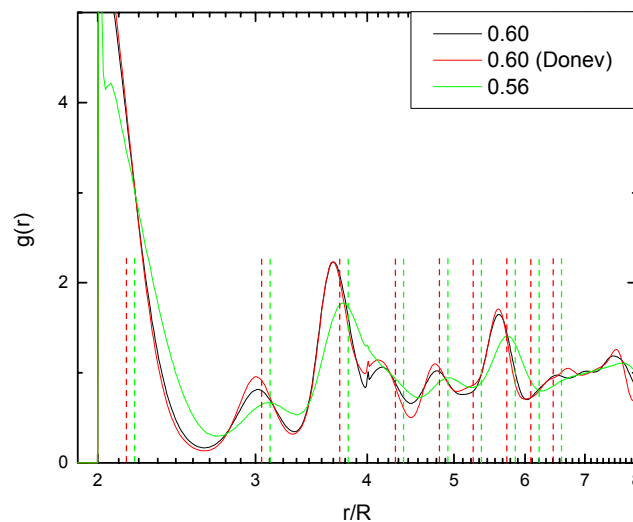


Figure 6.3.3: Pair distribution functions for crystallized frames of simulation. Vertical dashed lines correspond to the expected distances of the FCC crystal for the two volume fractions, 0.60 (red) and 0.56 (green).

6. Brownian Dynamics Simulations

In figure 6.3.3 again we have the $g(r)$ plotted against r for the simulation with 1005 particles, but now it is averaged through the frames that have crystallized. Due to the distorted FCC crystal, the peaks do not appear in the distances expected for a normal FCC crystal structure (In our case these are $2\sqrt{2}$, $2\sqrt{3}$, $2\sqrt{4}$, ...) and this is especially true for the higher volume fraction where the particles are more constricted.

Crystallization under shear

At 0.62 and for 1005 particles the particles did not crystallize in the given simulation time at rest. We decided to begin oscillatory shear simulations at this ϕ and this number of particles and compare with experiments.

As mentioned before, in the simple experimental flow between parallel plates a disordered glassy system at low strains (10%-20%) begins crystallizing with the closed packed direction of the FCC crystal perpendicular to shear and then orients the crystal parallel to shear at 40%-50% strain. The system becomes disordered at higher strains.

We performed simulations at 10%, 30%, 40%, 50% and 80% with $Pe' = \omega R^2/D = 1$ (at $\gamma_0 = 100\%$ this would correspond to $Pe' = 1$ for the maximum shear rate in a period). The first three simulations did exhibit crystallization, but the 50% and 80% did not show any ordering. Not seeing crystallization at 50% and 80% strain was not expected as the experiments show crystallization up to 100% strain. This does not mean that a sheared crystal is unstable at these strains, as will be discussed further in the text. There are indications that the strain of crystallization is also a function of the Pe' number, but the limited number of runs on $Pe' \neq 1$ make this far from conclusive.

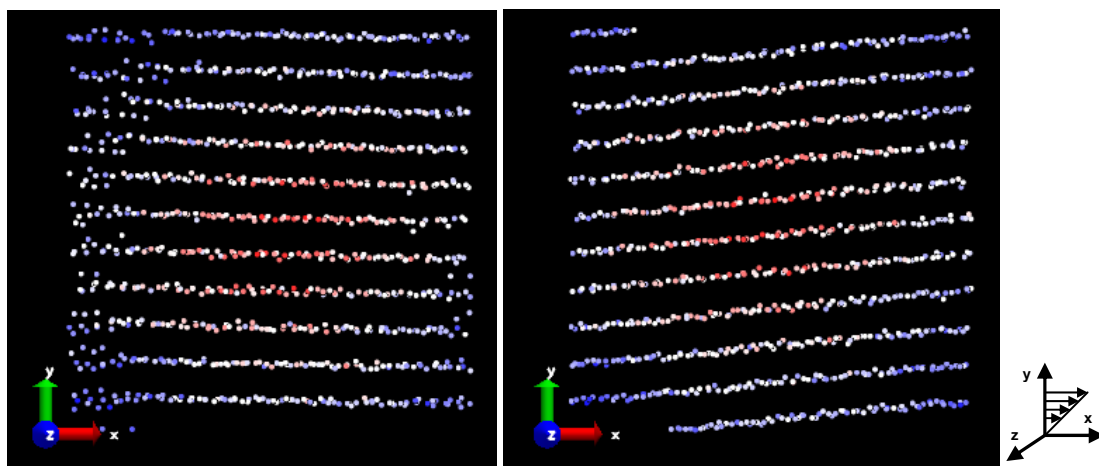


Figure 6.3.4: Tilting of sheared crystallized system in cubic box to accommodate straggling particles. Before accommodation (left) and after (right).

The orientation of the observed crystal was neither parallel, nor perpendicular to shear, but at an arbitrary angle. There were also some wandering particles that were unable to enter the

6. Brownian Dynamics Simulations

crystal structure and in one case that they were eventually accommodated (10%), the whole system tilted on the Z axis. (X - the shear direction, Y - the velocity gradient direction). The images in figure 6.3.4 illustrate this effect. The particle centers are shown as points and the colors show the distance from the centre of the box at the first simulation frame (changing from red to white and then to blue as the distance increases).

It seems that the FCC crystal in the orientation we are examining is anisotropic. This means that in order for the crystal to be properly accommodated in the simulation, the periodic boundary conditions need to be similarly anisotropic. This explains why the crystal is distorted when created at rest and why it has a different orientation than expected with the application of shear. To investigate this possibility we conducted simulations of amorphous structures on an anisotropic box which can accommodate a crystal parallel to shear. The created crystal was again not oriented parallel to shear, but in a random direction again having some particles out of the structure. When we attempted to run some of the same simulations (10%, 30%) at lower Peclet numbers ($Pe'=0.2$) we saw something different for 30% strain. An ordered structure was created, but in this case it seemed to randomly change orientations every few periods until the end of the simulation.

We assume that the periodicity of the system is still interfering with the crystallization process. Even though the simulation box makes a crystal parallel to shear preferable, the periodicity causes the system to get trapped in the first low energy configuration it stumbles on. In all observed cases this configuration was some sort of ordered structure, but it was never the experimental FCC crystal parallel or even perpendicular to shear. The changing structures at low Pe' show us that if the simulation time restrictions were not in effect, a crystal parallel to shear could possibly form.

Crystal under shear – Zig-zag motion and slipping layers

A crystal parallel as well as a crystal perpendicular to shear were simulated in anisotropic boxes again at $Pe'=1$ with 5%, 10%, 30%, 50% and 80% strain. The particle positions of these crystal lattices were calculated, set as the initial configurations and subsequently sheared in the simulation. Strains of 120% and 200% were additionally made for the crystal parallel to shear. The volume fraction remained at 0.62, but the particle number changed to 1440 in order to create a crystal that fits perfectly in the box. Both crystals remained stable during shear at all of the above strains, which contradicts experiments as crystal dissolves at high strains (>100%). This is most probably due to the constrictions of the periodic box and possible mechanisms which could lead to the dissolving of the crystal will be discussed further down the text. The images below (figure 6.3.5) illustrate the crystal with the close packed direction parallel to shear on the left and the crystal with the close packed direction perpendicular to shear on the right at $t=0$. (Always X - the shear direction, Y - the velocity gradient direction)

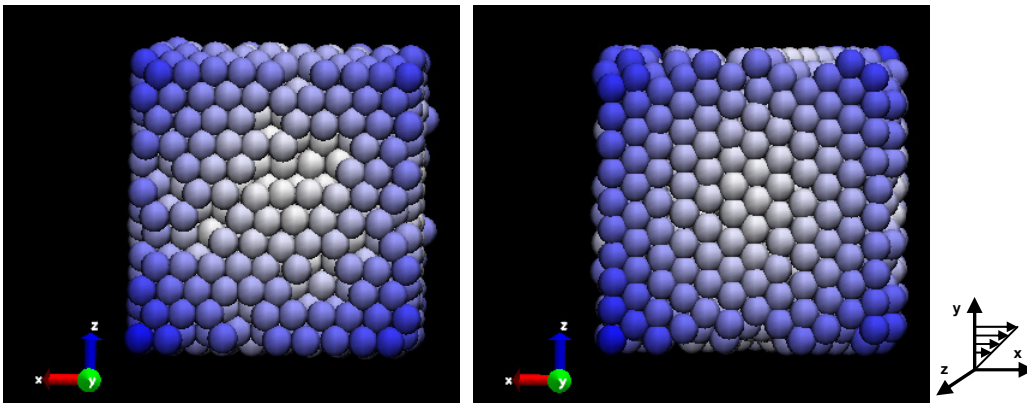


Figure 6.3.5: Illustration of crystal parallel to shear on the left and perpendicular to shear on the right. The plane shown is the (111) FCC plane.

Figure 6.3.6a shows the crystal parallel to shear at 30% strain at a time which is a multiple of the period of oscillation. During the oscillatory shearing motion something interesting to note is the small jiggling motion on the Z axis of particles on the crystal XZ planes (Seen as a left-right jiggle on the second image of all particles that are on the same Y height). This jiggle is what allows layers of particles to slide one past the other and make the shearing process easier. Of course there are more jiggles per period as the strain is increased. This jiggle is the zig-zag motion proposed by Ackerson (1990) and it is illustrated in figure 6.3.6b.

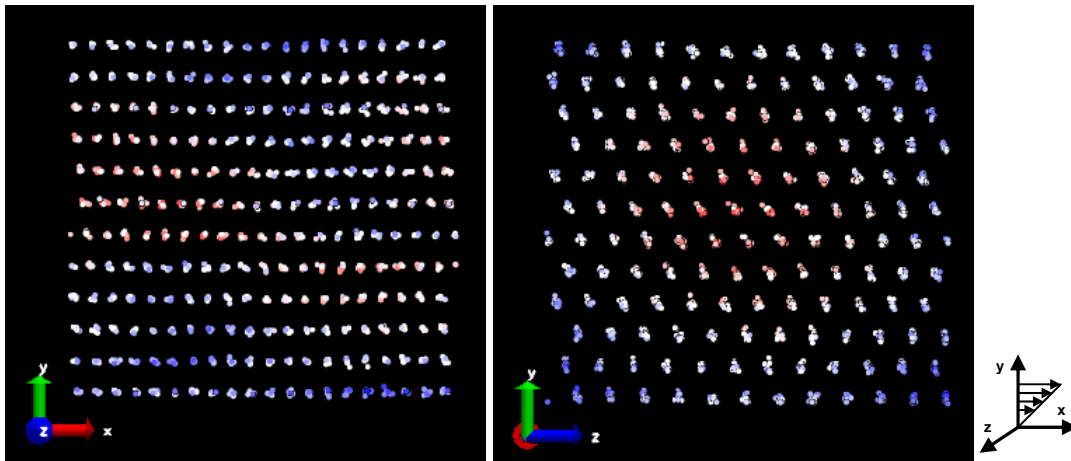


Figure 6.3.6a: Image of zig-zag motion seen in the right image as a jiggle on the Z-axis for particles on the same Y height. (Crystal parallel to shear)

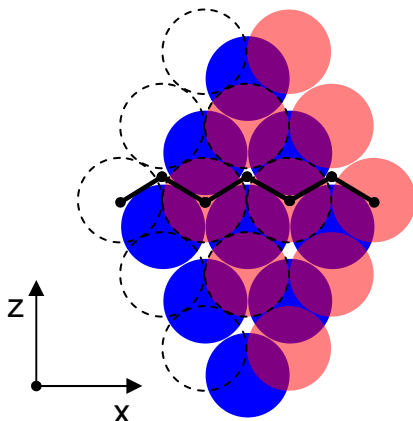


Figure 6.3.6b: Representation of zig-zag motion seen in simulations and proposed by Ackerson (1990). The crystal moves in layers making a small zig-zag motion in the Z direction.

6. Brownian Dynamics Simulations

The colors on the image show the distance of each particle from the center of the box at their initial configuration ($t=0$). Red particles are closer to the center, white are intermediate and blue are farthest. The distribution of the colors in this later image can give a measure of the displacement of the particles. What the above images show us is that particles don't displace much in the Z and Y direction (second image), but they do displace significantly in the X direction (first image) with the help of the zig-zag motion. This displacement in the X direction is more evident when the strains are over 30%. (The two images are in the same time step. The color distribution in the second image is more or less what you see in the initial configuration. So since this has not changed much as no red particles are away from the center, it means that dispersion in the Y and Z direction is small, whereas in the first image, we can see that the image has changed considerably!)

In order to quantify these observations, we need to measure the mean square displacement (MSD) of the particles. Typically in order to do this we would calculate for example in the x direction:

$$\langle \Delta x^2 \rangle_\tau = \left\langle \frac{1}{N} \sum_{i=1}^N [x_i(t+\tau) - x_i(t)]^2 \right\rangle_\tau \quad (\text{Eq. 6.3.7})$$

But because of the periodic boundary conditions and the very high density of the system, the MSD calculation needs a correction. The random Brownian displacement at every step coupled with the periodic boundary conditions and finite amount of particles cause the MSD measured with equation 6.3.7 to deviate from the correct value. As we can see from Figure 6.3.8, the averaged MSD of the individual particles is somehow coupled with the MSD of the centre of mass of the assembly of all the particles. As each particle diffuses randomly with a diffusion co-efficient of D_s , the centre of mass of the assembly of particles also diffuses with a co-efficient of D_s/N . In the case of Figure 6.3.8 there are 1005 particles so the centre of mass diffuses 1005 times slower. As N approaches infinity this motion should diminish.

In order to correct for this, we use the following formula for calculation:

$$\left\langle \frac{1}{N} \sum_{i=1}^N \left[(x_i(t+\tau) - x_i(t)) - \frac{\sum_{i=1}^N x_i(t+\tau) - x_i(t)}{N} \right]^2 \right\rangle_\tau \quad (\text{Eq 6.3.9})$$

which subtracts the centre of mass displacement at each time interval from the displacement of the individual particles. Essentially this calculates the displacement of each particle at time τ in a coordinate system moving with the centre of mass of the assembly of particles. As can be seen from figure 6.3.8, this results in a smoother curve.

6. Brownian Dynamics Simulations

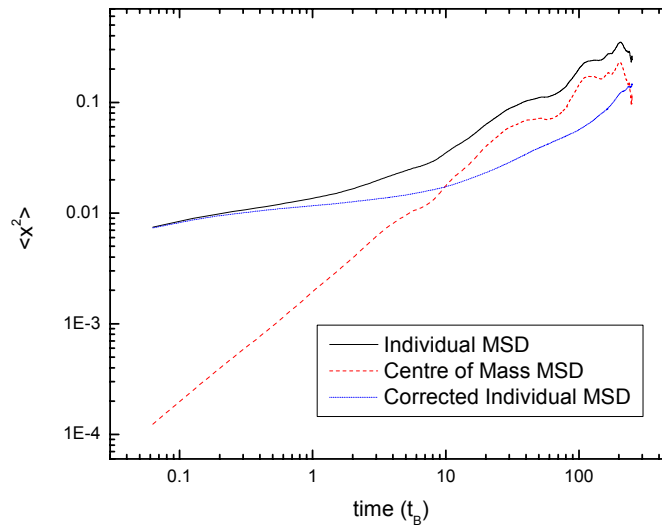


Figure 6.3.8: Erroneous calculation and correction of MSD in the x direction ($\phi=0.63$, $N=1005$ at rest)

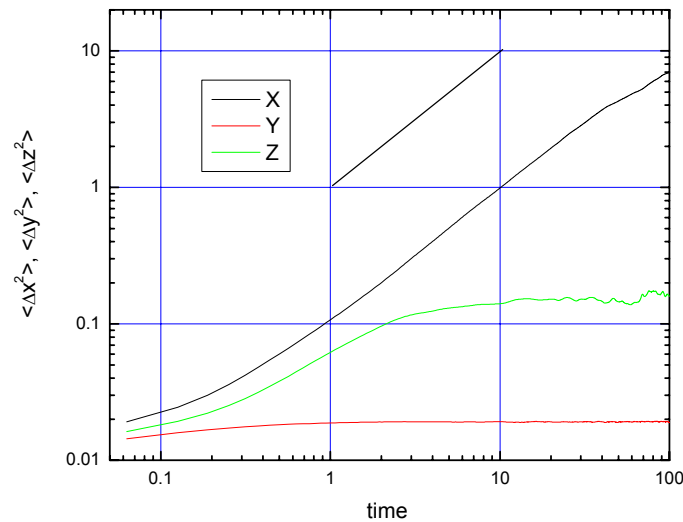


Figure 6.3.10: MSD of sheared crystal ($\phi=0.62$) with close packed direction parallel to shear for 30% strain and $Pe'=1$.

Returning to the displacement in discussion, from figure 6.3.6, we applied the preceding algorithm to the data and came up with figure 6.3.10. Here we can quantify our previous observations and see that indeed in the x direction there is a significant displacement, much larger than in the y or z directions. The slope of unity for the x direction points to diffusive behaviour, although this seems not to be of individual particles, but of whole layers as can be seen in the images. We can also see a plateau of the z direction MSD at a time roughly corresponding to one period. The height of the plateau shows that the jiggles are confined to

6. Brownian Dynamics Simulations

about a distance of $0.38 R$ throughout the simulation. The absence of displacement in the velocity gradient direction and the plateau in the vorticity direction is an important finding as it shows that the zig-zag motion is in the vorticity direction as discussed by Ackerson (1990) and that there is very little particle motion in the velocity gradient direction.

Figure 6.3.11a shows the crystal perpendicular to shear at 80% strain at a time which is a multiple of the period of oscillation. During the oscillatory shearing motion of the crystal perpendicular to shear, there is no zig-zag motion to accommodate the shear as for the crystal parallel to shear. Instead there is a sudden jolt in the positions of the crystal planes on the X axis (Seen as a left-right jolt on the first image, of all particles that are on the same Y height, with some adjacent layers jolting together). This jolting is what allows the layers of particles to slide one past the other and looks more violent than the previous zig-zag motion. This slipping mechanism was proposed by Ackerson (1990) and is shown in figure 6.3.11b. The crystal is able to alternate between twin FCC structures and in time result in a random FCC structure.

In addition to this, at higher strains (50% and 80%) there are big jolts in the Z direction (seen as violent left-right movements in the second image of 6.3.11a). These seem to threaten to destroy the crystal structure, because with every occurrence (once or more in each period), particles break off the crystal and re-attach. In figure 6.3.12, we can see the MSDs for this crystal at 30% and 80% strain. For the 30% strain, the plateau for the X direction quantifies that the slipping motion has now increased to $0.53 R$ compared to the parallel crystal's $0.38 R$ and is indeed more violent. For the 80% strain, the MSDs for X and Z display a linear increase with time showing some sort of diffusive behaviour. The displacement in the X direction can be attributed to multiple slipping of layers as compared to just one slipping at 30% (Seen in the motion of the particles). The displacement in the Z direction can be attributed to the crystal breaking and particle rearranging and the subsequent instantaneous restructuring. As the particles do not return to their initial positions within the crystal after restructuring, the MSD graph shows diffusive behaviour in the Z axis.

6. Brownian Dynamics Simulations

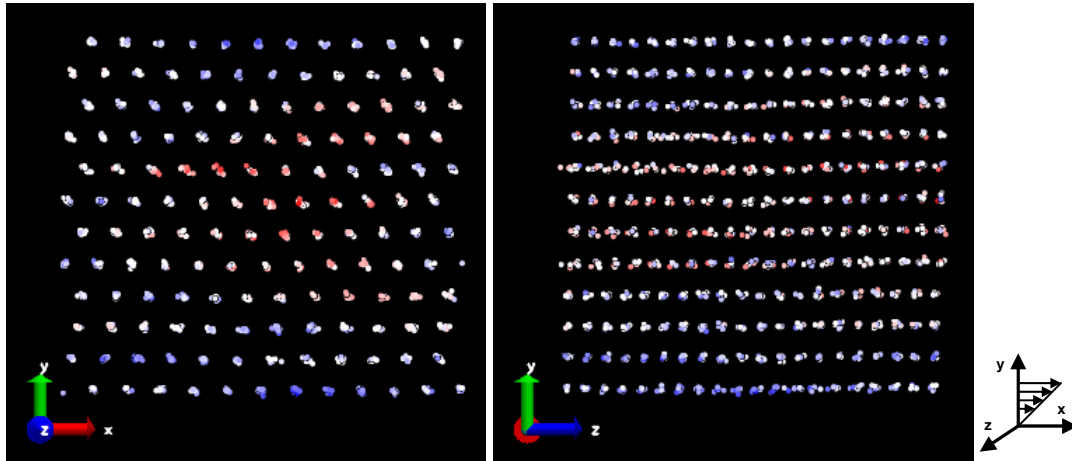


Figure 6.3.11a: Images of crystal with close packed direction perpendicular to shear at a strain of 80% and $Pe^*=1$.

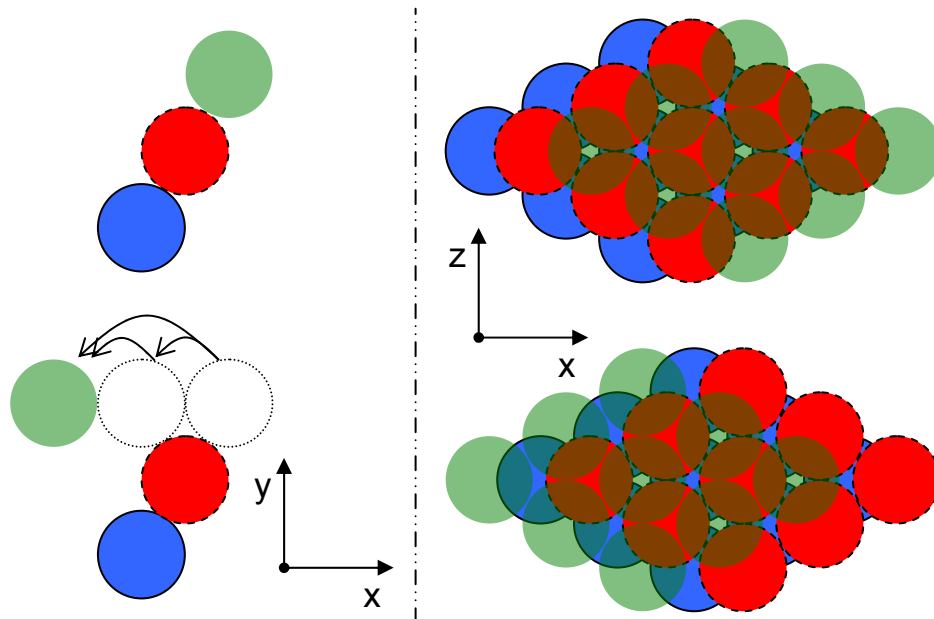


Figure 6.3.11b: Representation of alternating slipping layers in crystal perpendicular to shear. The crystal is able to alternate between twin FCC structures as proposed by Ackerson (1990), which in time results in a random FCC structure.

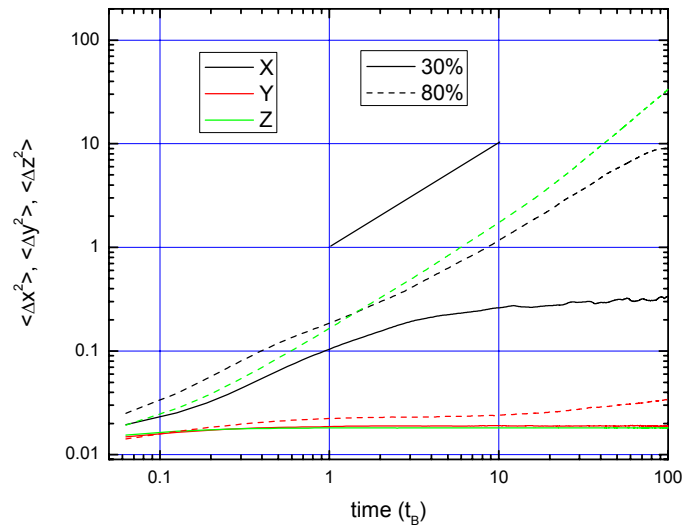


Figure 6.3.12: MSD for crystal perpendicular to shear at 30% (solid lines) and 80% (dotted lines) with X,Y and Z components at $Pe'=1$.

Stress vs Strain

The next figures show the stress-strain Lissajous plots within a period, extracted from the simulation. In the graphs that will be presented, the instantaneous stress and strain are divided with the maximum strain in order to be able compare different strains.

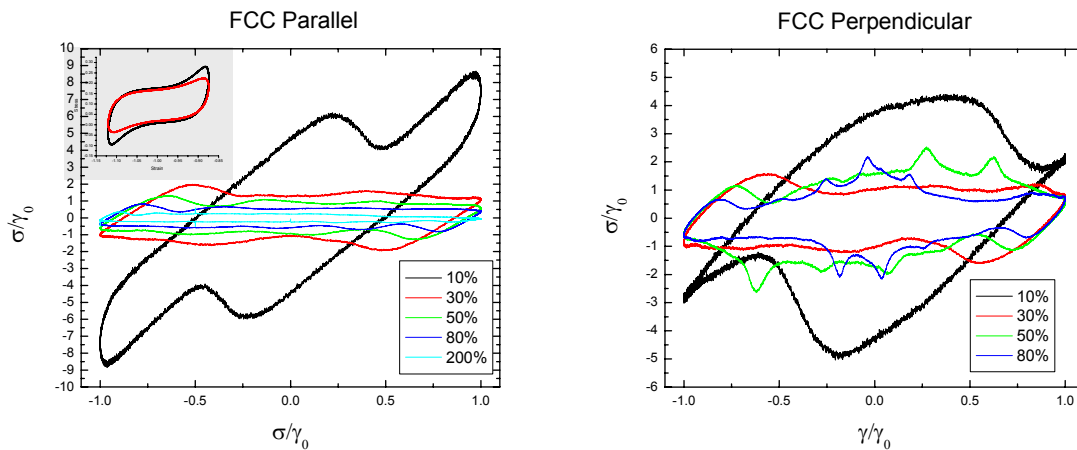


Figure 6.3.13: Lissajous plots of parallel and perpendicular crystal normalized by maximum applied strain for different strain amplitudes. Inset in left figure is from experimental results at 40% strain.

Figure 6.3.13 shows Lissajous plots for the two different crystal orientations at various probed oscillatory strains. The black curve, which is at 10% strain (non-linear), shows very different properties for parallel and perpendicular orientations. The jiggling motion for the crystal

6. Brownian Dynamics Simulations

parallel to shear and the jolting motion for the crystal perpendicular to shear should cause the sharp drop in stress during one period. The different shapes of the plots should correspond to the different mechanisms of sliding during shear.

With increasing strains the crystal parallel to shear creates similar patterns and seems to shear thin as the σ/γ_0 becomes smaller. The crystal perpendicular to shear behaves similarly for 10% and 30%. It becomes more interesting for 50% and 80% (where we see the violent jolting in the Z direction) as large stress peaks are formed. These seem to be indicators of instantaneous shear thickening and agree with the idea that the shearing motion is violently trying to break the crystal structure.

The inset is a Lissajous plot of experimental data of glass (Black) and crystal parallel to shear (Red) under oscillatory shear at a strain amplitude of 40%. The comparison with the experimental results, seen in the inset of the left figure reveals quantitative differences, but qualitative similarities with 10% strain in the simulation and 40% strain in the experiments. It is not apparent why the experimental glass curve is more similar to the simulation crystal curve than the experimental crystal.

An interesting discovery is that at 10% the parallel crystal exhibits a larger stress in a period than the perpendicular crystal. The reason for this is not obvious and experiments suggest the exact opposite. In the experimental setup we have found that a crystal made of randomly oriented crystallites has a higher elastic modulus than a crystal oriented parallel to shear. This suggests that a crystal perpendicular to shear should have higher stress in a period than a crystal parallel to shear. What it surely tells us is that at least *some* orientations different than parallel to shear have higher elastic moduli.

In order to elucidate this discovery, we performed some simulations at a strain of 5%, roughly in the linear regime, to actually measure the stress response of crystals parallel and perpendicular to shear. Figure 6.3.14 shows this response which turns out to be an interesting problem. The response of the crystal perpendicular to shear is distorted and asymmetric.

This is quite puzzling until one realizes that the FCC crystal in this orientation is actually asymmetric. Figure 6.3.15 shows a side image ($(1\bar{1}0)$ plane) of a perfect FCC structure in perpendicular orientation used to initiate the simulations. If one looks carefully it is indeed asymmetric in the velocity and velocity gradient directions. From this side view we can see the ABC stacking that is the cause of the asymmetry. In order to correct this we need to perform a simulation with the twin FCC stacking of CBA and take the average stress of both, as real experiments show a mix of twin FCC structures. An equivalent to a second simulation would be to simply reverse the sign of the applied stress and received strain. The average of the two, gives a curve which is identical to the crystal parallel to shear.

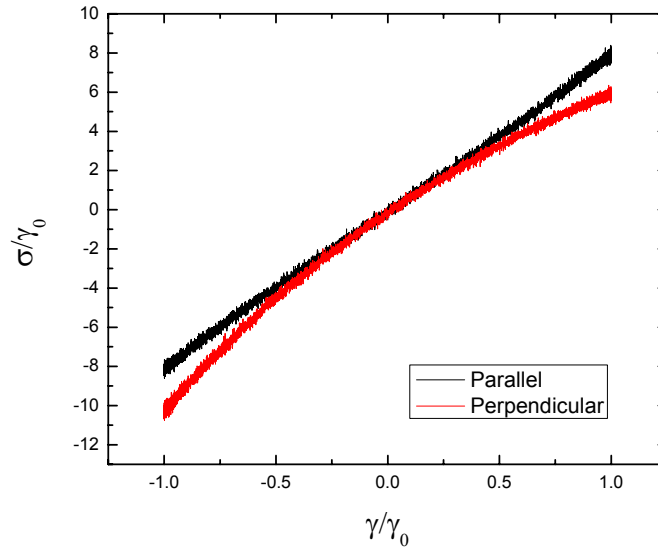


Figure 6.3.14: Lissajous plot of crystals parallel and perpendicular to shear in the linear regime.

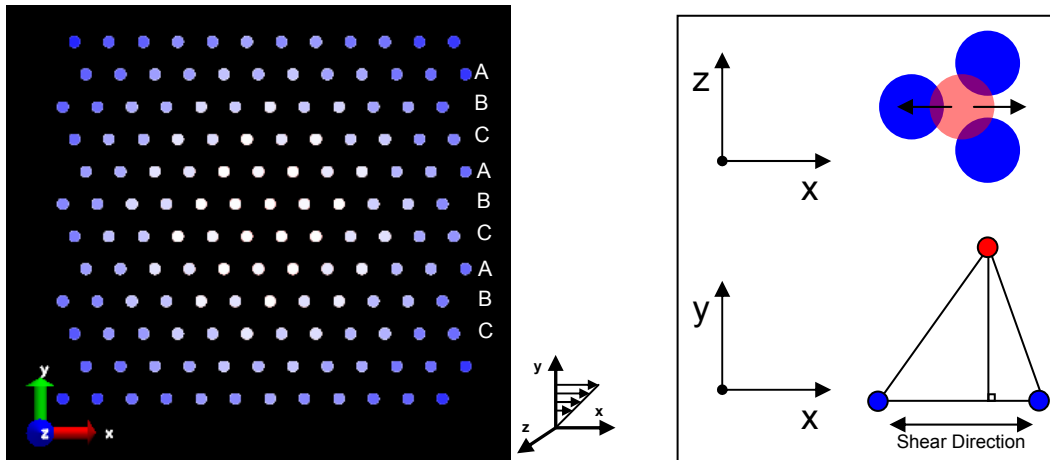


Figure 6.3.15: Image of initial perfect FCC structure in perpendicular orientation used in the simulations (left) and representation of the asymmetry seen in the image (right). As seen in the representation, when under oscillatory shear a layer will need a different amount of stress in the two directions of shear.

This means that the linear elastic modulus derived from the slope of the Lissajous plot is identical for a crystal parallel to shear and a crystal perpendicular to shear. Our assumption that a crystal perpendicular to shear has a higher elastic modulus than a crystal parallel to shear seems to be false, but since experiment shows that a random crystal has a higher modulus than a crystal parallel to shear, this would mean that orientations other than perpendicular to shear have higher elastic moduli. Figure (6.3.16) compares the Lissajous

plot of a crystal parallel / perpendicular to shear to a FCC crystal sheared at the [110] direction. Indeed from the slope we can see that the elastic modulus is about 60% higher than that of a crystal parallel to shear.

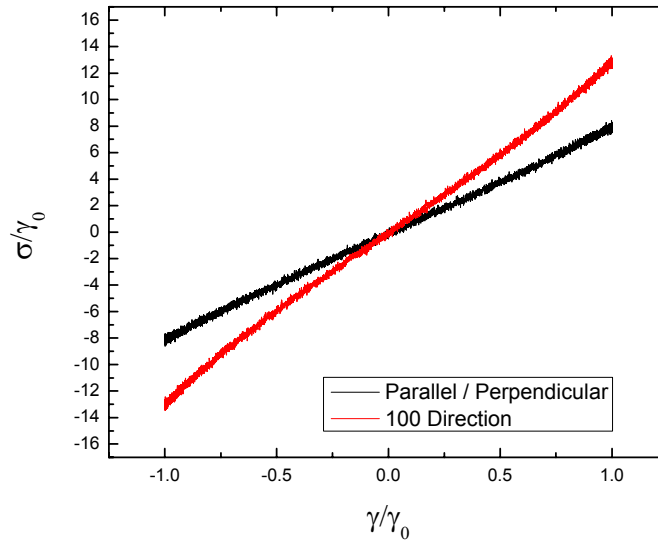


Figure 6.3.16: Lissajous plot in the linear regime of crystal parallel / perpendicular to shear and FCC crystal sheared at the [110] direction.

The findings that the stress for a crystal perpendicular to shear has the same value with that of parallel to shear at linear strain values, less stress at intermediate non linear strains and larger catastrophic stresses at high non-linear strains, could explain why at low strains crystals are formed with a direction perpendicular to shear, while at high strains they are oriented parallel to shear. When the crystal is being created at low strains it naturally stabilizes in the configuration of less stress; so in choosing between parallel and perpendicular orientations, it chooses perpendicular. As strains become higher, the perpendicular crystal cannot be accommodated due to the interparticle collisions which significantly increase stress and so turns to the easier zig-zag parallel structure. Going back to lower strains, the crystal is already formed in a minimum energy configuration and so prefers to remain as such, as no imposing restrictions are enforced upon it to return to perpendicular orientation. As discussed in the experimental section, the rotational geometry probably inflicts some spatial restriction to the crystal perpendicular to shear and thus crystallisation perpendicular to shear is inhibited as crystal parallel to shear is favoured.

The comparison between the Lissajous plots of glass and crystal configurations is seen in figure 6.3.17. The glass response is very noisy, but this is both due to low strain and short sampling time as the system quickly crystallizes. Firstly, even though it looks like we are not in the linear regime for the glass at 2%, it does seem that the glass is more elastic and has a higher stress response than the crystal at 5%. This finding is verified in the experiments. At

higher strains we also witness shear thinning behaviour for the glass, as the maximum stress drops and the shape shifts to a circle indicating increased viscous dissipation. In all cases, the elastic moduli (G') are less for the crystal than for the glass.

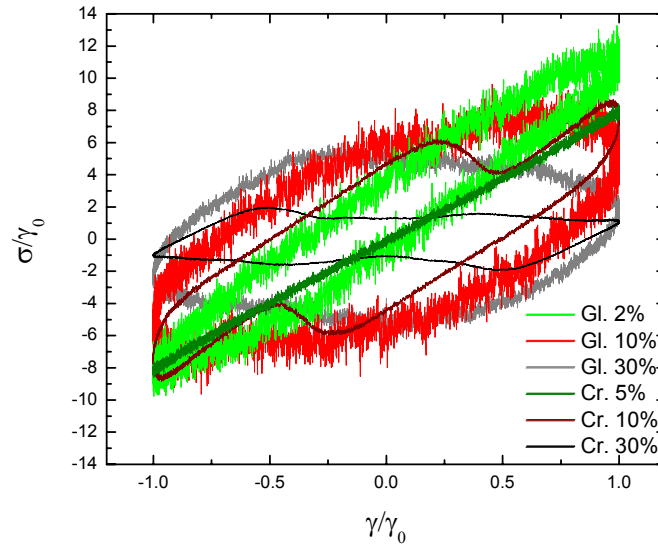


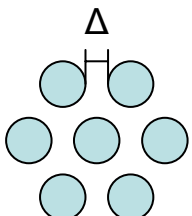
Figure 6.3.17: Lissajous plot of $\phi=0.62$ for glass and crystal at different strains.

The values of the elastic and viscous moduli cannot be directly compared to experiment, as shown by Foss and Brady (2000, JFM), because the hydrodynamic interactions missing from this code substantially contribute to the stress. Thus the values extracted from this simulation are an order of magnitude smaller than the experimental ones.

MSD of glass and crystal

In the next figure (6.3.18) we have the MSDs of different volume fractions of amorphous and crystal systems at rest. For the crystal we can see that the MSD quickly reaches a plateau, which is understandable, as the particles remain in fixed positions in the crystal structure just moving around a central position. If Δ is the average distance between particles with regard to maximum packing and volume fraction, then:

$$\Delta = 2R \left(\sqrt[3]{\frac{\phi_{\max}}{\phi}} - 1 \right)$$



(Eq. 6.3.19)

The diagram shows a cluster of seven light blue circles representing particles. Six circles are arranged in a hexagonal pattern, and one circle is positioned above the center of the hexagon. A vertical line with a horizontal bar at the top indicates the distance Δ between the top circle and the center of the hexagon.

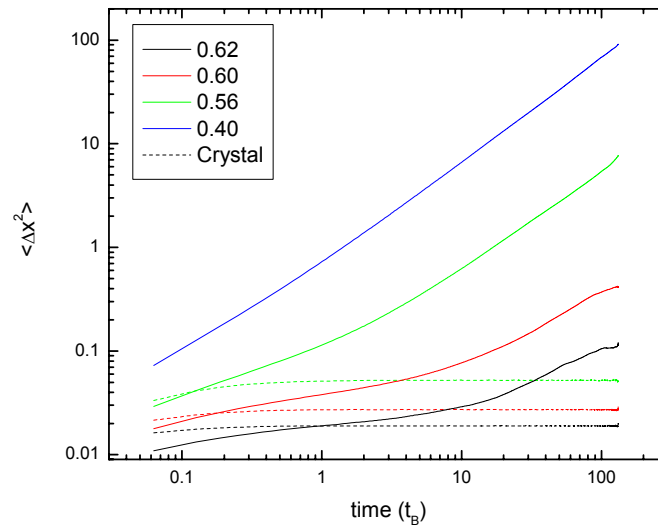


Figure 6.3.18: MSD in the X axis for amorphous and crystal at rest (X,Y and Z are identical)

Δ should be comparable in size to the MSD from the previous figure. For the glass structure, Δ is smaller than that of crystal and yet its MSD goes quite higher than that of crystal. This is explained if one examines the motion of the particles when in a glassy state. Even though the particles are jammed and most particles have less space than their crystal counterparts, there are some particles in the glassy state that have more space. These few particles are able to jump between cages and add to the MSD of the ensemble average causing the irregularities and big differences between crystal and glass. Dynamic heterogeneities such as these have also been seen in experiments conducted on concentrated systems. (Weeks et al. 2000, 2002, Kegel and van Blaaderen 2000, Conrad et al. 2006)

The next figures (6.3.20, 6.3.21) show the MSD of glass and parallel crystal under shear. For these graphs the main difference between glass and crystal is that there is shear induced diffusion for glass that spans all three axis and is approximately the same for all the axis, whereas for crystal as discussed before, there is only diffusion in the axis parallel to shear. This gives us a glimpse of the mechanism behind shear induced crystallization for glass. Although the system is trapped and each particle cannot pass the boundaries of its cage, shear gives it the ability to diffuse within the sample and find the crystal energetic minimum. As seen in figure 6.3.22, shear induced diffusion for glass goes up linearly with strain (Petekidis et al. 2002, 2003). We see that displacements are slightly higher in the velocity direction (X), a little lower in the velocity gradient direction (Y) and even lower for the vorticity direction (Z). At some point, we believe that with increasing strain, the diffusion coefficient becomes too high and begins to inhibit crystallization. This is perhaps why crystallization was not seen in simulated strains greater than 50% when starting with an amorphous sample.

6. Brownian Dynamics Simulations

From figure 6.3.22 we can also see that shear induced diffusion does not increase linearly with strain for the crystal, but reaches a plateau for strains over 50%. This alone could point to a potential mechanism for destroying the crystal as it cannot accommodate the shear induced diffusion applied to it, possibly increasing stresses and leading to instabilities. Indeed a crystal parallel to shear is experimentally seen to dissolve at these high strains. At even higher strains (200%) this is verified as the crystal in the simulation behaves more erratically, showing particle scattering and rearrangements in the Y direction at each period, similar to the crystal perpendicular to shear at lower strains, again pointing to this mechanism for destroying the crystal. The inset of figure 6.3.20 shows the odd behavior of 200% strain as compared to 50% strain. The plateau value of the Y direction increases and we see an erratic displacement in the shear direction (X) not consistent with lower values of strain.

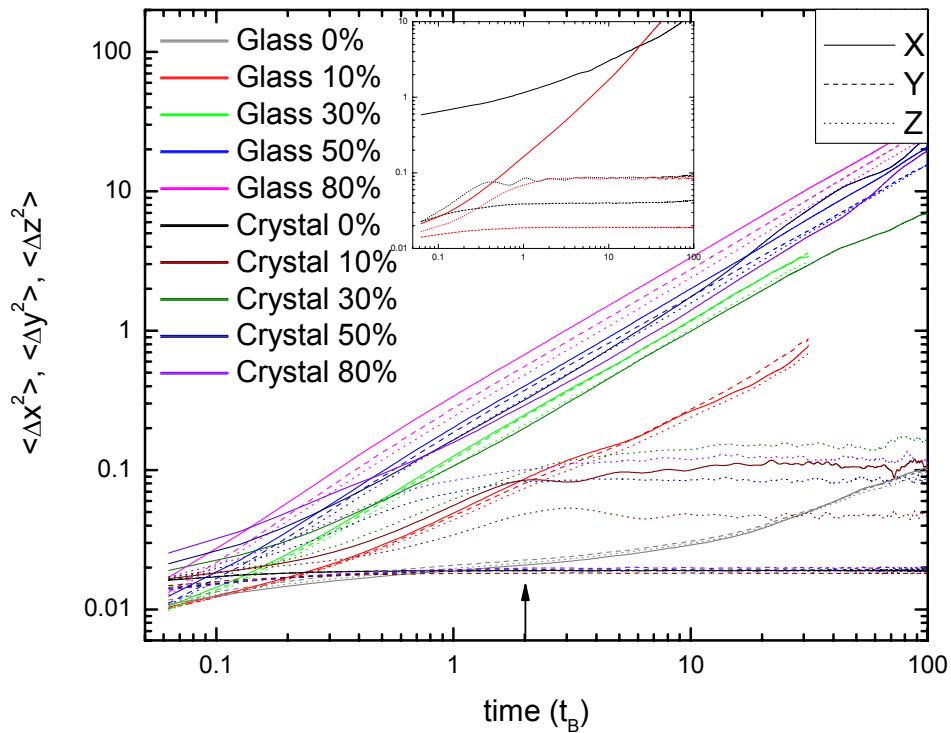


Figure 6.3.20: Graph of MSD for the different axis of glass and crystal under shear for $Pe'=1$ and strains of 0%,10%,30%,50% and 80%. Each colour represents a different strain, with the lighter colours being for glass and the darker ones for crystal. Crystal and glass are both at $\phi=0.62$. The inset shows 200% (black) and 50% (red) of the crystal parallel to shear.

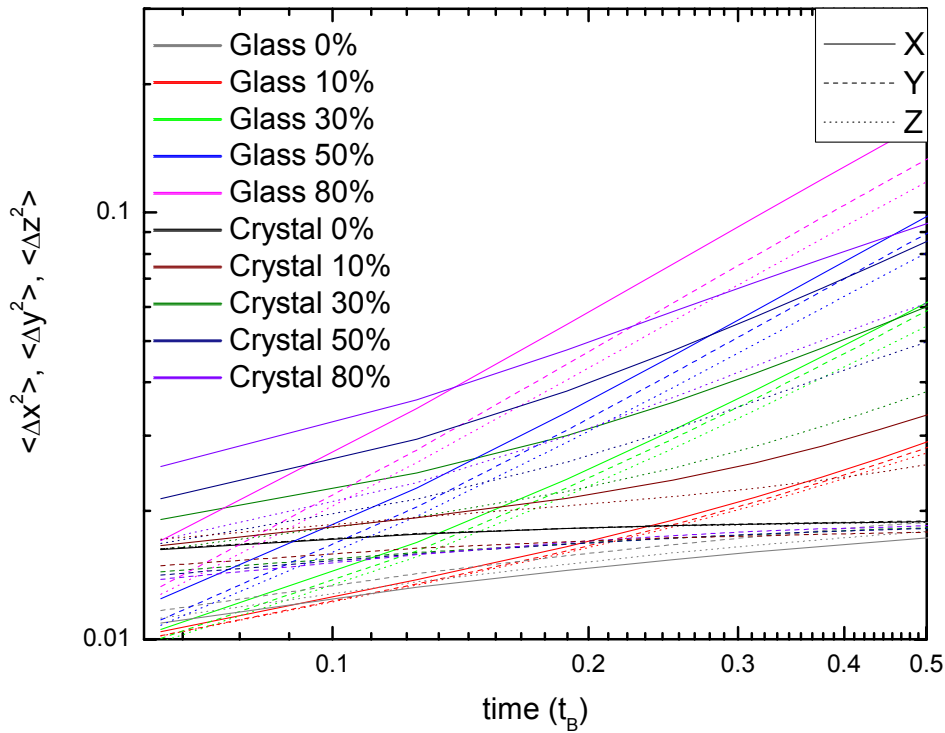


Figure 6.3.21: Graph of MSD for the different axis of glass and crystal under shear for $Pe'=1$ and strains of 0%,10%,30%,50% and 80% concentrating on smaller times.

Figure 6.3.22 shows the MSDs at a time of $2t_B$ that approximately corresponds the 1st echo in the experiments as the experimental Brownian time is $t_B \approx 0.3$ sec and shearing is at 1.6 Hz with $T=0.625$ sec. The inset has a graph of $-\ln(g(T))/3$ vs strain giving a qualitative picture of the MSD taken from the 1st echo in the experiments. We can see that with increasing strains the experiments show a crossover where the glass starts to have larger displacements than the crystal. The simulation shows qualitatively different results with no crossover point. We believe that this happens because there is no implementation of hydrodynamics in the simulation. In a real concentrated system, hydrodynamics cause the short time self diffusion co-efficient to decrease with volume fraction, as with each particle's individual Brownian motion influences neighbouring particles with hydrodynamic interactions. For the volume fractions we have studied this would mean a reduction of approximately 10 times (van Megen et al. 1998) in the short time self diffusion co-efficient.

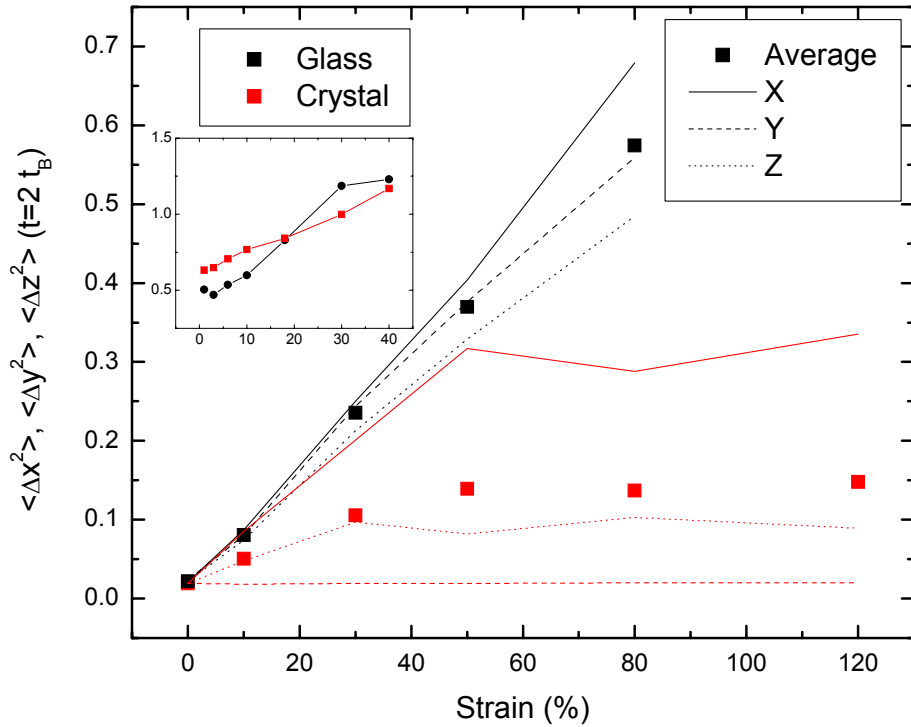


Figure 6.3.22: XYZ and average values of the different axis of MSD at a Brownian time equal to 2 (approximate time of 1st echo in experiments) for the glass (black) and crystal (red) at $\phi=0.62$ at different strains, shown as an arrow in figure 6.3.20. The inset gives a qualitative picture of the experimental MSD at the 1st echo.

If we attempt to take the average values of the MSD at a Brownian time 10 times smaller than in the previous figure at $0.2 t_B$, we get figure 6.3.23. Again the inset gives a qualitative picture of the MSD taken from the first echoes in the experiment. Comparing this figure to the inset, we see that it gives results that are qualitatively similar to the echo experiments. At low strains in the crystal, particles are able to displace themselves more than in the glass as they have more space available. As the strain is increased the sheared particles diffuse more due to shear induced displacements. Unlike the glass, in the crystal displacements for directions other than that of shear are diminished due to ordering. Thus at high strains the glass is able to diffuse more than the crystal.

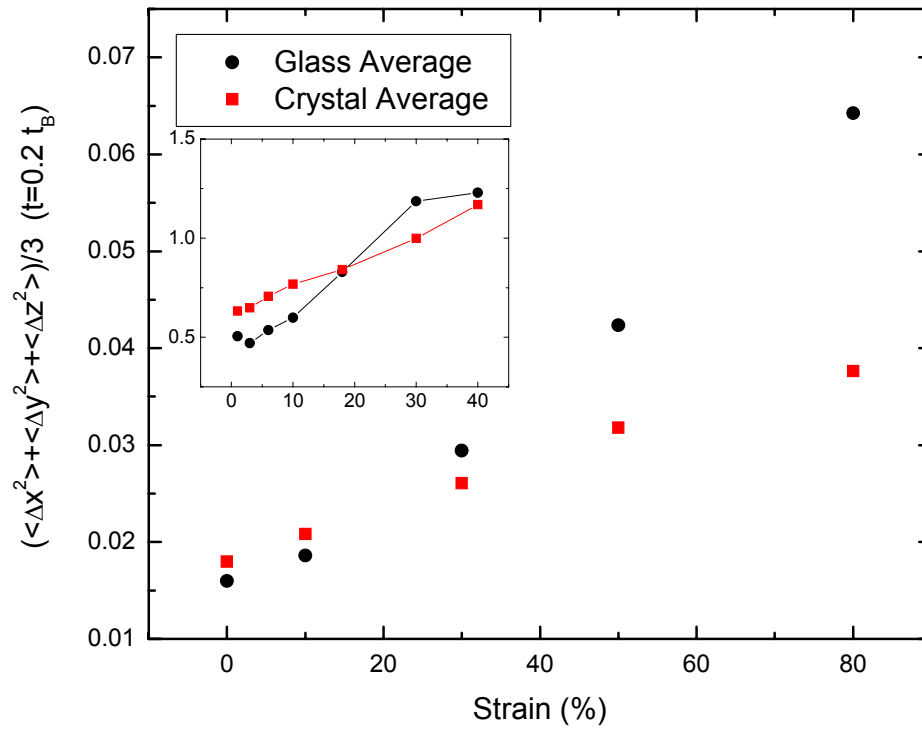


Figure 6.3.23: Average values of the different axis of MSD at a Brownian time equal to 0.2 for the glass (black) and crystal (red) at $\phi=0.62$ at different strains. The inset gives a qualitative picture of the experimental MSD at the 1st echo.

7. Conclusions

To conclude, we have experimentally verified that shear induced crystallization in a hard sphere glass has the effect of significantly dropping the values of the elastic and viscous moduli. Ordering is a mechanism of reducing the stress on the sheared glass material. The crystallization process begins at the crossover strain ($\sim 10\%$) with faint Bragg peaks that become more intense as the strain increases, making a perfect crystal at about 100% strain. At higher strains ($\sim 150\%$) the crystal is destroyed and the structure becomes amorphous. The crystal which is created is a random FCC with the (111) plane parallel to the plates and the close packing direction parallel to shear. Contrary to older experimental studies (Haw et al. 1998), there was no observation of a crystal perpendicular to shear, probably due to geometrical constrictions of the rotational geometry used. Also when comparing the two hard sphere particle sizes we observed that when creating the crystal, rheological stabilization takes longer with smaller particles due to Brownian motion working against the imposed shear. Moreover, the time scale associated with the minimum of the loss modulus in the frequency dependence of both glass and crystal at different volume fractions seems to relate to the mean interparticle distance. It also seems that the crystal's storage and loss moduli are dependent on the glass volume fraction, but in the low frequencies that we probed, the dependence is weaker than that of amorphous glass. When examining the dependence of the elastic modulus to the free volume we discovered that the crystal is more elastic at the same distance from maximum packing than the glass. We also found that the crossover strain of glass is generally higher than its crystal counterpart probably due to slipping layers that make yielding easier. For both glass and crystal the crossover strain is related with two mechanisms. One is associated with the formation of cages, which makes the crossover strain to increase with volume fraction, while the other comes into effect near close packing and is due to a tighter cage formation decreasing the yield strain with volume fraction. Additionally, both the yield and crossover strain of the crystal structure are less affected by volume fraction changes compared to glass due to the increased crystal distance from maximum packing. In the stress-strain Lissajous plots we observed that non-linearities and thickening at the extremes of oscillation at high strains are more apparent for the glass than for the crystal possibly because of less particle collisions due to the crystal slipping layers. It also seems that contrary to intuition, shear induced crystal structure formed from hard sphere glass seems to rheologically age much like the glass itself, whether this is an aging similar to glass or some sort of reorientation is still under question. Lastly, it is evident that small temperature fluctuations throughout the sample create changes in the viscoelastic aging process on both glass and crystal structures.

7. Conclusions

In the DWS-Echo experiments we found that the correlation function decay rate increases linearly with strain and it is not a function of glass or crystal structure which verifies the absence of slip. We also saw that the crystal correlation function at rest decays more than the one from the glass due to larger in cage motions. Once the first echo shows a full de-correlation, thus fully irreversible rearrangements (over the length scale of $\lambda/2$), we have the creation of the shear induced crystal.

From the Brownian Dynamics simulations we conducted, we came to various conclusions. At rest, we were able to see a similar phase diagram as that of the experiments, with a liquid, a crystal and an arrested state, but we discovered that the simulated system and the crystallization were strongly influenced by the amount of particles and initial configuration. We were also able to produce a shear induced configuration from a glass, although it did not have the anticipated orientation. Because of this all simulations on crystals were conducted on a constructed perfect FCC crystal. We believe that both of these findings are due to the periodic boundary conditions that constrict the crystal and accelerate nucleation dynamics. Any attempt to destroy the crystal structure failed as the box size constrictions impose crystal distances and don't allow it to break. However, at high strains (50% for perpendicular and 200% for parallel) there were instabilities indicating possible destruction mechanisms. We were also able to analyse how the slipping layers work on both parallel and perpendicular crystal structures and verify Ackerson's (1990) predictions. Additionally, the Lissajous stress-strain curves of the simulation verified that the stress response for glass is larger than for crystal as seen in the experiments. We also saw that crystals parallel and perpendicular to shear for a random FCC have the same linear stresses, whereas other orientations could have higher/different stresses. These Lissajous plots also helped show that experimental particles crystallize perpendicular to shear at low strains because of lower stresses and then reorient parallel to shear at larger strains because of crystal geometry. From the mean square displacement analysis of particle trajectories we were able to show that crystal MSDs reach a fast and stable plateau as the crystal structure has frozen long time dynamics. Under shear, the MSD increases linearly with strain as seen in echo experiments for glass (Petekidis et al. 2003). Moreover, the crystal has lower long time MSDs than the glass with increasing strain suggesting that irreversible rearrangements in the glass allow the system to reach the preferable crystal structure where they are minimal. Such minimization of irreversible rearrangements may be viewed as the origin of shear induced crystallization.

This work was supported by the Greek General Secretariat for Research and Technology (Basic Research Program, PENED - 03EΔ566).

8. References

- Abou, B., D. Bonn and J. Meunier, "Aging dynamics in a colloidal glass." *Phys. Rev. E* **64**, 021510. (2001)
- Ackerson, B. J., "Shear induced order and shear processing of model hard sphere suspensions." *J. Rheol.* **34**, 553. (1990)
- Ackerson, B. J. and P. N. Pusey, "Shear-Induced Order in Suspensions of Hard Spheres." *Phys. Rev. Lett.* **61**, 1033. (1988)
- Amos, R. M., J. G. Rarity, P. R. Tapster, T. J. Shepherd and S. C. Kitson, "Fabrication of large-area face-centered-cubic hard-sphere colloidal crystals by shear alignment." *J. Rheol.* **34**, 553. (2000)
- Bartlett, P., "A geometrically-based mean-field theory of polydisperse hard-sphere mixtures." *J. Chem. Phys.* **107**(1), 188-196.
- Berne, B. J. and R. Pecora (1976). *Dynamic Light Scattering*. New York, Wiley-Interscience Publications.
- Blaak, R., S. Auer, D. Frenkel and H. Lowen, "Crystal Nucleation of Colloidal Suspensions under Shear." *Phys. Rev. Lett.* **93**, 068303 (2004)
- Bonn, D., S. Tanase, B. Abou, H. Tanaka and J. Meunier, "Laponite: Aging and Shear Rejuvenation of a Colloidal Glass." *Phys. Rev. Lett.* **89**, 015701 (2002)
- Bouchaud, J. P., "Aging in glassy systems: new experiments, simple models and open questions", *Soft and Fragile Matter: Nonequilibrium Dynamics, Metastability and Flow*, M. Cates and M. Evans, IoP Publishing (1999)
- Bryant, G., S. R. Williams, L. Qian, I. K. Snook, E. Perez and F. Pincet, "How hard is a colloidal "hard-sphere" interaction?" *Phys. Rev. E* **66**, 060501 (2002)
- Chen, L. B., M. K. Chow, B. J. Ackerson and C. F. Zuckoski, "Rheological and Microstructural Transitions in Colloidal Crystals." *Langmuir* **10**, 2817-2829. (1994)
- Cipelletti, L. and L. Ramos, "Slow dynamics in glassy soft matter." *J. Phys. Condens. Matter* **17**, R253–R285 (2005)
- Cohen, I., B. Davidovitch, A. B. Schofield, M. P. Brenner and D. A. Weitz, "Slip, Yield, and Bands in Colloidal Crystals under Oscillatory Shear." *Phys. Rev. Lett.* **97**, 215502. (2006)
- Cohen, I., T. G. Mason and D. A. Weitz, "Shear-Induced Configurations of Confined Colloidal Suspensions." *Phys. Rev. Lett.* **93**, 046001 (2004)
- Conrad, J. C., P. P. Dhillon, E. R. Weeks, D. R. Reichman and D. A. Weitz, "Contribution of Slow Clusters to the Bulk Elasticity Near the Colloidal Glass Transition." *Phys. Rev. Lett.* **97**. (2006)
- Courtland, R. E. and E. R. Weeks, "Direct visualization of ageing in colloidal glasses." *J. Phys. Condens. Matter* **15**, S359–S365. (2003)
- Deike, I., M. Ballauff, N. Willenbacher and A. Weiss, "Rheology of thermosensitive latex particles including the high-frequency limit." *J. Rheol.* **43**(3). (2001)
- Denneman, A. I. M., R. J. J. Jongschaap and J. Mellema, "A colloidal crystal modeled by bead–spring cubes." *J. Chem. Phys.* **111**(17). (1999)

8. References

- Derec, C., G. Ducouret, A. Ajdari and F. Lequeux, "Aging and nonlinear rheology in suspensions of polyethylene oxide-protected silica particles." *Phys. Rev. E* **67**, 061403 (2003)
- Derks, D., H. Wisman, A. v. Blaaderen and A. Imhof, "Confocal microscopy of colloidal dispersions in shear flow using a counter-rotating cone-plate shear cell." *J. Phys. Condens. Matter* **16**, S3917–S3927 (2004)
- Donev, A., S. Torquato and F. H. Stillinger, "Neighbor List Collision-Driven Molecular Dynamics for Nonspherical Hard Particles: I. Algorithmic Details." *Journal of Computational Physics* **202**. (2005)
- Duff, N. and D. J. Lacks, "Shear-induced crystallization in jammed systems." *Phys. Rev. E* **75**, 031501 (2007)
- Foss, D. R. and J. F. Brady, "Brownian Dynamics Simulation of hard sphere colloidal dispersions." *J. Rheol.* **44**(3). (2000)
- Foss, D. R. and J. F. Brady, "Structure, diffusion and rheology of Brownian suspensions by Stokesian Dynamics simulation." *J. Fluid Mech.* **407**, 167. (2000)
- Frith, W. J., T. A. Strivens and J. Mewis, "Dynamic Mechanical Properties of Polymerically Stabilized Dispersions." *J. Coll. Int. Sc.* **139**. (1990)
- Grand, A. L. and G. Petekidis, "Effects of particle softness on the rheology and yielding of colloidal glasses." *Rheologica Acta*, To Be Published. (2007)
- Haw, M. D., W. C. K. Poon and P. N. Pusey, "Direct observation of oscillatory shear-induced order in colloidal suspensions." *Phys. Rev. E* **57**, 6859. (1998)
- Haw, M. D., W. C. K. Poon, P. N. Pusey, P. Hébraud and F. Lequeux, "Colloidal glasses under shear strain." *Phys. Rev. E* **58**, 4673. (1998)
- Hébraud, P., F. Lequeux, J. P. Munch and D. J. Pine, "Yielding and Rearrangements in Disordered Emulsions." *Phys. Rev. Lett.* **78**(24). (1997)
- Hébraud, P., F. Lequeux, J. P. Munch and D. J. Pine, "Yielding and Rearrangements in Disordered Emulsions ", *Phys. Rev. Lett.* **78**. (1997)
- Hohler, R., S. Cohen-Addad and A. Asnacios, "Rheological memory effect in aqueous foam." *Europhys. Lett.* **48**(1), 93-98. (1999)
- Hoover, W. G. and F. H. Ree, "Melting Transition and Communal Entropy for Hard Spheres." *J. Chem. Phys.* **49**. (1968)
- Isner, B. A. and D. J. Lacks, "Generic Rugged Landscapes under Strain and the Possibility of Rejuvenation in Glasses." *Phys. Rev. Lett.* **96**, 025506. (2006)
- Kaloun, S., M. Skouri, A. Knaebel, J.-P. Munch and P. Hébraud, "Aging of a colloidal glass under a periodic shear." *Phys. Rev. E* **72**, 011401. (2005)
- Kegel, W. K. and A. v. Blaaderen, "Direct Observation of Dynamical Heterogeneities in Colloidal Hard-Sphere Suspensions." *Science* **287**. (2000)
- Kegel, W. K. and J. K. G. Dhont, "'Aging" of the structure of crystals of hard colloidal spheres." *J. Chem. Phys.* **112**, 3431. (1999)
- Kobelev, V. and K. S. Schweizer, "Strain softening, yielding and shear thinning in glassy colloidal suspensions." *Phys. Rev. E* **71**, 021401. (2005)

8. References

- Lacks, D. J. and M. J. Osborne, "Energy Landscape Picture of Overaging and Rejuvenation in a Sheared Glass." *Phys. Rev. Lett.* **93**, 255501. (2004)
- Laird, B. B., "Weighted density functional theory calculation of elastic constants for face centered cubic and body centered cubic hard sphere crystals." *J. Chem. Phys.* **97**(4), 2699. (1992)
- Laird, B. B., J. D. McCoy and A. D. J. Haymet, "Density functional theory of freezing: Analysis of crystal density." *J. Chem. Phys.* **87**. (1987)
- Lee, Y. S. and N. J. Wagner, "Dynamic properties of shear thickening colloidal suspensions." *Rheologica Acta* **42**(3), 199-208. (2003)
- Loose, W. and B. J. Ackerson, "Model calculations for the analysis of scattering data from layered structures." *J. Chem. Phys.* **101**, 7211. (1994)
- Maranzano, B. J. and N. J. Wagner, "The effects of interparticle interactions and particle size on reversible shear thickening: Hard-sphere colloidal dispersions." *J. Rheol.* **45**(5), 1205. (2001)
- Martelozzo, V. C., A. B. Schofield, W. C. K. Poon and P. N. Pusey, "Structural Aging of crystals of hard-sphere colloids." *Phys. Rev. E* **66**, 021408. (2002)
- Mason, T. G. and D. A. Weitz, "Linear Viscoelasticity of Colloidal Hard Sphere Suspensions near the Glass Transition." *Phys. Rev. Lett.* **75**, 2770. (1995)
- Masri, D. E., M. Pierno, L. Berthier and L. Cipelletti, "Ageing and ultra-slow equilibration in concentrated colloidal hard spheres." *J. Phys. Condens. Matter* **17**, S3543-S3549. (2005)
- Mazoyer, S., L. Cipelletti and L. Ramos, "Origin of the Slow Dynamics and the Aging of a Soft Glass." *Phys. Rev. Lett.* **97**, 238301. (2006)
- Megen, W. v., T. C. Mortensen, S. R. Williams and J. Muller, "Measurement of the self-intermediate scattering function of suspensions of hard spherical particles near the glass transition." *Phys. Rev. E* **58**(5). (1998)
- Megen, W. v. and S. M. Underwood, "Glass transition in colloidal hard spheres: Measurement and mode-coupling-theory analysis of the coherent intermediate scattering function." *Phys. Rev. E* **49**, 4206. (1994)
- Mewis, J. and J. Vermant, "Rheology of sterically stabilized dispersions and lattices." *Pr. Org. Coat.* **40**. (2000)
- Ozon, F., G. Petekidis and D. Vlassopoulos, "Signatures of Nonergodicity Transition in a Soft Colloidal System." *Ind. Eng. Chem. Res.* **45**, 6946-6952. (2006)
- Panine, P., T. Narayanan, J. Vermant and J. Mewis, "Structure and rheology during shear-induced crystallization of a latex suspension." *Phys. Rev. E* **66**, 022401. (2002)
- Paulin, S. E., B. J. Ackerson and M. S. Wolfe, "Equilibrium and Shear Induced Nonequilibrium Phase Behavior of PMMA Microgel Spheres." *J. Coll. Int. Sc.* **178**, 251-262. (1996)
- Paulin, S. E., B. J. Ackerson and M. S. Wolfe, "Microstructure dependent viscosity in concentrated suspensions of soft spheres." *Phys. Rev. E* **55**, 5812. (1997)
- Petekidis, G., A. Moussaid and P. N. Pusey, "Rearrangements in hard-sphere glasses under oscillatory shear strain." *Phys. Rev. E* **66**, 051402. (2002)
- Petekidis, G., D. Vlassopoulos and P. N. Pusey, "Yielding and flow of colloidal glasses." *Faraday Discuss* **123**, 287-302. (2003)

8. References

- Petekidis, G., D. Vlassopoulos and P. N. Pusey, "Yielding and flow of sheared colloidal glasses." *J. Phys. Condens. Matter* **16**, S3955-S3963. (2004)
- Pham, K. N., G. Petekidis, D. Vlassopoulos, S. U. Egelhaaf, P. N. Pusey and W. C. K. Poon, "Yielding of colloidal glasses." *Europhysics Letters* **74**(4), 624-630. (2006)
- Phan, S.-E., M. Li, W. B. Russel, J. Zhu, P. M. Chaikin and C. T. Lant, "Linear viscoelasticity of hard sphere colloidal crystals from resonance detected with dynamic light scattering." *Phys. Rev. E* **60**, 1988. (1999)
- Poon, W. C. K. and P. N. Pusey, "Phase Transitions of spherical colloids", *Observations and Simulations of Phase Transitions of Complex Fluids*, M. Baus, Kluwer Academic Publishers: 3-51 (1995)
- Pronk, S. and D. Frenkel, "Large difference in the Elastic Properties of fcc and hcp Hard Sphere Crystals." *Phys. Rev. Lett.* **90**, 255501. (2003)
- Pusey, P. N., *J. Phys. (Paris)* **48**. (1987)
- Pusey, P. N. and W. v. Meegen, "Phase-behaviour of concentrated suspensions of nearly hard colloidal spheres." *Nature* **320**(6060), 340-342. (1986)
- Pusey, P. N., W. v. Meegen, P. Bartlett, B. J. Ackerson, J. G. Rarity and S. M. Underwood, "Structure of crystals of hard colloidal spheres." *Phys. Rev. Lett.* **63**(25), 2753-2756. (1989)
- Rao, R. B., V. L. Kobleev, Q. Li, J. A. Lewis and K. S. Schweizer, "Nonlinear elasticity and yielding of nanoparticle glasses." *Langmuir* **22**, 2441-2443. (2006)
- Schaertl, W. and H. Sillescu, "Brownian dynamics of polydisperse colloidal hard spheres: Equilibrium structures and random close packings." *J. Stat. Phys.* **77**, 1007. (1994)
- Schöpe, H. J., G. Bryant and W. v. Meegen, "Effect of polydispersity on the crystallization kinetics of suspensions of colloidal hard spheres when approaching the glass transition." *J. Chem. Phys.* **127**, 084505. (2007)
- Schöpe, H. J., T. Decker and T. Palberg, "Response of the elastic properties of colloidal crystals to phase transitions and morphological changes." *J. Chem. Phys.* **109**. (1998)
- Smith, P. A. (2004). *Colloidal Gels under Oscillatory Shear*. School of Physics, University of Edinburgh. **PhD**.
- Smith, P. A., G. Petekidis, S. U. Egelhaaf and W. C. K. Poon, "Yielding and crystallization of colloidal gels under oscillatory shear." *Phys. Rev. E* **76**. (2007)
- Solomon, T. and M. J. Solomon, "Stacking fault structure in shear-induced colloidal crystallization." *J. Chem. Phys.* **124**, 134905. (2006)
- Sorensen, C. M., R. C. Mockler and W. J. Sullivan, *Phys. Rev. A* **14**, 1520. (1976)
- Stieger, M., P. Lindner and W. Richtering, "Structure formation in thermoresponsive microgel suspensions under shear flow." *J. Phys. Condens. Matter* **16**, S3861-S3872. (2004)
- Stieger, M., J. S. Pedersen, P. Lindner and W. Richtering, "Are Thermoresponsive Microgels Model Systems for Concentrated Colloidal Suspensions? A Rheology and Small-Angle Neutron Scattering Study." *Langmuir* **20**, 7283-7292. (2004)
- van Meegen, W., T. C. Mortensen, S. R. Williams and J. Muller, "Measurement of the self-intermediate scattering function of suspensions of hard spherical particles near the glass transition." *Phys. Rev. E* **58**(5), 6073-6085. (1998)

8. References

Vermant, J. and M. J. Solomon, "Flow-induced structure in colloidal suspensions." *J. Phys. Condens. Matter* **17**, R187-R216. (2005)

Viasnoff, V., S. Jurine and F. Lequeux, "How are colloidal suspensions that age rejuvenated by strain application?" *Faraday Discuss* **123**, 253-266. (2003)

Viasnoff, V. and F. Lequeux, "Rejuvenation and Overaging in a Colloidal Glass under Shear." *Phys. Rev. Lett.* **89**, 065701. (2002)

Vorst, B. v. d., D. v. d. Ende and J. Mellema, "Linear viscoelastic properties of ordered lattices." *J. Rheol* **39**. (1995)

Weeks, E. R., J. C. Crocker, A. C. Levitt, A. Schofield and D. A. Weitz, "Three-Dimensional Direct Imaging of Structural Relaxation Near the Colloidal Glass Transition." *Science* **287**. (2000)

Weeks, E. R. and D. A. Weitz, "Properties of Cage Rearrangements Observed near the Colloidal Glass Transition." *Phys. Rev. Lett.* **89**(9). (2002)

Weitz, D. A. and D. J. Pine (1993). Dynamic Light Scattering, The Method and Some Applications. Oxford, Oxford Science Publications.

Acknowledgments

I would like to thank my supervisor George Petekidis for the many hours spent in discussion and all his help, Dimitris Vlassopoulos for his contribution to my rheological background, Mixalis Kapnistos for his help in using and understanding the rheometers and their quirks, John Brady and Kostas Karatasos for their help with the simulations and Andy Downard for the code and his remarks, Manolis Steiakakis, Evelyne van Ruymbeke, Arnaud le Grand, Vasiliki Michailidou, Manos Anyfantakis, Nikos Gomopoulos and the many other people I have asked for assistance, however small, in these past two years. I would also like to thank my family for supporting me, not only for these last two years, but all my life. And of course, Nikki for putting up with me!